NIGHTTIME MEASUREMENTS OF DINITROGEN PENTOXIDE AND THE NITRATE RADICAL VIA CAVITY RING-DOWN SPECTROSCOPY

A Dissertation

by

KATIE CHRISTINE PERKINS

Submitted to the Office of Graduate Studies at
Texas A&M University
in partial fulfillment of the requirements for the degree of

DOCTOR OF PHILOSOPHY

August 2009

Major Subject: Chemistry

NIGHTTIME MEASUREMENTS OF DINITROGEN PENTOXIDE AND THE NITRATE RADICAL VIA CAVITY RING-DOWN SPECTROSCOPY

A Dissertation

by

KATIE CHRISTINE PERKINS

Submitted to the Office of Graduate Studies at
Texas A&M University
in partial fulfillment of the requirements for the degree of

DOCTOR OF PHILOSOPHY

Approved by:

Chair of Committee,	Simon W. North
Committee Members,	Jaan Laane
	Robert R. Lucchese
	Renyi Zhang
Head of Department,	David H. Russell

August 2009

Major Subject: Chemistry

ABSTRACT

Nighttime Measurements of Dinitrogen Pentoxide and the Nitrate Radical
via Cavity Ring-Down Spectroscopy. (August 2009)
Katie Christine Perkins, B.S., Truman State University
Chair of Advisory Committee: Dr. Simon W. North

Development of effective pollution control strategies for urban areas requires accurate predictive models. The ability of models to correctly characterize the atmospheric chemistry, meteorology, and deposition rely on accurate data measurements, both as input and verification of output. Therefore, the measurement techniques must be sensitive, accurate, and capable of resolving the spatial and temporal variations of key chemical species. The application of a sensitive *in situ* optical absorption technique, known as cavity ring-down spectroscopy, will be introduced for simultaneously measuring the nitrate radical and dinitrogen pentoxide.

The cavity ring-down spectrometer was initially designed and constructed based on the experiments by Steven Brown and Akkihebal Ravishankara at the National Oceanic and Atmospheric Administration. The instrument design has since undergone many revisions before attaining the current instrumentation system. Laboratory observations provide verification of accurate N_2O_5 and NO_3 detection with measurements of the nitrate radical absorption spectrum centered at 662 nm, effective chemical zeroing with nitric oxide, and efficient thermal decomposition of N_2O_5. Field observations at a local park provided further confirmation of the instruments capability

in measuring N_2O_5 and NO_3. However, detection limits were too high to detect ambient NO_3. Effective and frequent zeroing can easily improve upon the sensitivity of the instrument. Determination of the source of the polluted air masses detected during these studies was unknown since the typical southerly winds from Houston were not observed. Since deployment in the field, instrumentation modifications and laboratory measurements are underway for preparation of the SOOT campaign in Houston, Texas starting April 15, 2009. Current modifications include automation of the titration with a solenoid valve and an automated filter changer. Wall losses and filter transmission for NO_3 and N_2O_5 will be determined through laboratory measurements in coincidence with and ion-drift chemical ionization mass spectrometer prior to the SOOT project. Potential modifications to improve upon the instrument are suggested for future endeavors.

ACKNOWLEDGEMENTS

The completion of this Ph. D. would not have been possible without the support of friends and co-workers. I am grateful to everyone who has contributed directly or indirectly to the work presented in this dissertation. Special thanks to:

-My advisor, Dr. Simon North, for the opportunity to work on such an exciting project, for being an excellent teacher in class, for his ability to make anything work in the lab, and for his guidance over the years.

-My committee members, Dr. Jaan Laane, Dr. Robert Lucchese, and Dr. Renyi Zhang, for their input and suggestions throughout the course of my education and research.

-Everyone in the North group, previous and present. Erin, Kristin, and Andrea, I don't think I would have made it through without any of you. I'm so grateful for all of your help and support throughout the years and for the strong friendships that were created. I will always be grateful for Justine, for collaboration on this project for the past year. It would not have been the same without you; especially during the early morning hours at Lick Creek Park when we hadn't had enough sleep. Thanks also to Jiho, Hahkjoon, Buddhadeb, Michael, and Qingnan, for your support and friendship.

-The undergraduates that worked with me throughout the years. Thank you, Kelly for helping construct the first design of the instrument. Helen, you provided much entertainment and we had some interesting nights on the roof of the O&M building. Anna, you will always be remembered as the one who first reached a 160 μs ring-down.

-The Center for Atmospheric Chemistry and the Environment, the Environmental Protection Agency, the Texas Air Research Center, and the Houston Advanced Research Center, all whom of which allowed for the existence of this project by providing funding.

-Crystal Reed, who has provided much assistance and allowed use of the trailer for measurements at Lick Creek Park. Thanks also to Chance Spencer and Dr. Don Collins for support and the use of instruments/equipment. I am grateful to Jun Zhang who was there from the beginning at Moody Tower in 2006 and provided great advice then and now. I appreciate the time you all have taken out of your schedule to help me.

-Dr. Barry Lefer and everyone else at the University of Houston who has allowed us access to Moody Tower for measurements and collaborations.

-Dr. Steven Brown, Bill Dubé, and Hendrick Fuchs for their many communications that have helped us work out many of the kinks in the instrument. I am also thankful for the filter changer designs provided by Bill Dubé.

Most of all, I would like to thank my wonderful husband, Sam, for always providing encouragement and support. Without him, I would not have made it through. And to Lucas, our beautiful son, who has not only provided motivation, but joy and entertainment during much needed breaks. My parents have also been a great support throughout this journey. Mom and Dad, you always believed in me and encouraged me at times when I needed it most. I love you and thank you for everything.

NOMENCLATURE

CIMS	Chemical Ionization Mass Spectrometry
CRDS	Cavity Ring-Down Spectroscopy
CW	Continuous-wave
EDAS	Eta Data Assimilation System
ESR	Electron Spin Resonance
FEP	Fluorinated Ethylene Propylene (a type of Teflon® material)
HYSPLIT	Hybrid Single Particle Lagrangian Integrated Trajectory Model
ID	Inner Diameter
K	Kelvin
LIF	Laser-Induced Fluorescence
NASA JPL	National Aeronautics and Space Administration Jet Propulsion Laboratory
NBL	Nocturnal Boundary Layer
NCEP	National Centers for Environmental Prediction
NOAA	National Oceanic and Atmospheric Administration
OD	Outer Diameter
PCI	Peripheral Component Interconnect
PFA	Perfluoroalkoxy (a type of Teflon® material)
PMT	Photomultiplier Tube
pptv	Parts Per Trillion by Volume
PTFE	Polytetrafluoroethylene (a type of Teflon® material)

READY	Real-time Environmental Applications and Display sYstems
sccm	Standard Cubic Centimeters per Minute at STP
SHARP	Study of Houston Atmospheric Radical Precursors
SIP	State Implementation Plan
slpm	Standard Liters per Minute at STP
SOOT	Surface-induced Oxidation of Organics in the Troposphere
STP	Standard Temperature and Pressure
TexAQS-II	Texas Air Quality Study-II
TRAMP	TexAQS-II Radical and Aerosol Measurement Project
TPI	Turns Per Inch
UV	UltraViolet

TABLE OF CONTENTS

Page

LIST OF FIGURES

FIGURE Page

FIGURE Page

LIST OF TABLES

1. INTRODUCTION

1.1 Motivation and Introduction

Predictive models for atmospheric chemistry, meteorology and deposition are critical in the development and assessment of effective pollution control strategies. These models rely on accurate data measurements to characterize the behavior of the atmospheric chemical systems. The ability of models to correctly characterize these systems rests on the data against which they are tested. Therefore, it is crucial that measurement techniques are sensitive, accurate, and capable of resolving the spatial and temporal variations of key chemical species.

The subject of this dissertation is the application of a sensitive *in situ* optical absorption technique, called cavity ring-down spectroscopy (CRDS), to measure the nitrate radical (NO_3) and dinitrogen pentoxide (N_2O_5) simultaneously. This section discusses atmospheric nitrogen chemistry, with a focus on NO_3 and N_2O_5. Explanation for detection requirements for these species leads into section 2, where the basic principles of CRDS are described. Details of the instrumentation design and operation are also illustrated. Initial laboratory observations to provide verification of the readiness for field measurements are presented in section 3. The field observations presented in section 4 demonstrate the successful detection of N_2O_5 and NO_3 in the semi-urban atmosphere of College Station, Texas. Section 5 details the current and

---

This dissertation follows the style of *Journal of Physical Chemistry A.*

future direction for the instrument, with preliminary results from the most recent field observations in Houston, Texas.

1.2 Atmospheric Nitrogen Chemistry

Oxides of nitrogen play an important role in tropospheric atmospheric chemistry due to their contribution to ozone production.[1] The most significant nitrogen oxide species are nitric oxide, NO, and nitrogen dioxide, NO_2, the sum of which is known as NO_x. Figure 1.1 summarizes the important atmospheric nitrogen oxide reactions and thus only a select few will be discussed. Nitric oxide readily reacts with ozone to produce nitrogen dioxide:

$$NO + O_3 \longrightarrow NO_2 + O_2 \qquad \text{(R1.1)}$$

with a rate constant of $k = 1.9\times10^{-14}$ cm^3 $molecule^{-1}$ s^{-1} at 298 K.[2] Nitric oxide can be regenerated by the photolysis of NO_2:

$$NO_2 + h\nu \longrightarrow NO + O \qquad \text{(R1.2)}$$

where an oxygen atom then can undergo reaction with O_2 to form ozone:

$$O + O_2 \xrightarrow{M} O_3 \qquad \text{(R1.3)}$$

This photochemical cycle is inactive at night, leading to the production of the nitrate radical, NO_3, *via* the oxidation of NO_2:

$$NO_2 + O_3 \longrightarrow NO_3 + O_2 \qquad \text{(R1.4)}$$

at a rate of 3.2×10^{-17} cm^3 $molecule^{-1}$ s^{-1} at 298 K.[2] The nitrate radical is rapidly photolyzed during the day, and therefore this reaction is only significant at night. Once NO_3 is formed in the nighttime, it rapidly establishes equilibrium with nitrogen dioxide

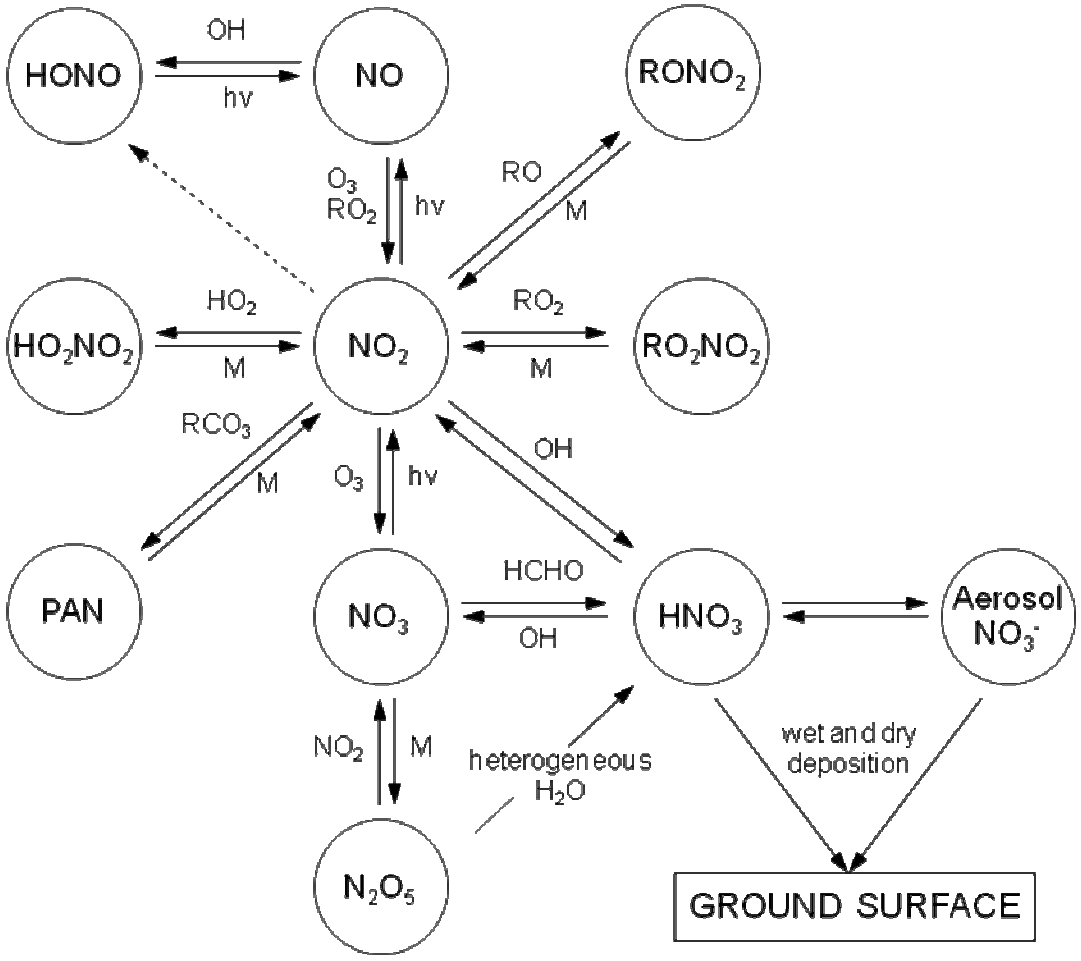

Figure 1.1. Overview of atmospheric nitrogen chemistry.

and dinitrogen pentoxide:

$$NO_3 + NO_2 \xrightarrow{M} N_2O_5 \qquad \text{(R1.5a)}$$

$$N_2O_5 \xrightarrow{M} NO_3 + NO_2 \qquad \text{(R1.5b)}$$

The temperature dependent equilibrium constant given by the expression:

$$\frac{[N_2O_5]}{[NO_3]} = K_{eq} \times [NO_2] \qquad (1.1)$$

is $K_{eq} = 2.7 \times 10^{-27} e^{(11000/T)}$ cm^3 molecule^{-1}. Reaction (1.5a) is the only known source for N_2O_5. Due to the relative stability of N_2O_5 at low temperatures, it can transport in cool air masses. Upon warming, it decomposes to reform NO_3 and NO_2.

N_2O_5 is an important nighttime source of nitric acid through its rapid hydrolysis on wet surfaces and aerosol particles to form two molecules of nitric acid. This reaction is the major loss process of N_2O_5:

$$N_2O_5 + H_2O(het) \longrightarrow 2HNO_3 \qquad \text{(R1.6)}$$

Removal of nitrogen oxide species from the atmosphere is accomplished by deposition. Wet and dry deposition are the processes in which particles and gases are deposited to the surface of the earth. Wet deposition refers to pollutants that become dissolved in water droplets, while particles or gases that are absorbed and/or adsorbed by materials without dissolving in water droplets are termed dry deposition.

1.3 The Nitrate Radical

The gaseous nitrate radical was initially observed in the atmosphere at night, in both urban and remote environments, *via* differential optical absorption spectroscopy

(DOAS) in 1980.[3] Since its detection in the atmosphere, the nitrate radical has been recognized as an important nighttime species.

Substantial nitrate radical concentrations are typically only observed at night because of the rapid photolysis of NO_3 by visible light. Two possible decomposition pathways exist for NO_3:

$$NO_3 + hv \longrightarrow NO_2 + O(^3P) \qquad \text{(R1.7a)}$$

$$\longrightarrow NO + O_2 \qquad \text{(R1.7b)}$$

with wavelength-dependent relative and absolute yields. The threshold for (R1.7a), determined by Davis *et al*,. is 587 ± 3 nm and a corresponding dissociation energy of 48.69 ± 0.25 kcal/mol.[4] Johnston and coworkers[5] later reported 585.5 nm for the threshold and is within the error limits of the previous value. The energy barrier for the dissociation of (R1.7b) is 47.3 ± 0.8 kcal/mol, with an observed threshold of 594.5 nm.[4, 5] Most of the NO_3 that is present at sunrise therefore leads to the formation of NO_2 and O, which can reform ozone *via* reaction 1.3.

At night, appreciable concentrations of NO_3 will only increase in the absence of nitric oxide (NO), which rapidly reacts with the nitrate radical to form two molecules of nitrogen dioxide:

$$NO_3 + NO \longrightarrow 2NO_2 \qquad \text{(R1.8)}$$

with a rate constant of $k = 2.6\times10^{-11}$ cm^3 molecule^{-1} s^{-1}.[2]

As an important nocturnal species, the nitrate radical impacts atmospheric chemistry in several ways. The role of the nitrate radical as a potent nighttime oxidizer is considered to be as important as OH oxidation during the day.[6] The nitrate radical is

known to react with various volatile organic compounds[7] (VOCs) *via* either hydrogen abstraction for reactions with alkanes (RH), or through addition to double bonds, in the case of alkenes ($R_2C{=}CR_2$).

$$NO_3 + RH \longrightarrow HNO_3 + R\cdot \qquad \text{(R1.9)}$$

$$NO_3 + R_2C = CR_2 \longrightarrow \cdot R_2C - CR_2ONO_2 \qquad \text{(R1.10)}$$

These reactions of the nitrate radical with VOCs provide a method of generating organic free radicals and subsequently hydroxyl radicals at night. To demonstrate the effectiveness of the oxidizing capacity of NO_3, Table 1.1 compares the lifetimes for NO_3, O_3, and OH reactions with various VOCs. It is seen that reactions of the nitrate radical with certain trace gases in the atmosphere dominate similar reactions to those with ozone or the hydroxyl radical. Therefore, a direct contribution to the oxidizing capacity of the atmosphere is derived from the nitrate radical.

Additionally, the formation of NO_3 provides a possible reservoir for NO_x by the reaction 1.5a with NO_2. Dinitrogen Pentoxide can then undergo heterogeneous reactions to form nitric acid *via* reaction 1.6. Both N_2O_5 and HNO_3 are readily removed from the atmosphere *via* wet and dry deposition processes,[8] and therefore the production of NO_3 is a key step in nocturnal NO_x and VOC removal. Since NO_x and VOCs are essential for the production of O_3 during the day, nocturnal nitrogen chemistry can impact ozone concentrations for the subsequent day.

Table 1.1. Comparison of tropospheric lifetimes of selected tropospheric constituents for reaction with O_3, OH, and NO_3.

Reactant	k_{O3}	k_{OH}	k_{NO3}	Tropospheric Lifetimes wrt O_3	OH day (hours)	NO_3 night
	(cm^3 $molecule^{-1}$ s^{-1})					
Sulfur-containing trace gases of major atmospheric significance						
Hydrogen Sulfide, H_2S	–	4.7×10^{-12}	$\leq8\times10^{-16}$	–	49.3	$\geq1.4\times10^{4}$
Carbon Disulfide, CS_2	–	2×10^{-12}	$\leq4\times10^{-16}$	–	116	$\geq2.8\times10^{3}$
Carbonyl Sulfide, COS	–	1.5×10^{-15}	–	–	1.5×10^{5}	–
Dimethyl Sulfide, CH_3SCH_3	$\leq8\times10^{-19}$	6.3×10^{-12}	1.0×10^{-12}	≥350	36.8	1.1
Sulfur-containing trace gases of minor atmospheric significance						
Methyl Mercaptan, CH_3SH	–	3.3×10^{-11}	1.0×10^{-12}	–	7	1.1
Ethyl Mercaptan, C_2H_5SH	–	4.7×10^{-11}	1.3×10^{-12}	–	4.9	0.85
Dimethyl Disufide, CH_3SSCH_3	–	2.0×10^{-10}	4.0×10^{-13}	–	1.1	2.4
Industrially produced sulfur-containing compounds						
Sulfur Dioxide, SO_2	–	1.5×10^{-12}	$\leq7\times10^{-21}$	–	15	$\geq1.6\times10^{8}$
Aldehydes						
Formaldehyde, HCHO	$\leq2.1\times10^{-20}$	9.8×10^{-12}	6.8×10^{-16}	$\geq1.4\times10^{8}$	23.6	1.6×10^{3}
Acetaldehyde, CH_3CHO	$\leq6\times10^{-21}$	1.5×10^{-11}	2.8×10^{-15}	$\geq4.7\times10^{4}$	15.4	397
Biogenically emitted alkenes						
Isoprene, C_5H_8	1.2×10^{-17}	1.0×10^{-10}	1.0×10^{-12}	24	2.3	1.1
α-pinene, $C_{10}H_{16}$	8.4×10^{-17}	5.4×10^{-11}	6.2×10^{-12}	3.4	4.3	0.185
β-pinene, $C_{10}H_{16}$	2.1×10^{-17}	7.9×10^{-11}	2.3×10^{-12}	13.5	2.9	0.48
Δ^3-carene , $C_{10}H_{16}$	1.2×10^{-16}	8.8×10^{-11}	9.1×10^{-12}	2.3	2.6	0.12
d-limonene, $C_{10}H_{16}$	6.4×10^{-16}	1.6×10^{-10}	1.2×10^{-11}	0.44	1.44	0.093

Table 1.1. continued

Reactant	k_{O3}	k_{OH}	k_{NO3}	Tropospheric Lifetimes wrt O_3	OH day (hours)	NO_3 night
	(cm^3 $molecule^{-1}$ s^{-1})					
Industrially produced alkenes						
Ethene, C_2H_4	1.8×10^{-18}	8.5×10^{-12}	2.0×10^{-16}	157	27.2	5.5×10^{3}
Propene, C_3H_6	1.1×10^{-17}	2.6×10^{-11}	9.5×10^{-15}	25.8	8.9	117
Trans-2-butene, C_4H_8	2×10^{-16}	6.4×10^{-11}	3.8×10^{-13}	1.4	3.6	2.9
2-methyl-2-butene, C_5H_{10}	4×10^{-16}	8.7×10^{-11}	8.9×10^{-12}	0.70	2.7	0.125
2,3-dimethylbutene, C_6H_{12}	1.1×10^{-15}	1.1×10^{-10}	4.5×10^{-11}	0.24	2.1	0.026
Industrially produced aromatic compounds						
Benzene, C_6H_6	2×10^{-23}	1.2×10^{-12}	$\leq3.2\times10^{-17}$	4×10^{6}	193	$\geq3.5\times10^{4}$
Benzaldehyde, C_6H_5CHO	–	1.3×10^{-11}	2.5×10^{-15}	–	17.8	444
Toluene, $C_6H_5CH_3$	1.2×10^{-20}	6.0×10^{-12}	6.9×10^{-17}	2.4×10^{4}	38.5	1.6×10^{4}
Phenol, C_6H_5OH	–	2.6×10^{-11}	3.6×10^{-12}	–	8.9	0.31
o-cresol, C_7H_7OH	2.6×10^{-19}	4.0×10^{-11}	2.2×10^{-11}	1.1×10^{3}	5.8	0.05
m-cresol, C_7H_7OH	2.0×10^{-19}	5.7×10^{-11}	1.7×10^{-11}	1.4×10^{3}	4.1	0.065
p-cresol, C_7H_7OH	4.7×10^{-19}	4.4×10^{-11}	2.4×10^{-11}	6.0×10^{3}	5.3	0.046
Industrially produced furan and thiophene						
Furan, C_4H_4O	2.4×10^{-18}	4.0×10^{-11}	1.4×10^{-12}	118	5.8	0.79
Thiophene, C_4H_4S	$\leq6\times10^{-20}$	9.5×10^{-12}	3.9×10^{-14}	$\geq4.7\times10^{3}$	24.4	28.5

Note: The tropospheric lifetimes of hydrocarbons are calculated from the expression:

$$\tau_X=1/k_X[X]_{PBL}.$$

assuming the following:
i) $[O_3]_{PBL}=9.8\times10^{11}$ molecule cm^{-3}
ii) $[OH]_{PBL}=1.2\times10^{6}$ molecule cm^{-3}
iii) $[NO_3]_{PBL}=2.5\times10^{8}$ molecule cm^{-3}

Ozone is consumed, rather than produced, in the following set of nocturnal nitrogen reactions, providing another explanation for the importance of nitrate radical chemistry in the troposphere.

$$NO_2 + O_3 \longrightarrow NO_3 + O_2 \qquad \text{(R1.4)}$$

$$NO_3 + NO_2 \xrightarrow{M} N_2O_5 \qquad \text{(R1.5a)}$$

$$N_2O_5 \xrightarrow{M} NO_3 + NO_2 \qquad \text{(R1.5b)}$$

$$N_2O_5 + H_2O(het) \longrightarrow 2HNO_3 \qquad \text{(R1.6)}$$

$$\text{Net}: 2NO_2 + O_3 + H_2O(het) \longrightarrow 2HNO_3 + O_2 \qquad \text{(R1.11)}$$

The net reaction as a source for HNO_3 is thought to be as effective as the daytime reaction of OH and NO_2.[9]

1.4 NO_3 and the Nocturnal Boundary Layer

The lowest part of the atmosphere, closest to the earth's surface is classified as the boundary layer (BL). The boundary layer is defined by Stull[10] as "the part of the troposphere that is directly influenced by the presence of the earth's surface, and responds to the surface forcings with a time scale of about an hour or less." Its height is highly variable, ranging from a few meters to several kilometers. This height determines the available volume for dispersal of pollutants released at the earth's surface. From sunset to sunrise, the BL is typically referred to as the nocturnal boundary layer (NBL) and is characterized by a stable layer. The stable layer forms due to the termination of solar heating and, in turn, the beginning of radiative cooling. The stable NBL is quite

complex due to its varying structure and duration.[11] In urban areas, the NBL is further complicated by buildings that generate mechanical and thermal turbulence.[12, 13]

Pollutant dispersal in the NBL occurs in the horizontal direction more rapidly than in the vertical.[10] This slow vertical mixing gives rise to the accumulation of surface-emitted trace gases in the lower NBL.[14-16] In urban areas, reactions with nitrogen oxides dominate atmospheric chemistry at night.[17] Since nitric oxide titrates ozone (R 1.1) and the nitrate radical (R 1.8), freshly emitted NO, in combination with the slow vertical mixing of the NBL, is responsible for the altitude dependence observed for ozone, nitrogen dioxide, and the nitrate radical.[16, 18] Ozone and the nitrate radical are typically depleted near the earth's surface, while nitrogen dioxide displays a negative gradient (higher concentrations at the ground) from reactions 1.1 and 1.8.[15-17, 19-24] Due to these observed vertical profiles, N_2O_5 also displays an altitude dependence since its formation is dependent on each. The altitude dependence of trace gases in urban areas has a major impact on the nocturnal atmospheric chemistry.

1.5 The Steady State Approximation for N_2O_5 and NO_3

Analysis of NO_3 and N_2O_5 for interpretation of their observed atmospheric concentrations is typically carried out with the utilization of steady state lifetimes.[25, 26] The reaction mechanism, without the addition of sunlight and NO, is straight forward. NO_3 is formed from the reaction of NO_2 and O_3, with the source for N_2O_5 arising from the reaction of NO_3 with NO_2. A reversible reaction of N_2O_5 formation allows for NO_3, N_2O_5, and NO_2 to be in equilibrium. One also assumes that the loss reactions for NO_3 or

N_2O_5 can be summed to form a single sink reaction for each compound. This mechanism is as follows:

$$NO_2 + O_3 \longrightarrow NO_3 + O_2 \qquad k_{1.4} \qquad \text{(R1.4)}$$

$$NO_3 + NO_2 \xrightarrow{M} N_2O_5 \qquad k_{1.5a} \qquad \text{(R1.5a)}$$

$$N_2O_5 \xrightarrow{M} NO_3 + NO_2 \qquad k_{-1.5b} \qquad \text{(R1.5b)}$$

$$NO_3 + X \longrightarrow \text{products} \qquad k_{1.13} \qquad \text{(R1.12)}$$

$$N_2O_5 + Y \longrightarrow \text{products} \qquad k_{1.14} \qquad \text{(R1.13)}$$

The steady state assumption defines the time rate of change in the concentration as approximately zero. From the above mechanism, the differential concentrations for NO_3 and N_2O_5 can be represented as:

$$\frac{d[NO_3]}{dt} = k_{1.4}[O_3][NO_2] + k_{1.5b}[N_2O_5] - k_{1.5a}[NO_2][NO_3] - k_{1.13}[NO_3] \qquad (1.2)$$

$$\frac{d[N_2O_5]}{dt} = k_{1.5a}[NO_2][NO_3] - k_{1.5b}[N_2O_5] - k_{1.14}[N_2O_5] \qquad (1.3)$$

Therefore, by assuming steady state in N_2O_5, $d[N_2O_5]/dt \approx 0$, the irreversible removal for N_2O_5 is approximately equal to the difference in the formation and loss of N_2O_5 from its equilibrium with NO_3 and NO_2.

$$k_{1.14}[N_2O_5] \approx k_{1.5a}[NO_2][NO_3] - k_{1.5b}[N_2O_5] \qquad (1.4)$$

Similarly, by assuming a steady state in NO_3, i.e. $d[NO_3]/dt \approx 0$, we obtain the following expression:

$$k_{1.4}[O_3][NO_2] \approx k_{1.13}[NO_3] + k_{1.14}[N_2O_5] \qquad (1.5)$$

from substitution of Equation 1.4 into Equation 1.2. This implies that the source of NO_3 from the reaction of NO_2 with O_3 is approximately equal to the sum of the sink reactions for NO_3 and N_2O_5.

By further assumption, NO_3 and N_2O_5 are approximately in equilibrium with each other given by the temperature-depended equilibrium expression:

$$[N_2O_5] = K_{eq}(T)[NO_2][NO_3] \tag{1.6}$$

Therefore, the following expression is generated for the steady state lifetime of NO_3 by substitution of Equation 1.6 into Equation 1.5:

$$\tau_{ss}(NO_3) = \frac{[NO_3]}{k_{1.4}[O_3][NO_2]} \approx \left(k_{1.13} + k_{1.14}K_{eq}(T)[NO_2]\right)^{-1} \tag{1.7}$$

If, however, there are negligible sinks for N_2O_5, i.e. $k_{1.14} \ll k_{1.13}$, this steady state lifetime expression simplifies to

$$\tau_{ss}(NO_3) = \frac{[NO_3]}{k_{1.4}[O_3][NO_2]} \approx k_{1.13}^{-1} \tag{1.8}$$

Similarly, using the equilibrium for NO_2, NO_3, and N_2O_5, the steady state lifetime of N_2O_5 can be described as:

$$\tau_{ss}(N_2O_5) = \frac{[N_2O_5]}{k_{1.4}[O_3][NO_2]} \approx \left(k_{1.14} + \frac{k_{1.13}}{K_{eq}(T)[NO_2]}\right)^{-1} \tag{1.9}$$

As in the NO_3 steady state lifetime simplification, if there are negligible sinks for NO_3, i.e. $k_{1.14} \gg k_{1.13}$, the Equation 1.9 is simplified to:

$$\tau_{ss}(N_2O_5) = \frac{[N_2O_5]}{k_{1.4}[O_3][NO_2]} \approx k_{1.14}^{-1} \tag{1.10}$$

The steady state assumption can rarely be applied for NO_3/N_2O_5 nocturnal air masses. In polluted environments, when it may require long periods of time to achieve steady states of NO_3 and N_2O_5, the steady state analysis fails to model actual NO_3 and N_2O_5 observed concentrations. This situation can arise when there are significant changes in the chemistry, such as fresh emissions of NO and/or NO_2, rapid dilution by other air masses, chemical losses for NO_2 and O_3 not accounted for in the above mechanism, or changes in temperature that shift the NO_2-NO_3-N_2O_5 equilibrium. Since these significant changes are highly probable in the actual atmosphere, application of the steady state analysis is not feasible. For example, Brown *et al.* has observed gradients in the NO_3 and N_2O_5 mixing ratios, lifetimes, and NO_x partitioning of the measured vertical profiles.[27, 28] Pollutants trapped within the nocturnal boundary layer provided the source for the observed and typical gradients in the troposphere. This also emphasizes the importance of individually measuring each species, NO_3, NO_2, and N_2O_5, to provide the ease and capability to accurately model the observed nocturnal chemistry.

1.6 Nitrate Radical Detection in the Atmosphere

The nitrate radical exhibits strong absorption bands in the visible region of the electromagnetic spectrum. Since most atmospherically important species absorption are typically in the UV, it is highly unusual that the nitrate radical absorbs strongly in the red region of the visible spectrum. Wayne *et al.* has reviewed the literature regarding the nitrate radical absorption spectrum.[29] There are two prominent bands centered at 623 nm and 662 nm, as shown in Figure 1.2. The strong absorption bands correspond to the

0-0 and 0-1 symmetric N-O stretching vibration in the excited state at 662 nm and 623 nm, respectively.[2]

Several have discovered that there is a temperature-dependence for the absorption cross section of NO_3.[30-34] The NASA/JPL evaluation determined a value at 662 nm and 298 K of $(2.25\pm0.15) \times 10^{-17}$ $cm^2molecule^{-1}$, which is an average of the results of Sander and Yokelson.[2, 30, 32] Osthoff *et al.* recently reported the absorption cross-section at 662 nm as $(2.29\pm0.19) \times 10^{-17}$ $cm^2molecule^{-1}$at 298 K,[34] which is in agreement with NASA JPL's value.

Also to consider is the quantum yield for dissociation of the nitrate radical because it is non-zero at wavelengths less than 640 nm. NO_3 photolysis leads to two possible dissociation channels, which were introduced previously in this section. The primary quantum yield for dissociation *via* channel 1.7a yields nitrogen dioxide (NO_2) and a ground state oxygen atom ($O(^3P)$), while pathway 1.7b produces nitric oxide (NO) and molecular oxygen (O_2). The total quantum yield, ϕ_{total}, is the sum of the two primary quantum yields. Figure 1.2 plots the nitrate radical photolysis quantum yields at 298K in conjunction with the absorption spectrum for NO_3 at 298K. The total quantum yield approaches unity for excitation wavelengths less than 625 nm and is zero for wavelengths greater than 640 nm. Therefore, with the prominent absorption band at 662 nm and a photolysis quantum yield of zero, detection at this wavelength is ideal for atmospheric absorption measurement.

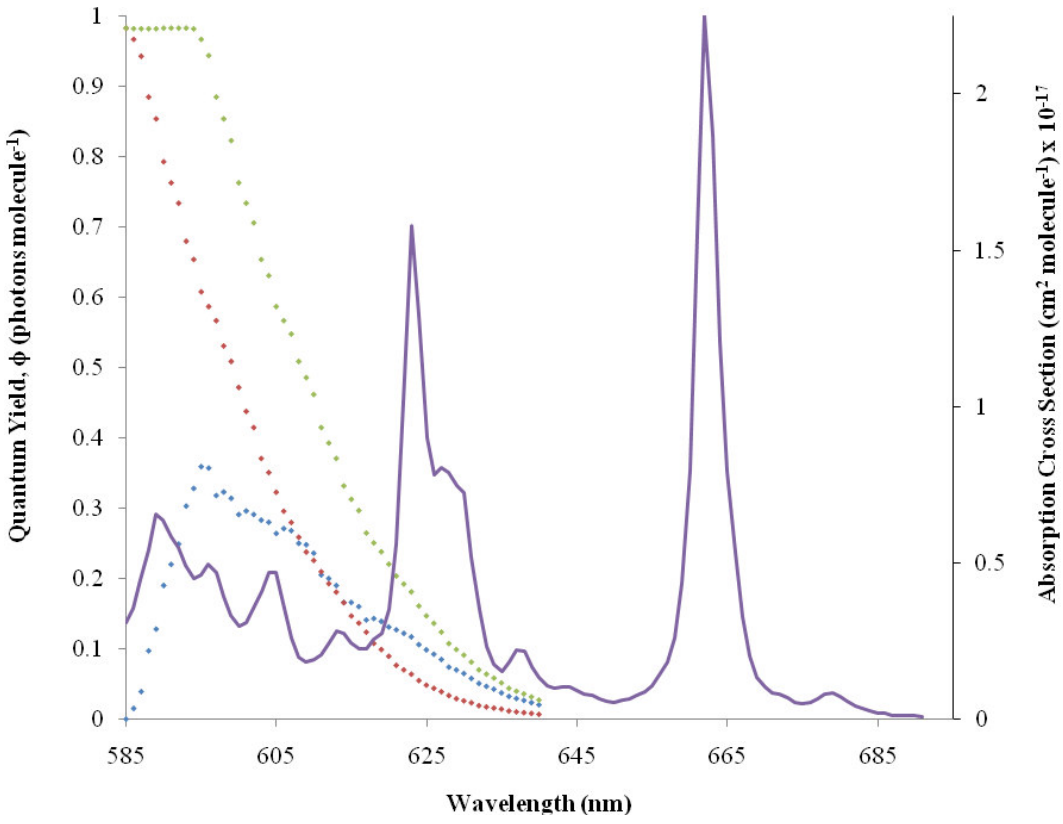

Figure 1.2. Photolysis quantum yields[5] and the absorption spectrum[2] at 298K for NO_3.

Table 1.2. Absorption cross section at 662 nm for other atmospherically relevant species.

species	$\sigma / 10^{-21}$ (cm^2 $molecule^{-1}$)	Typical Atmospheric Concentrations (ppb)	reference
NO_3	2.250×10^{4}	1×10^{-2}	2
NO_2	2.913	5	35
H_2O	1.06×10^{-5}	1×10^{7}	36, 37
O_3	2.018	40	38

The cross section for H_2O is at 290 K, while the other species are at 298 K.

Not only is the B $^2E' \leftarrow X\ ^2A_2'$ transition at 662 nm ideal due to the zero value for the photolysis quantum yield, but also because most other atmospherically relevant species do not absorb strongly at that wavelength. Table 1.2 lists some of these species and their corresponding absorption cross sections at 662 nm.

Detecting the nitrate radical in the atmosphere poses many challenges. Because the maximum atmospheric mixing ratio of NO_3 rarely exceeds 100 ppt, the measurement technique must be highly sensitive. Sensitive detection is complicated by the presence of many interfering compounds, such as aerosols, water vapor, ozone and nitrogen dioxide. In addition, the nitrate radical is also highly reactive, which complicates the sampling procedure. The difficulty of measuring the nitrate radical limits the variety of techniques capable of doing so accurately.

1.7 Instrumentation Requirements

Simultaneous measurement of NO_3 and N_2O_5 is ideal as is high time resolution in order to follow the expected fast time-scale processes that make the mixing ratios variable. The reactivity of the nitrate radical makes it difficult to sample and considerations of the sampling procedure must be taken into account. The technique must also be capable of resolving the complex environment of the NO_3 radical, such as aerosols, water vapor, nitrogen dioxide, and ozone. Exposure conditions, including vibrations and temperature changes, that are not typically present in the laboratory, also need to be considered. The instrument should be portable and therefore compact for easy transport to various locations for field campaigns.

Because the nitrate radical possesses the strong absorption peaks in the visible region at 623 and 662 nm, it is an ideal candidate for detection by absorption spectroscopy. Most atmospheric measurements of NO_3 are provided by differential optical absorption spectroscopy (DOAS) and have provided detection sensitivities from 0.2 pptv (parts per trillion by volume) to 10 pptv.[16, 24, 39-41] This technique measures the average concentration over a path length of a few kilometers and requires long integration times on the order of minutes. Rather than directly measuring N_2O_5 concentrations, this technique requires the calculation of the steady state mixing ratio of N_2O_5 based on observations of NO_2,NO_3, and temperature.[42] While DOAS is successful at measuring path-averaged NO_3 concentrations, an *in situ* method is desirable for comparing NO_3 and N_2O_5 concentrations with other chemical species measured *in situ*.

A handful of *in situ* techniques have been employed to detect NO_3 and N_2O_5. The earliest technique for NO_3 detection is matrix isolation and electron spin resonance (ESR) spectroscopy of a cryogenically trapped air sample.[43, 44] Slusher *et al.*,[45] as well as Zhang and coworkers[46] have applied chemical ionization mass spectrometry (CIMS) to detect NO_3^- from the reactions of NO_3 and N_2O_5 with I^-. This technique allows for sensitive, real-time detection, but provides the sum of NO_3 and N_2O_5 concentrations, rather than individual concentrations of NO_3 and N_2O_5. Cavity ring-down spectroscopy (CRDS) is another sensitive, real-time detection technique that utilizes the strong visible absorption peaks of NO_3 similar to DOAS. By thermal decomposition to NO_3, N_2O_5 can be directly measured. Brown *et al.*,[47-50] Simpson and coworkers,[51, 52] and Ball *et al.*[53, 54] have all reported CRDS based instruments for atmospheric detection of NO_3 and the sum

of NO_3 and N_2O_5, with detection sensitivities from 0.2-2 ppt and integration times of seconds to minutes. Laser induced fluorescence (LIF) has also recently been applied to direct NO_3 and N_2O_5 detection by Wood and coworkers[55, 56] and Matsumoto *et al.*[57, 58] The technique is similar to CRDS for detection of N_2O_5 via its thermal decomposition to NO_3, however, the detection limits range from 4-80 pptv for integration times of 10-1 min. The sensitivities of the *in situ* LIF technique cannot compete with those of CRDS. The CRDS technique has the ability of accurately measuring NO_3 and N_2O_5 and will be discussed in subsequent sections.

2. CAVITY RING-DOWN SPECTROSCOPY (CRDS)

2.1 Introduction

Cavity ring-down spectroscopy (CRDS) is a sensitive absorption technique where the rate of light absorption is used to determine molecular concentrations. Originally designed in the early 1980s to determine mirror reflectivities[59], the first use of the CRDS concept for spectroscopic applications with gas-phase samples was introduced by O'Keefe and Deacon in 1988.[60] The cavity ring-down technique has now evolved into a valuable spectroscopic method with a variety of applications, including *in situ* measurements of trace gases in the atmosphere. The CRDS method has been reviewed by Paul and Saykally[61] and Scherer *et al.*;[62] in addition to a book complied and dedicated to CRDS by Busch and Busch.[63]

2.2 Basic CRDS Principles

The CRDS technique includes at least two highly reflective mirrors, with reflectivities typically greater than 99.99%. Either a continuous wave (CW) laser (CW-CRDS) or a pulsed laser (P-CRDS) source is used to send a laser pulse directly into the cavity through the back of one of the cavity mirrors. Because our application is a pulse laser system, the latter case will be the subject of future discussion. In this case, the distance between mirrors must be large compared to the pulse width to avoid multi-beam interference in the cell. The small amount of light that is trapped inside the optical cavity reflects back and forth between the two mirrors, while a small fraction (~1-R) transmits through each mirror at each reflection. The intensity of the light exiting the

cavity is monitored as a function of time and allows the decay time of the cavity to be determined. The time required for the cavity to decay to a 1/e of the initial output pulse is called the "cavity ring-down" time. A simulated ring-down decay is depicted in Figure 2.1.

In an empty cavity, with no absorber present, a single exponentially decaying function of time from the cavity of the intensity, I(t), can be detected with a time constant, τ_0. The time constant is inversely proportional to the mirror transmission.

$$I(t) = I_0 \exp\left(\frac{-t}{\tau_0}\right) \qquad (2.1)$$

With the presence of an absorbing species in the optical cavity, an additional loss channel for the light inside the cavity is provided. If the absorption follows Beer's law, the light intensity inside the cavity will still decay exponentially, which results in a decrease in the cavity ring-down time, τ, as shown in Figure 2.2. The intensity decay then follows Equation 2.2:

$$I(t) = I_0 \exp\left(\frac{-t}{\tau_0}\right) = I_0 \exp\left(-\frac{t}{\tau_0} - \frac{1}{R_L} c[A]\sigma t\right) \qquad (2.2)$$

where c is the speed of light, [A] is the concentration of the absorber (molecules cm^{-3}), σ is the absorption cross section (cm^2 $molecule^{-1}$), and R_L is the ratio of the total cavity length to the length over which the absorber is present. R_L is important because in some CRDS systems, the mirrors are purged to ensure their cleanliness; the purge volume then reduces the effective volume where the absorber is present. The ring-down time is

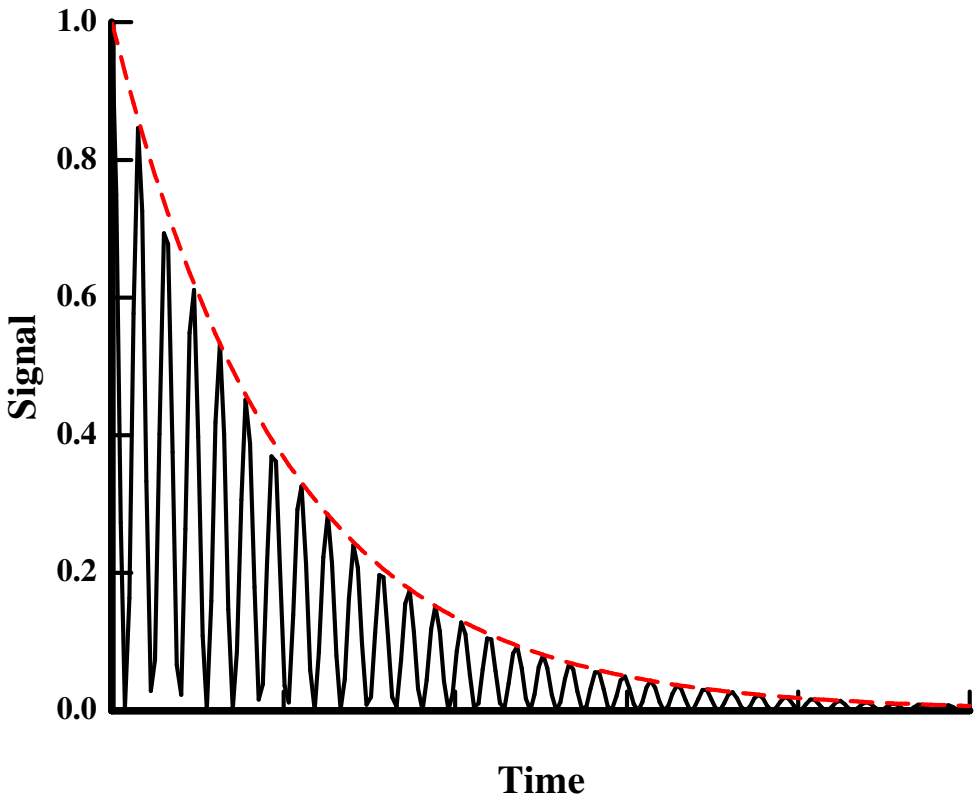

Figure 2.1. Simulated ring-down decay. The smoothed decay profile shown in red is typically observed.

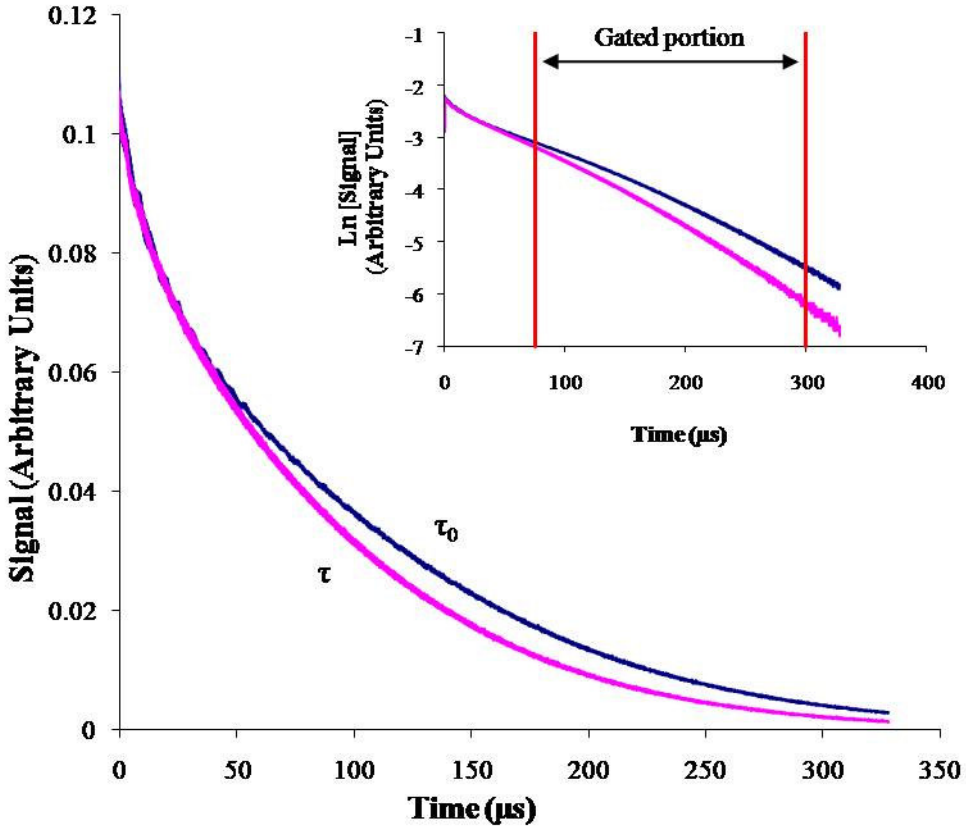

Figure 2.2. Example of observed ring-down decays and corresponding natural logarithm of the observed trace. Decays are from the original instrumentation design for an empty cavity when no absorber is present, τ_0, and when an absorbing species is in the optical cavity, τ. Also displayed is the gated portion used for determining the 1/lifetime values, discarding the portion outside the gates.

independent of the amplitude of light entering the optical cavity. This is useful for pulsed lasers, which can fluctuate in intensity.

The absorber concentration can be obtained directly from the difference in loss rate in a cavity with the absorber present to the loss rate of an empty cavity, which is just a rearrangement of Equation 2.2:

$$[A] = \frac{R_L}{c\sigma}\left(\frac{1}{\tau} - \frac{1}{\tau_0}\right) \qquad (2.3)$$

If the absorption cross section, σ, is known, the absorption measurement for CRDS is an absolute determination.

The advantage of CRDS is the high sensitivity and good time resolution associated with the technique. However, the limitation of the sensitivity is determined by the accuracy of the ring-down time measurement. As mirror reflectivity increases, the fractional uncertainty in the decay time generally decreases, giving rise to a higher sensitivity limit. Although the theoretical limit is typically not achieved in most CRDS experiments, higher mirror reflectivities offer the simplest means to attain greater sensitivity levels. For reactive species, such as the nitrate radical, losses due to the sampling procedure can affect the overall sensitivity of the instrument. In the small signal limit, where τ approaches τ_0, Equation (2.4) gives the limiting sensitivity:

$$[A]_{min} = \frac{R_L}{c\sigma}\left(\frac{\Delta\tau_{min}}{\tau_0^2}\right) \qquad (2.4)$$

$[A]_{min}$ is the minimum detectable concentration, and $\Delta\tau_{min}$ is the smallest measurable

value of τ_0-τ. $\Delta\tau_{min}$ is typically taken as the standard deviation in τ_0 from repeated measurements. For our system in the laboratory with the absorption of NO_3 at 662nm, τ_0 is approximately 125 μs. $\Delta\tau_{min}$ is about 1 μs for a 2.5 s integration time. With the absorption cross-section of 2.25×10^{-17} $cm^2molecule^{-1}$ for NO_3 at 662 nm, $[NO_3]_{min}\approx6\times10^7$ molecules cm^{-3}, or approximately 5 ppt at standard temperature and pressure (STP). Longer integration times can improve upon this limit, as well as increased mirror reflectivities. It is also imperative for large or rapid changes in the background signal to make more frequent measurements of the background relative to the signal.

2.3 Original Experimental Design

The dual cavity-ring down instrument was initially designed and constructed based on the experiments by Brown and Ravishankara.[47, 48] The optical layout for the CRDS instrument, with two separate cells allowing the detection of NO_3 and N_2O_5 + NO_3, is pictured in Figure 2.3 with both the lower and upper breadboard layout designs. The pulsed dye laser (Sirah, CBR-P) operating with DCM dye (Exciton) in dimethylsulfoxide pumped at 532 nm by an Nd:YAG laser (Big Sky Laser, Ultra-CFR) is mounted on a 2×4 ft^2 optical breadboard (TMC). The 6 ns pulsed output of the dye laser is approximately 5 mJ/pulse with a repetition rate of 10 Hz. The dye laser wavelength is tuned to a point on the broad maximum of the NO_3 absorption spectrum near 662 nm.[32] Once directed through a series of iris, the beam passes through a laser port *via* a prism to the upper 2×4 ft^2 optical breadboard that houses the ring-down

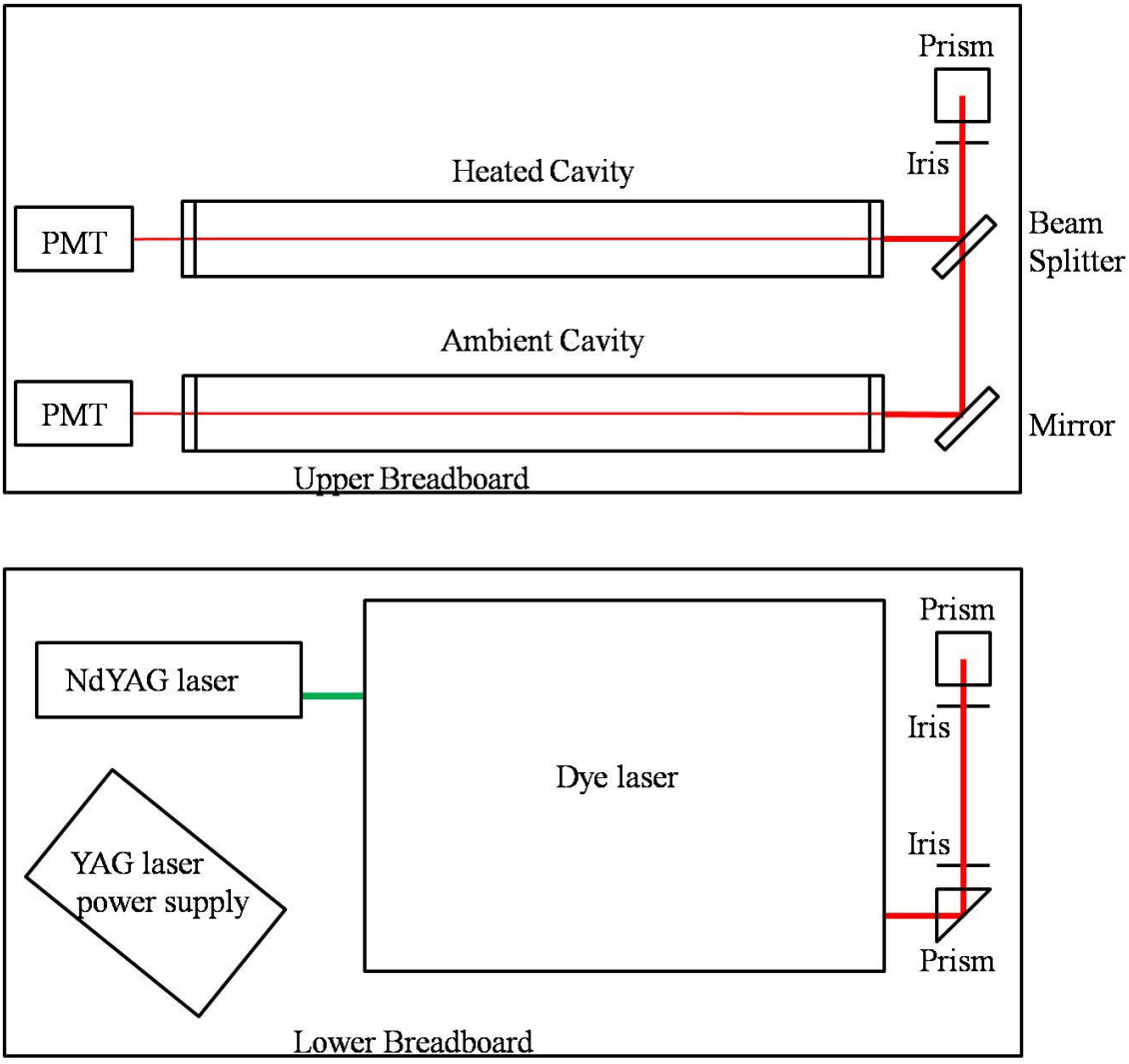

Figure 2.3. Schematic of the optical layout for the lower and upper breadboards for the cavity ring-down instrument.

cavity optics and detectors. Prior to the insertion into the cavity, the beam from the dye laser propagates through another iris to minimize the laser spot size at the far end of the optical cavities. A 50/50 beam splitter (Thorlabs, BSW10) separates the laser pulse into each of the optical cavities.

Each cavity consisted of two 2 cm diameter, 6 m radius of curvature, dielectric coated mirrors (Los Gatos Research), separated by 94 cm. The cavity ring-down mirror reflectivity is 99.99878% at 662 nm, to give an ideal τ_0 value of 250 μs. Each mirror was mounted in a custom-made 3-point adjustment cavity ring-down mount, pictured in Figure 2.4, with alignment screws of 100 TPI (turns per inch). Welded to the mount were two 1/8 in. stainless steel tubes to allow for purging of the mirrors with dry nitrogen (Botco, 99%) at a flow of 100.0 sccm (cubic centimeters per minute at standard temperature and pressure) to maintain mirror cleanliness. The nitrogen purge proved effective in preventing degradation of the cavity mirror reflectivity, which was observed to remain constant or to improve slightly during a run. The mirror mount was welded to a flange connected by a flexible bellow (Kurt. J. Lesker) to maintain a seal with the cavities, also seen in Figure 2.4.

Light transmitted through the rear cavity mirror is collected through a 610 nm longpass colored glass filter (Thorlabs, FGL610) to reject stray light at wavelengths below 610 nm, through a 2.54 mm columnating lens onto the photomultiplier tubes (Hamamatsu, H6780-20). Signals from the PMTs are digitized on a 14-bit PCI oscilloscope card (Gage Applied Technologies, 14100) and are analyzed in Labview 8.0

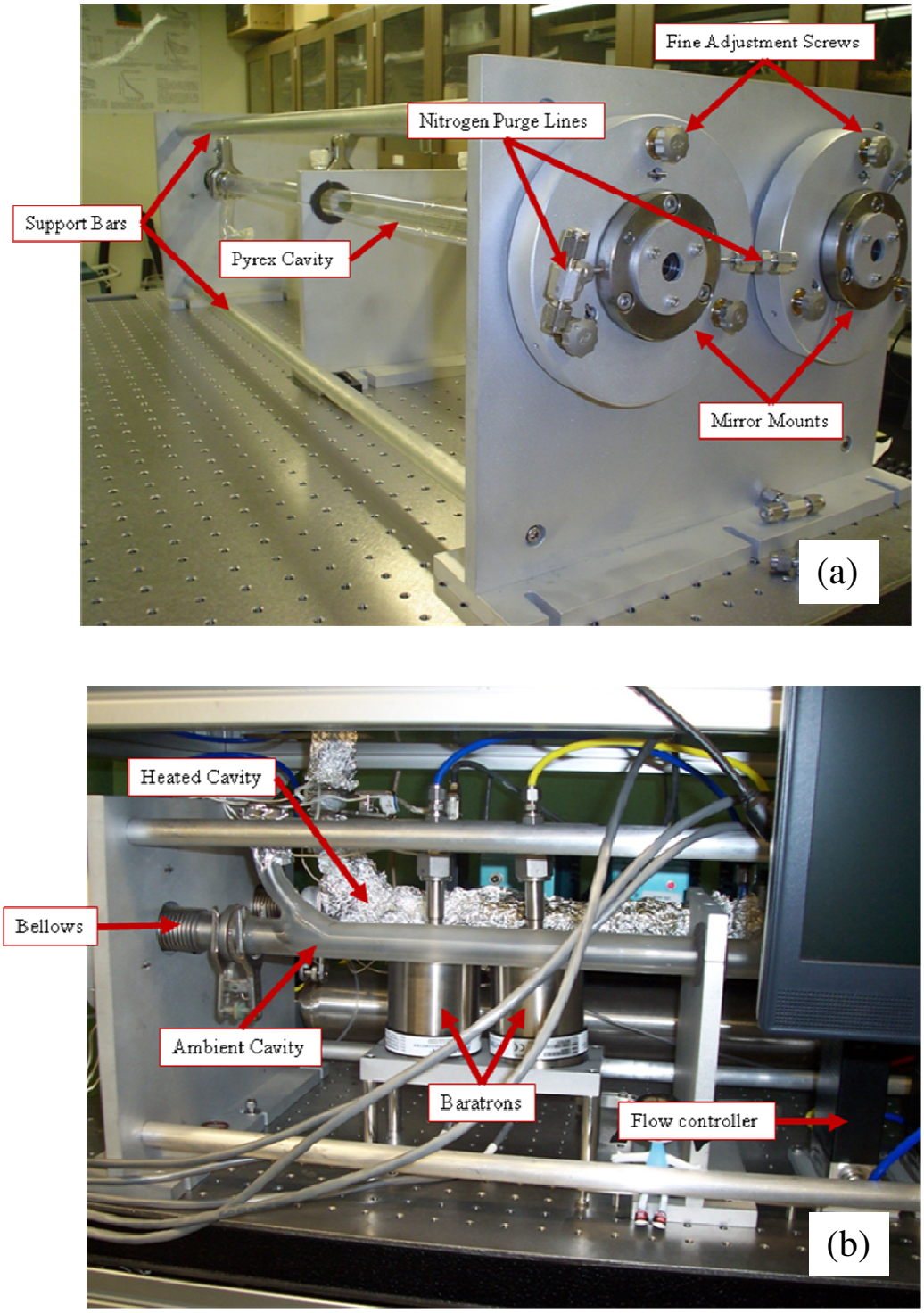

Figure 2.4. Images of the original instrument design. (a) Cavities and mirror mounts (b) Cavities, bellows, baratrons and flow controllers.

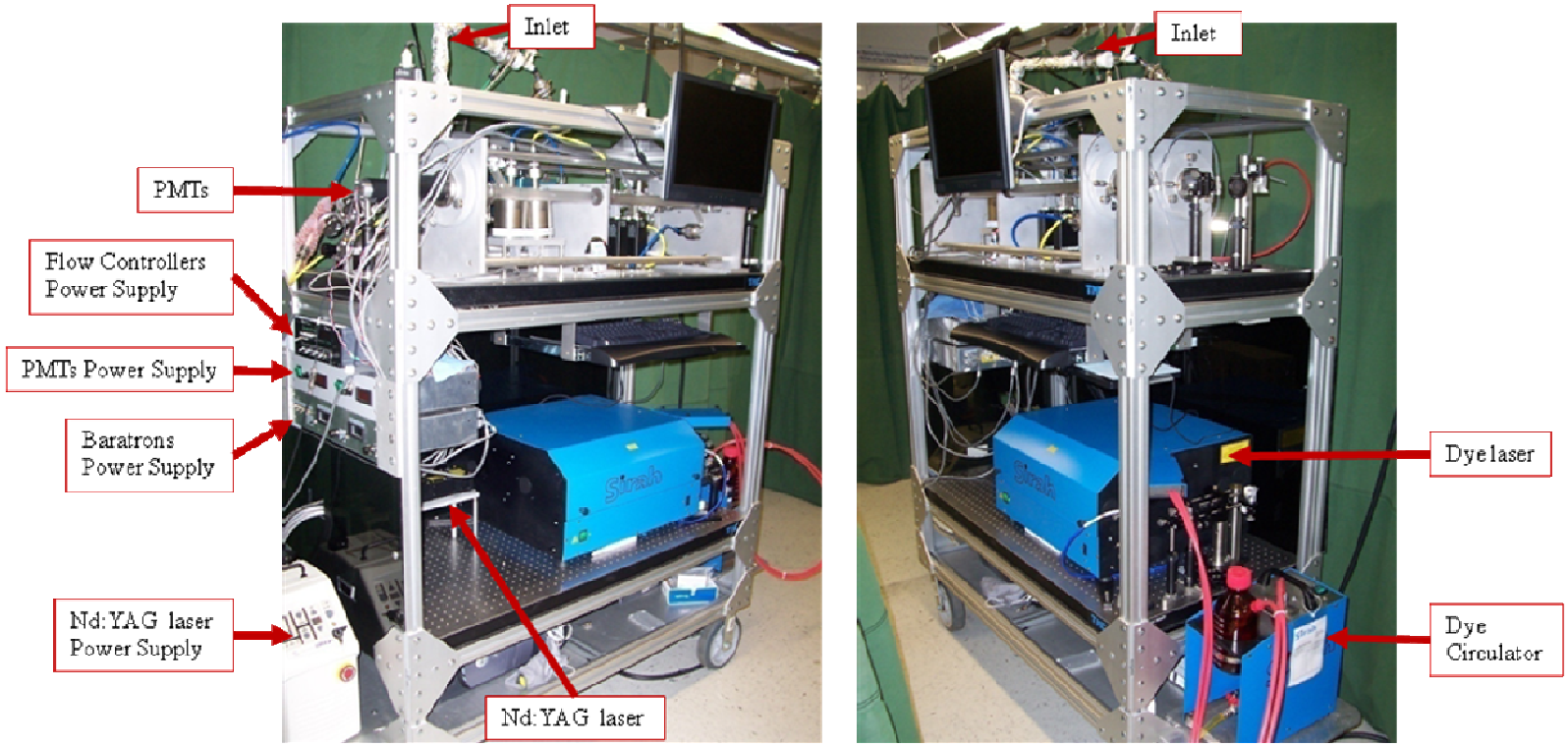

Figure 2.5. Images of the entire original CRDS instrumentation design.

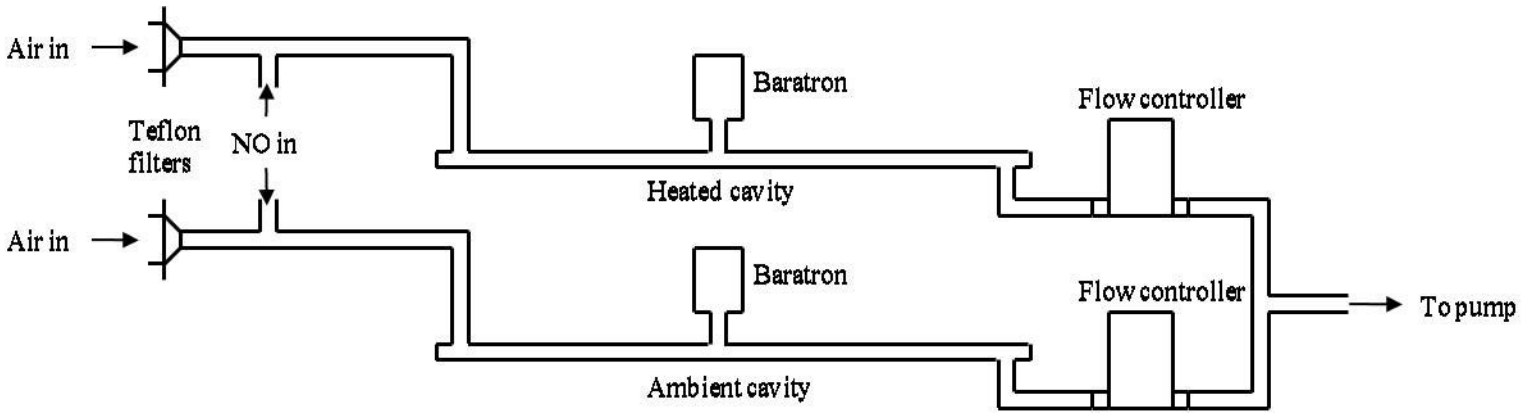

Figure 2.6. Schematic of the flow design for the initial instrumentation setup.

(National Instruments). A typical run included an averaging of 100 laser shots of the exponential decays, then a linear least squares fit to the natural logarithm of the exponential decay, which provided an individual time constant for each profile. The program recorded the averaged decay profile and the corresponding lifetime of that profile as a function of time.

The entire system is mounted on two 2×4 ft^2 aluminum breadboards (TMC), with the laser system below the cavity ring-down cells, attached to custom-made aluminum frame (Bosch, 45 series) housing. Figure 2.5 shows the entire cavity ring-down setup. The overall size and weight of the instrument are $1.32 \times 0.64 \times 1.8$ m^3 and approximately 270 kg, respectively.

The flow system, schematic shown in Figure 2.6, consisted of two 1 in. outer diameter (OD) Pyrex cells coated with inert halocarbon wax to reduce wall reactions. The inlets constructed for the cavities were designed from 0.75 in. OD Pyrex and were also coated with halocarbon wax. The flows were set to 12 slpm (liters per minute at standard temperature and pressure) and 8 slpm for the ambient and heated cavities, respectively, and correspond to a 3.25 s residence time for the system. The flows for each cavity were established by calibrated mass flow controllers (MKS, 1179A) at the output of the cells. A belt-driven pump (Welch, 1400) was common to both flow controllers.

When field testing, it is important to maintain a constant temperature of the outside, sampled air with the inside air temperature where the instrument is housed. This is imperative to minimize the shifts in the N_2O_5 to NO_3 equilibrium and to prevent

possible condensation of water inside the tubing. The temperatures were observed using K-type thermocouples. If necessary, slight heating of the inlet tubing and ambient cell is performed to maintain a constant temperature with the outside air. Insulation of the inlets and cavities also serves to minimize temperature drops between the typically warmer outside air and the inside temperature. The Pyrex cavity and inlet, wrapped in fiberglass insulated heat tape (Briskheat) controlled by a variac, maintains a constant temperature for the ambient channel along the optical cavity. The heated channel is designed similarly to the ambient channel. However, prior to entering the optical cavity, the sampled air was heated to approximately 120 °C for effective thermal decomposition of N_2O_5. The Pyrex cavity for the heated channel was maintained at a temperature of 80 °C. The temperatures for each channel, as well as the heated inlet temperature, is monitored by thermocouples through an analog to digital converter (National Instruments, USB-6009) interfaced with the Labview program. The pressures in the individual optical cavities were monitored with a baratron (MKS, 628B) at the midpoint of the cells. Pressures are recorded similar to the temperatures through the analog to digital converter. Typical pressure in the system, both cavities, was approximately 730 Torr.

Extinction of the ring-down signal in ambient air due to aerosol scattering and absorption can be quite significant and can give rise to shot-to-shot fluctuations in τ_0.[64] Removal of these aerosols is therefore required for highly sensitive CRDS measurements. In coincident with aerosol removal, the removal of a portion of the NO_3 and N_2O_5 to be detected cannot be avoided. A thin, 25 μm, Teflon PTFE filter (Pall-

Gelman) with 38 mm diameter and pore size of 2 μm is utilized at the mouth of the two separate inlets for removal of aerosols and to minimize loss of NO_3 and N_2O_5. Due to buildup on the filters, they are typically changed every 1-2 hours.

Even though laboratory measurements of N_2O_5 were obtained, a variety of issues caused failed attempts at measuring ambient N_2O_5 and NO_3 in the field. Substantial wall losses and ring-down instability were to blame for the absence of field measurements. Problems with wall losses occurred from the slow residence time of 3.25 s in the system because the inlets and cavities were too large in diameter. Also, in combination with the large diameter was the high pressure of 730 Torr throughout the system. Therefore, from the initial instrumental setup, numerous redesigns of the inlets, cells, and mirror mounts were made to obtain the current configuration described in detail below, also based on Brown's instrumentation.[50]

2.4 Current Experimental Design

The mirror mounts, housing the dielectric coated mirrors (Los Gatos Research), are separated by 94 cm. Each mirror is mounted in a commercially available 3-point adjustment purgeable cavity ring-down mount (Los Gatos Research), with alignment screws of 80 TPI (turns per inch). This mount is attached to a Conflat flange with a welded 1/8 in. tube for purging the mirrors with dry nitrogen (Botco) at a flow of 100.0 sccm. Unlike the previous design, there is only one purge tube per mirror mount. In addition, the mirror mounts are much more compact compared to the originals. A 3/8 in. compression fitting attaches the Conflat flange of the mirror mount to the cavity, rather than utilizing bellows. A schematic of the current design can be seen in Figure 2.7.

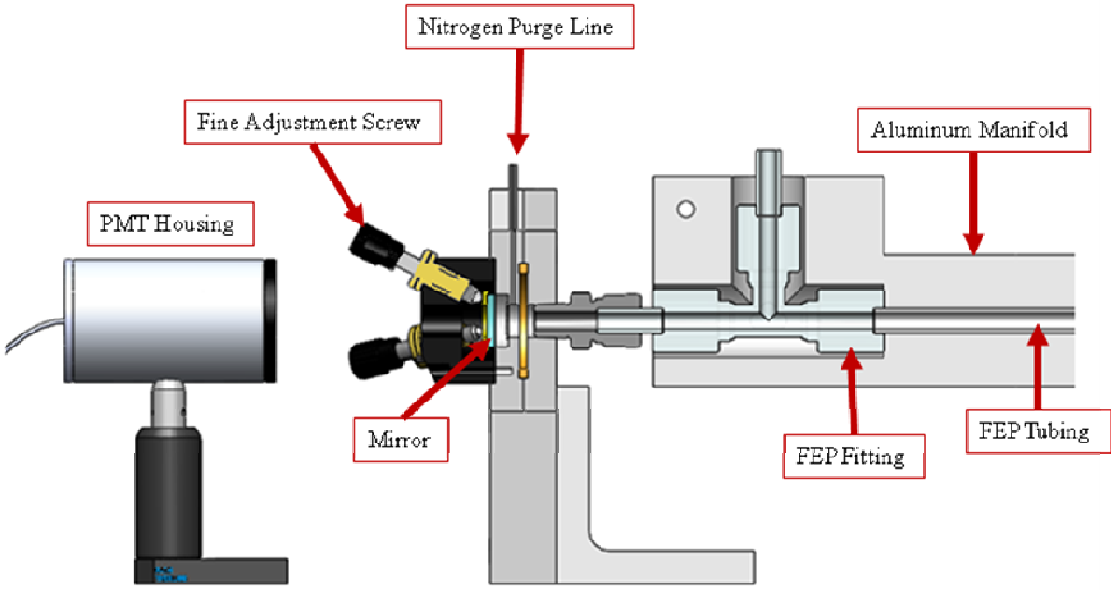

Figure 2.7. Schematic of the current mirror mount design. Also shown is the FEP tubing cavity that is housed in an aluminum manifold.

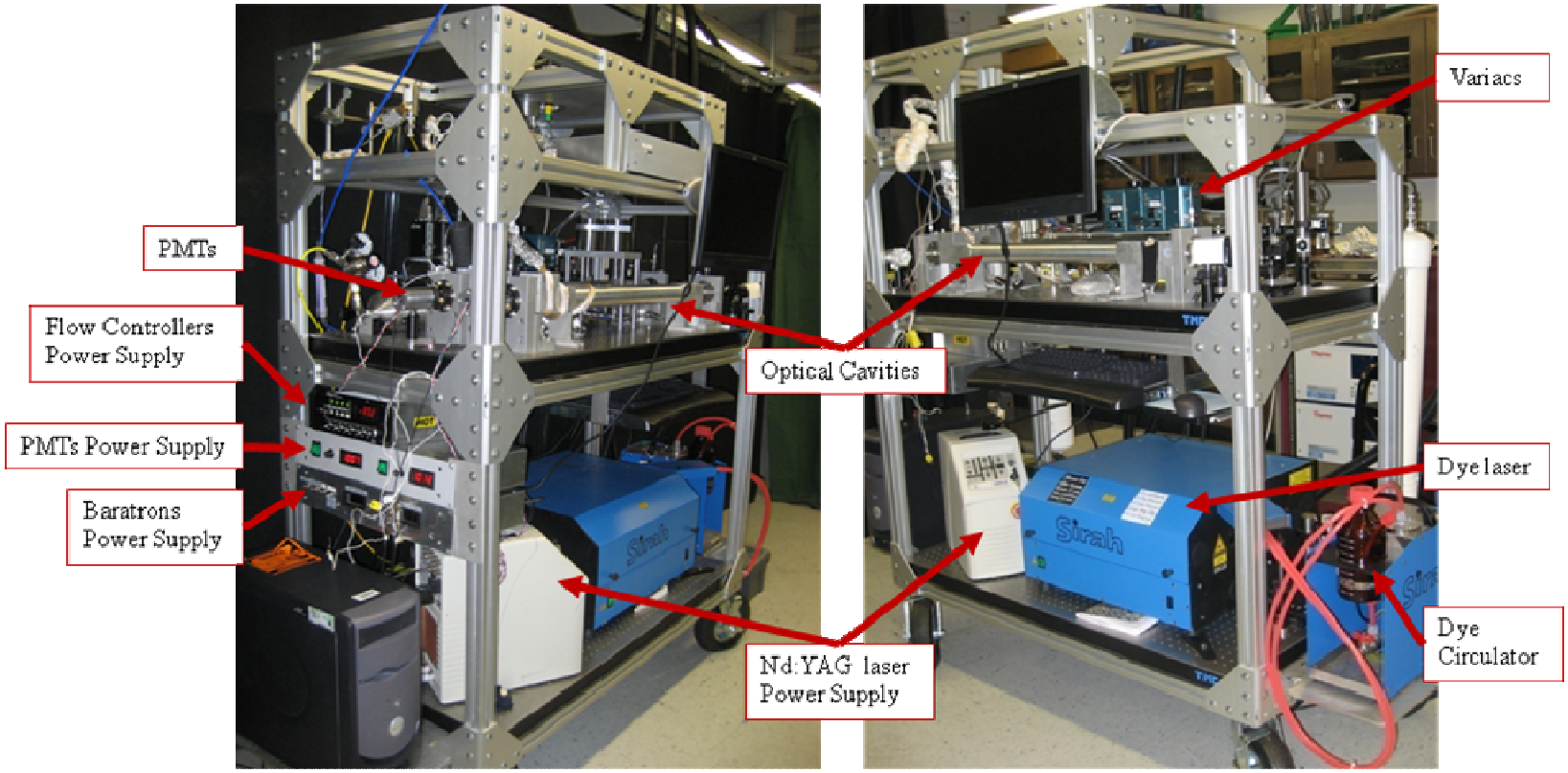

Figure 2.8. Images of the entire current CRDS instrumentation design.

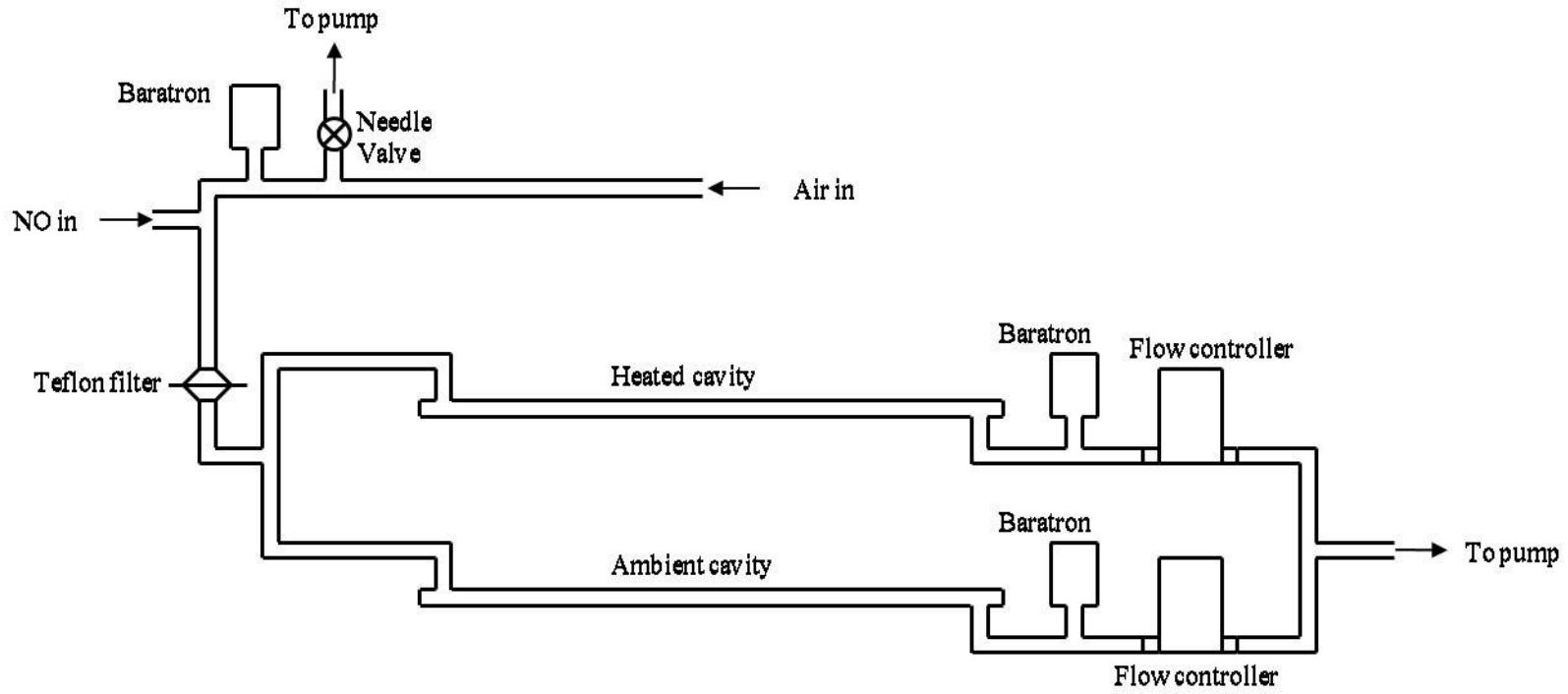

Figure 2.9. Schematic of the flow design for the current instrumentation setup.

The housing for the CRDS instrument has been altered from its original design, as depicted in Figure 2.8. With the addition of shelves on either side of the instrument housing to store the computer tower and the dye circulator, the overall size has only increased its length in comparison to the previous design. The current dimensions of the instrumental cart are $1.8 \times 0.75 \times 1.8$ m^3, with the total weight of the instrumental apparatus remaining the same at approximately 270 kg.

The redesigned flow system is comprised of three components: the initial, fast-flow portion that transports the air sample from outside; a Teflon® membrane filter that removes aerosols in the system; and a slow-flow part that brings the air sample into the two optical cavity cells. A schematic of the flow system is displayed in Figure 2.9. The initial portion of the flow system is constructed of 25 ft. of commercial 1/4 in. outer diameter (OD), 1/16 in. inner diameter (ID) PTFE fittings and tubings, while the slow-flow portion is constructed of commercial 3/8 in OD, 1/4 in. ID FEP fittings and tubings. The fast-flow region employs an oil-free diaphragm pump (Vacuubrand, ME4 NT), measured at 52 slpm, to pull the sampled air in through the 25 ft inlet. The overall flow rate through the fast-flow region is approximately 60 slpm, which is the sum of the 52 splm inlet diaphragm pump and the totaled 8 slpm controlled flows in the slow-flow system. The slow-flow portion samples air from the fast-flow region at a tee-connection prior to the membrane filter. The filter is mounted in a PTFE housing that allows the FEP tubing to fit inside and be butted up against the filter. Immediately following the membrane filter, the slow-flow region is split into two air samples that are controlled by

individual electronic mass flow controllers (MKS, 1179A) at the cell exhausts. A second diaphragm pump (Vacuubrand, ME4) is common to both cells.

Monitoring of the pressure in the individual optical cavities occurs at the exit portion of the cavities, rather than at their midpoint. Pressure is recorded as described in the original design, with the addition of a monitor to measure the inlet pressure (MKS, 722B). Typical pressures in the fast-flow region are 350-375 Torr, while pressures in the slow-flow region are 300-315 Torr. Running with decreased pressures shortens the residence time to 0.17 s through the system and in turn minimizes wall loss of NO_3 and N_2O_5. Pressure pulsations were also observed, which gave rise to fluctuating ring-down decays. Ballasts constructed of 3 ft long, 4 in. diameter PVC tubing with two Scotch-Brite sponges secured inside and capped with 4 in. to 1/2 in. adaptors were placed in-line for each pump. This provided pulsation dampening to minimize the pressure fluctuations in the cell cavities.

With the cavities constructed from 3/8 in. FEP Teflon® tubing, an aluminum manifold was designed for structural support as well as providing a medium for heating the cavity. The inner portion of the manifold is machined to the shape of the tubing and fittings, and is split into a top and bottom half that bolt together for easy replacement of the tubing. The manifold design with the mirror mounts are pictured in Figure 2.10. The aluminum manifold, wrapped in heat tape controlled by a variac, maintains a constant temperature for the heated channel along the optical cavity, including the inlet and exhaust tee-fittings. The manifold and optical cavity is maintained at a temperature

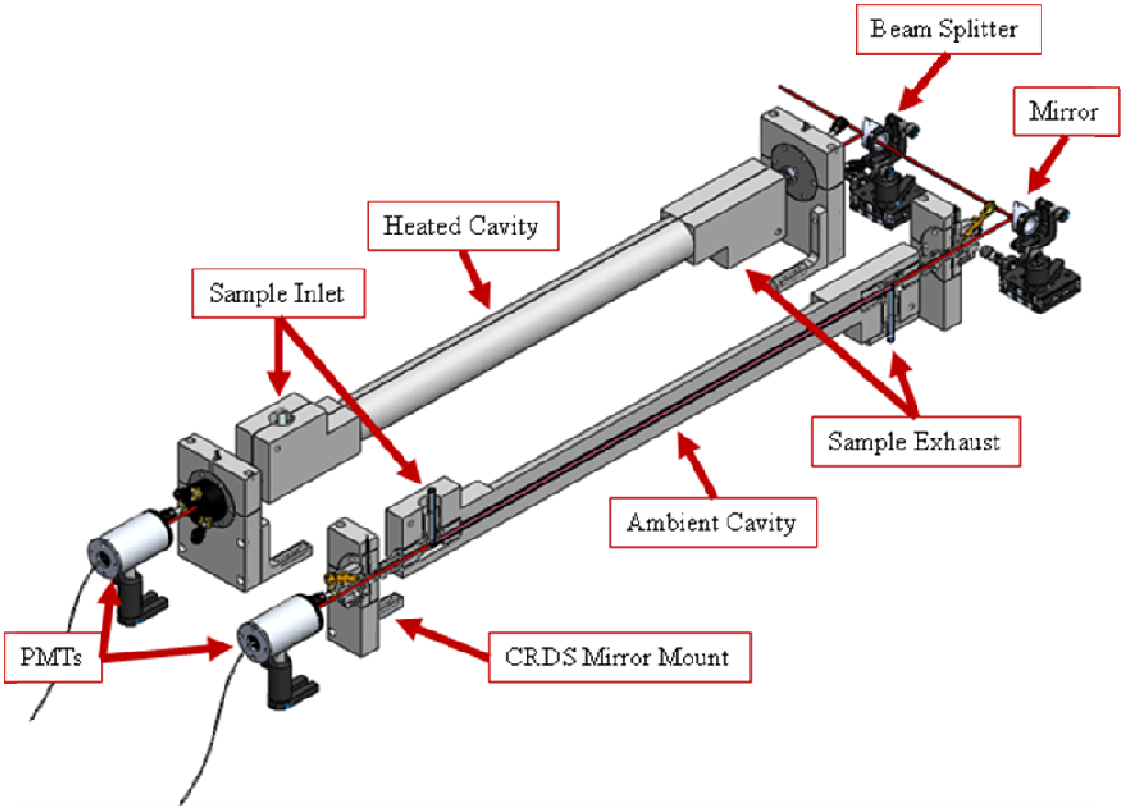

Figure 2.10. Current optical cavity design with FEP tubing housed in aluminum manifolds.

of 75 °C, with the inlet set at approximately 100 °C. The ambient cavity is designed similarly to the heated cell, which allows for slight heating if necessary to obtain a constant temperature with the outside air. Temperatures are still monitored and recorded as in the previous design with K-type thermocouples to an analog to digital converter.

2.5 Data Acquisition

As mentioned briefly in a previous section, ring-down signals from the PMTs are digitized on a PCI oscilloscope card (Gage Applied Technologies, 14100). The heated channel measuring N_2O_5 + NO_3 is connected to channel A of the oscilloscope, while the ambient NO_3 cavity is connected to channel B. The oscilloscope is triggered externally *via* the Q-switch sync from the Big Sky YAG laser, set at repetition rate of 10 Hz. Software development kits provided by Gage Applied Technologies allow for the oscilloscope signal to be transferred into Labview 8.0 (National Instruments). The Labview program, screen shot seen in Figure 2.11, is written to read the separate ring-down decays from both channel A and channel B, while plotting each as a function of voltage versus time in microseconds. The natural logarithm of each exponentially decaying ring-down is calculated and then plotted alongside the ring-down decays. A gate or a portion of the ring-down trace is selected prior to calculation of the natural logarithm, as displayed previously in Figure 2.1. Typically the first 25 μs of data displays some curvature in a log-linear scale and is therefore excluded. The gate also truncates the end of the ring-down decay; this value depends on the overall ring-down

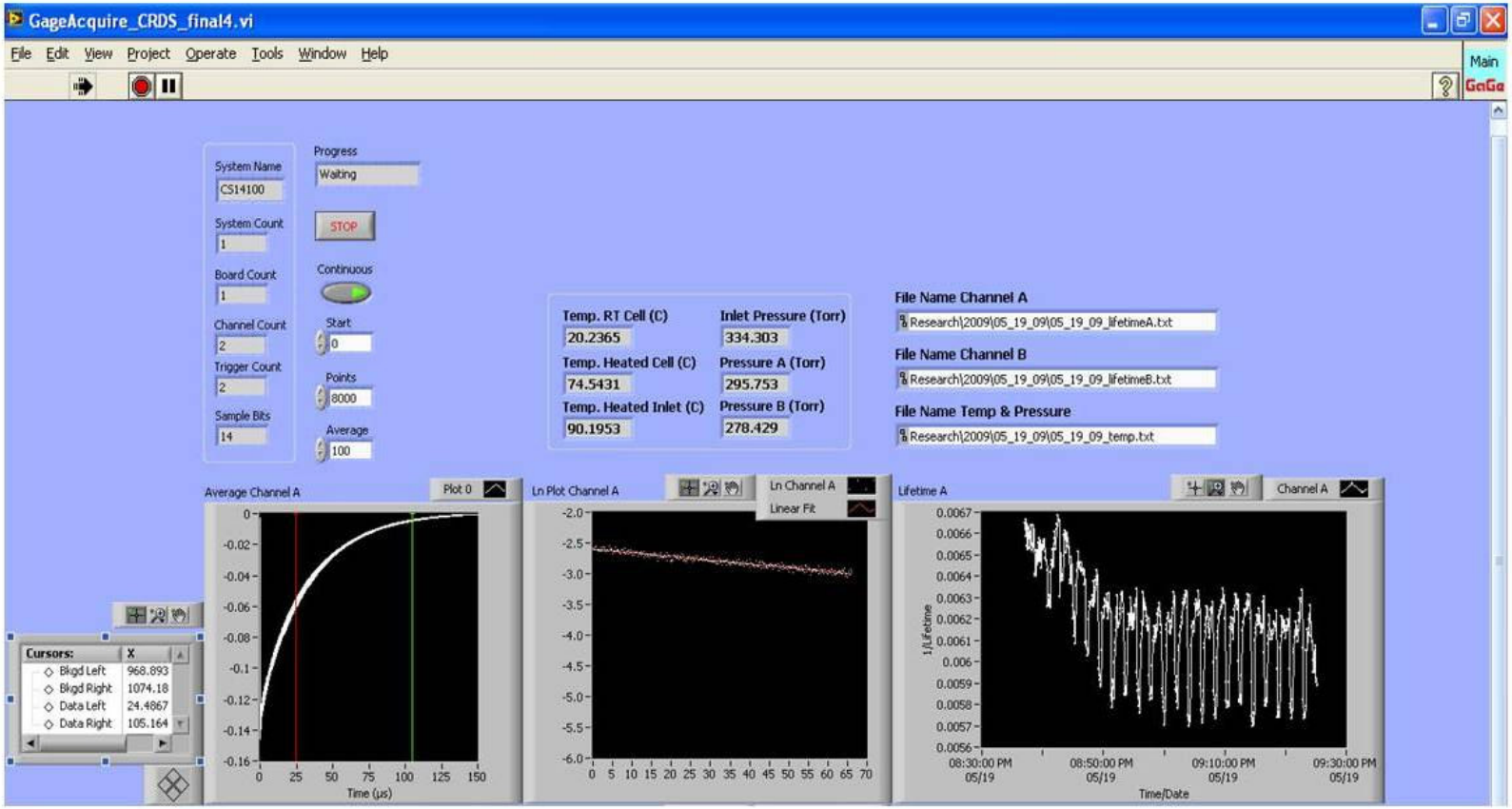

Figure 2.11. Labview 8.0 program front panel for data acquisitioning. Only channel A is pictured above; however for the program the same plots for channel B can be viewed directly below the plots for channel A.

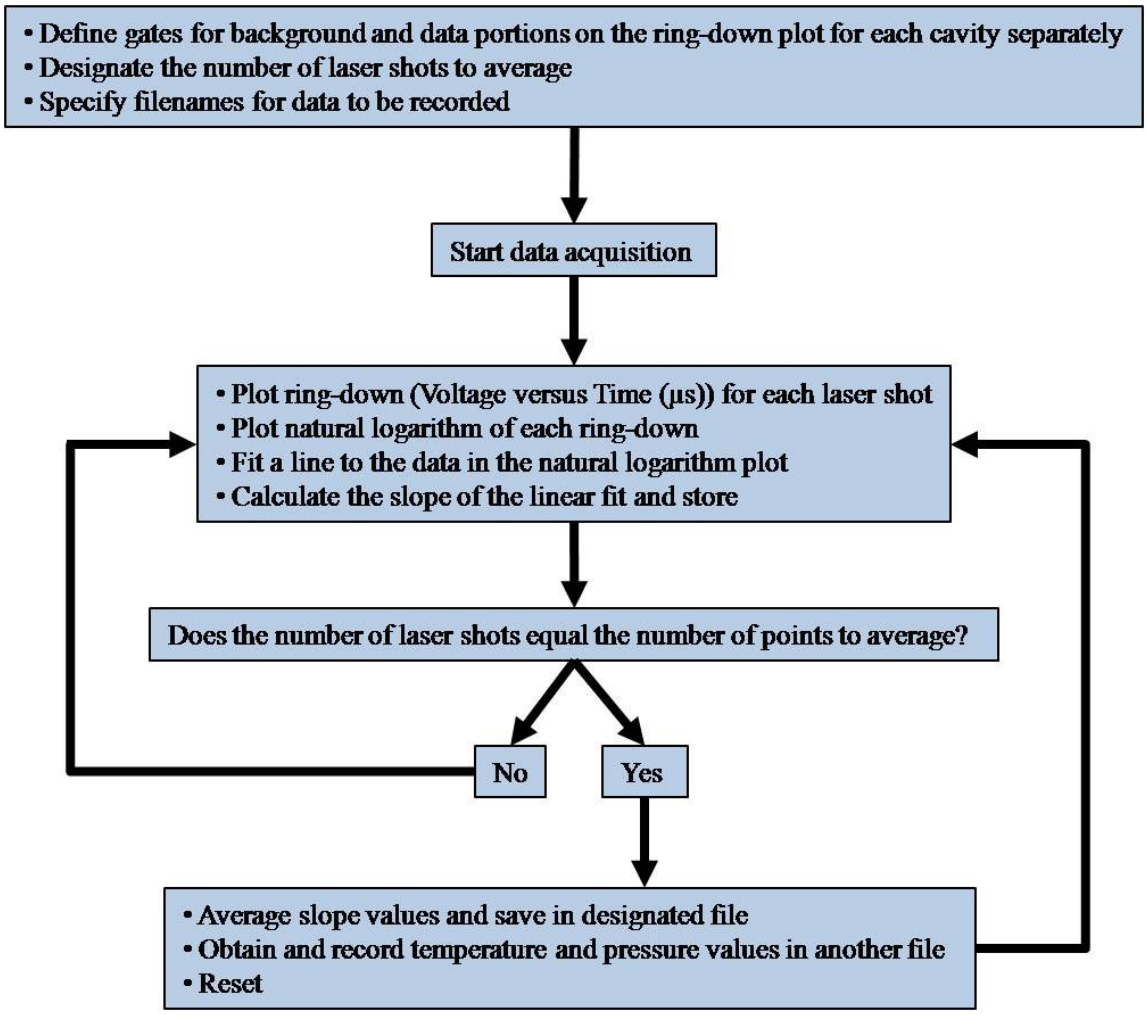

Figure 2.12. Flowchart for data acquisition in Labview for the CRDS instrument.

time for τ_0. Truncation of τ_0 ensures that the natural logarithm is linear for the highly variable shorter decay profile, τ, when the absorbing species is present. The slope of the natural logarithm provides a value of 1/lifetime in μs^{-1}. An average of 25 consecutive calculated slopes is determined and provides the plotted 1/lifetime value. An average of 25 represents the number of laser shots. With the laser set at 10 Hz, this therefore corresponds to a 2.5 s integration time. At the same time the averaged slopes provide the plotted 1/lifetime value, the Labview program is also set to probe the temperatures and pressures. A flowchart of the program is seen in Figure 2.12.

Temperatures for the heated inlet, the heated cavity, and the ambient cavity are monitored alongside each of the pressures for the heated cavity, the ambient cavity, and the inlet upstream from the membrane filter. A data acquisition, DAQ, board (National Instruments, USB-6009) that is compatible with the Labview software allows for the temperature and pressure information to be pulled directly into the same Labview program as the ring-down signals with a sub-vi called DAQ Assist. The temperatures displayed while the program is running are an approximate temperature to simplify the program, but can be calculated exactly at a later time. K-type thermocouples provide a microvolt reading that corresponds to a temperature *via* the polynomial expressed in

Equation 2.5:

$$T(°C) = a_0 + a_1 v + a_2 v^2 + a_3 v^3 + a_4 v^4 + \ldots + a_n v^n \qquad (2.5)$$

$$\begin{aligned}
a_0 &= 0.0 \\
a_1 &= 2.508355 \times 10^{-2} \\
a_2 &= 7.860106 \times 10^{-8} \\
a_3 &= -2.0503131 \times 10^{-10} \\
a_4 &= 8.31527 \times 10^{-14} \\
a_5 &= -1.228034 \times 10^{-17} \\
a_6 &= 9.804036 \times 10^{-22} \\
a_7 &= -4.413030 \times 10^{-26} \\
a_8 &= 1.057734 \times 10^{-30} \\
a_9 &= -1.052755 \times 10^{-35}
\end{aligned}$$

where v is in microvolts (μV). The DAQ is not capable of reading such low voltages and therefore requires an amplifier to convert microvolts to millivolts before being transferred into the DAQ. The mV reading for the temperatures is the recorded value into the text file. Similarly, the pressures are recorded from the output voltage (0-10 V) from each pressure transducor. The voltage reading is transferred into the DAQ and corresponds to a pressure (0-1000 Torr). Therefore, this only requires a multiplication of the voltage by 100 to give the pressure.

The time and date (synced to the computer), 1/lifetime value, temperatures and pressures are all written into a text file at this point. Once completed, the program loops back through the entire cycle and plots another point on the 1/lifetime versus time plot. The program continues through the loop until stopped by the user.

2.6 Chemical Zeroing

Periodic and effective zeroing of the instrument is necessary to account for any drifting in the background signal, τ_0. This is accomplished by chemically removing NO_3 with the addition of NO upstream of the detection region prior to transmission through the Teflon membrane filter. The reaction

$$NO_3 + NO \longrightarrow 2NO_2 \qquad (2.5)$$

is fast, with a rate of 2.6 x 10^{-11} cm^3 $molecule^{-1}$ s^{-1} at 298 K.[2] With NO at an addition of 3×10^{13} molecules cm^{-3}, this corresponds to a pseudo-first order lifetime for NO_3 of approximately 1×10^{-3} s at 80 °C and 1 atm.[2] This is ensures complete removal of NO_3 before reaching the detection region of the flow cell (0.17 s).

By chemically zeroing with NO, both measurements, τ and τ_0, include the same interference contributions from water vapor at the single wavelength of 662 nm at the absorption maximum for NO_3. The reaction of NO with NO_3 does lead to the formation of two NO_2 molecules. Therefore, with the addition of NO, production of twice as much NO_2 as there was NO_3 is now present in the detection region, adding an absorption during the "zero" measurement. The effect is twice the ratio of the absorption cross section of NO_2/NO_3 at 662 nm equaling approximately 2×10^{-4}, which leads to a negligibly small reduction in the NO_3 effective cross section. Thus, chemically zeroing with NO is an ideal method for determining the baseline measurement.

3. LABORATORY OBSERVATIONS

3.1 Introduction

In this section, initial laboratory measurements validate the readiness of the CRDS instrument for field testing. Verification of NO_3 detection is shown by the observed absorption spectrum. Successful chemical zeroing of the instrument by addition of NO upstream of the mirror cavity is demonstrated. In addition, the determination of the ideal N_2O_5 decomposition temperature provides complete conversion of N_2O_5 to the detected NO_3.

3.2 N_2O_5 Synthesis

All observations of NO_3 in the laboratory required the thermal decomposition of N_2O_5. Synthesis of solid N_2O_5 was accomplished in a Pyrex flow reactor by mixing NO_2 with excess O_3 similarly to the preparation described by Davidson and coworkers.[65] Dried oxygen (Botco) flowed through a commercial bench top ozone generator (Pacific Ozone Technology, L21) to produce ozone at approximately 4-6%/wt. The NO_2 (Aldrich, ≥99.5%) is collected in a Pyrex trap in a dewar of liquid nitrogen. Once enough NO_2 is collected, the trap is transferred into a second dewar that is maintained at a temperature of approximately 240 K with acetone and dry ice. The NO_2 trap is then placed in-line between the ozone generator output flow tube and the second Pyrex trap used to collect the synthesized N_2O_5. Figure 3.1 displays the setup for N_2O_5 synthesis. A third Pyrex bubbler containing mineral oil is located after the trap collecting N_2O_5. This allows for the monitoring of the ideal ozone flow rate of approximately 3-5 bubbles

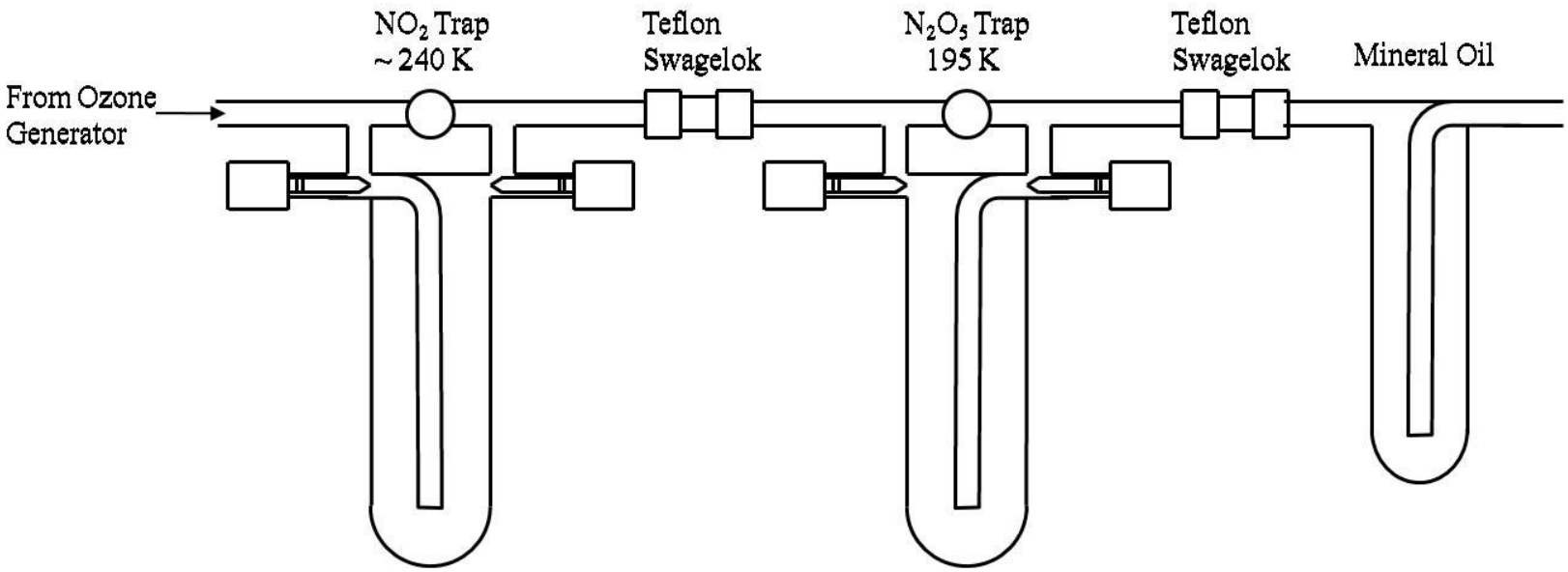

Figure 3.1. Apparatus for N_2O_5 synthesis.

per second through the mineral oil. Once the trap containing NO_2 is placed in-line, the ozone flow is adjusted with a needle valve at a t-joint prior to the NO_2 trap. The system allows the ozonised oxygen to flow through, collecting and reacting with the NO_2, forming N_2O_5 in the second Pyrex trap held constant at a colder temperature of 195 K with acetone and dry ice. Once completed, the solid white N_2O_5 sample is removed from the system. Excess unreacted NO_2 is then removed by allowing the sample to warm to 268-273 K while pumping on it for several minutes. The sample remains stored in a dewar with acetone and dry ice in a freezer until use. Successful N_2O_5 sample preparation was verified by the UV spectrum obtained with an Oriel LineSpec™ Linear Array Spectrometer, shown in Figure 3.2. The spectrum features are in good agreement with NASA JPL[2] and Osborne *et al*.[66]

3.3 NO_3 Observation

Detection of the nitrate radical has been confirmed by the absorption spectrum taken by the CRDS instrument. The absorption spectrum was obtained by introducing a small concentration of N_2O_5 into the main flow of ambient air from the laboratory and thermally decomposing the sample to NO_3 and NO_2. A schematic depicting the introduction of N_2O_5 sample and the flow of the system is shown in Figure 3.3. The flow of N_2O_5 was established by flowing argon (Botco) through a flow controller (MKS, 1179A) at 20 sccm into the Pyrex trap containing the N_2O_5 sample at 195 K. A dry ice/acetone bath maintained the sample at 195 K throughout the run. The N_2O_5/argon mixture was then added to the bulk flow of ambient room air. The air sample passed through a Teflon® membrane filter prior to entering the heated portion of the inlet to

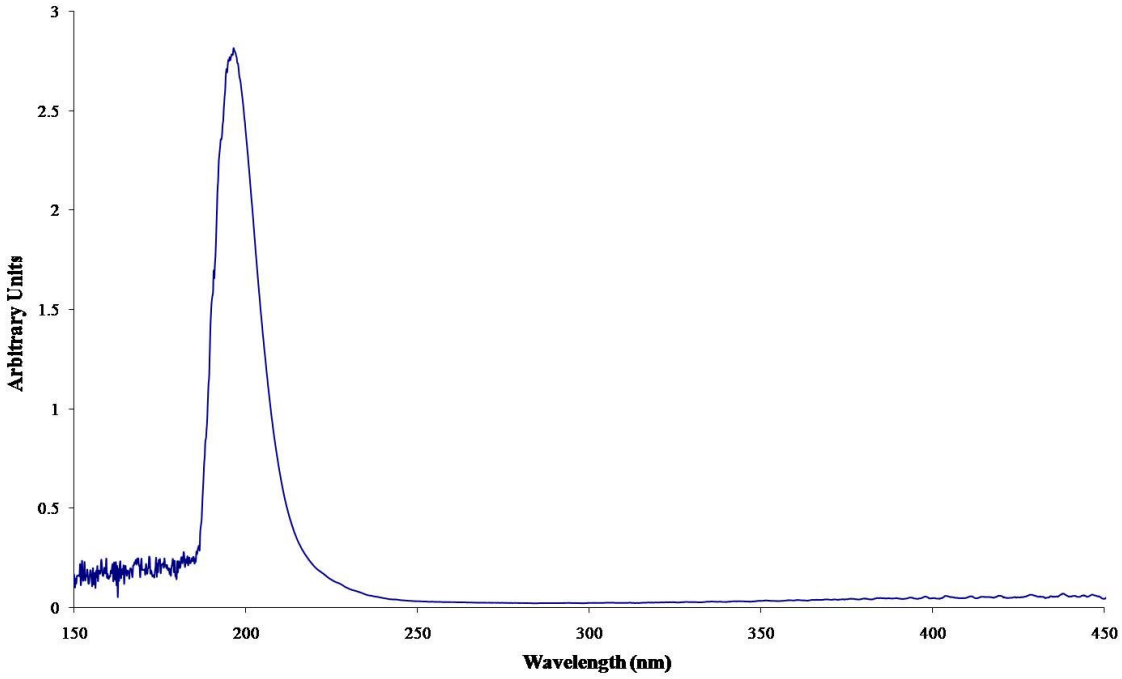

Figure 3.2. UV spectrum of N_2O_5. The spectrum was obtained for verification of successful N_2O_5 synthesis.

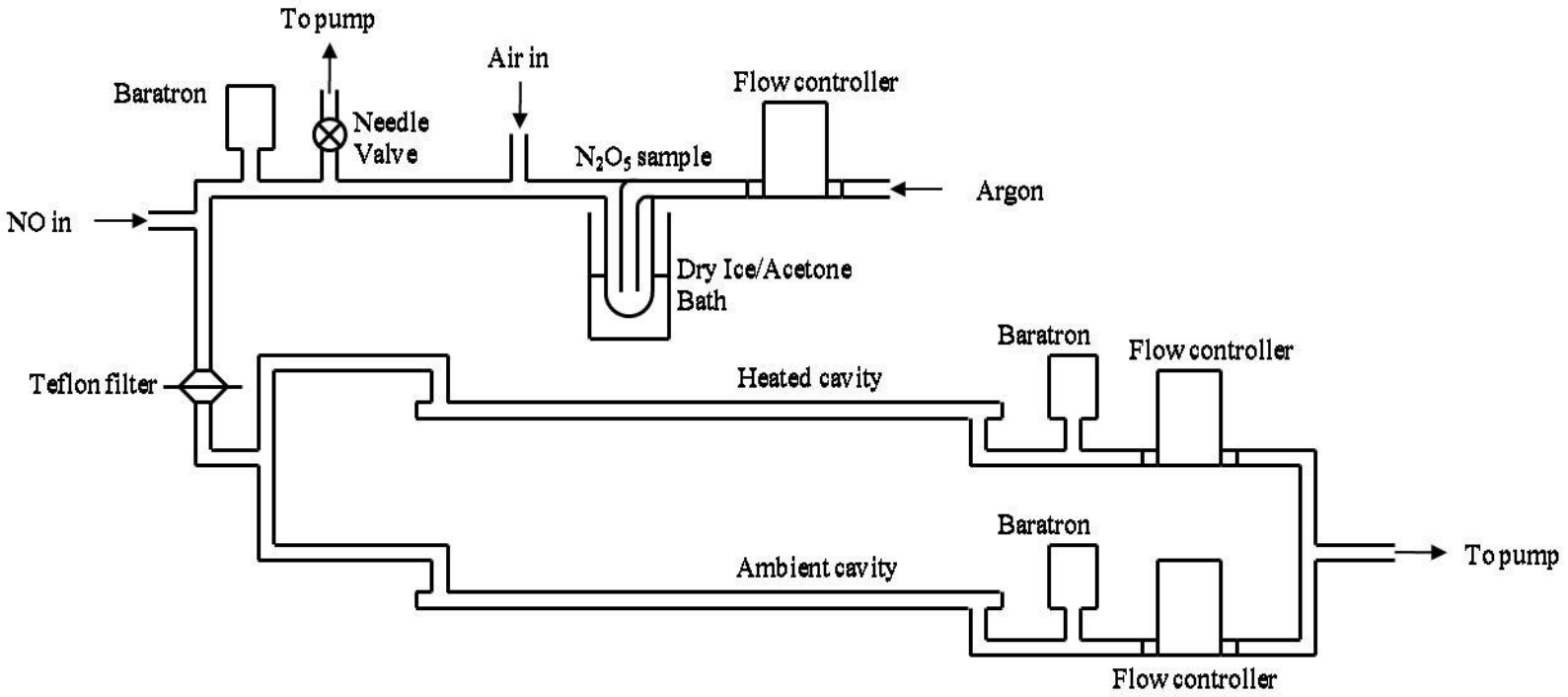

Figure 3.3. System setup for flow during calibration with N_2O_5 sample.

trap any unwanted particles from the room air. The inlet was held constant at 120 ˚C to allow for sufficient decomposition of the N_2O_5 sample, while the optical cavity was maintained at 80 ˚C during the experiment.

The laser was tuned between 650 and 675 nm, in increments of approximately 1 nm. At every third step, the laser wavelength was set equal to 662 nm, the NO_3 absorption maximum. Ring-downs were recorded at a 2.5 s integration time, corresponding to 25 laser shots. The raw data recorded is shown in Figure 3.4 as $1/\tau$ versus time elapsed. The relative NO_3 concentrations were then calculated using Equation 2.3, introduced in section 2. This CRDS-recorded spectrum and the NO_3 spectrum attained from NASA JPL[2] is displayed in Figure 3.5.

3.4 Chemical Zeroing

As discussed in section 2, a baseline measurement is required for the calculation of the absorber concentration, NO_3 for this instrument. This is accomplished *via* titration with nitric oxide, NO. A 3785 cm^3 stainless steel cylinder (Swagelok, 304L-HDF8-1GAL) is prepared containing a mixture of nitric oxide and nitrogen. The cylinder is first emptied to vacuum before the addition of NO. Nitric oxide (Aldrich, 98.5%) flows through a trap containing sodium hydroxide-coated silica (Ascarite® II, 8-20 mesh) to remove unwanted NO_2 and water before entering the cylinder. Approximately 5 Torr of nitric oxide is transferred into the cylinder. Then a buffer gas of nitrogen (Botco) fills the cylinder to about 500 psi. This corresponds to roughly 0.02% nitric oxide in nitrogen, or approximately 3×10^{15} molecules cm^{-3} of NO in the cylinder. For a typical field campaign, the experiment runs 12 hours a day, with the NO/N_2 mixture zeroing for

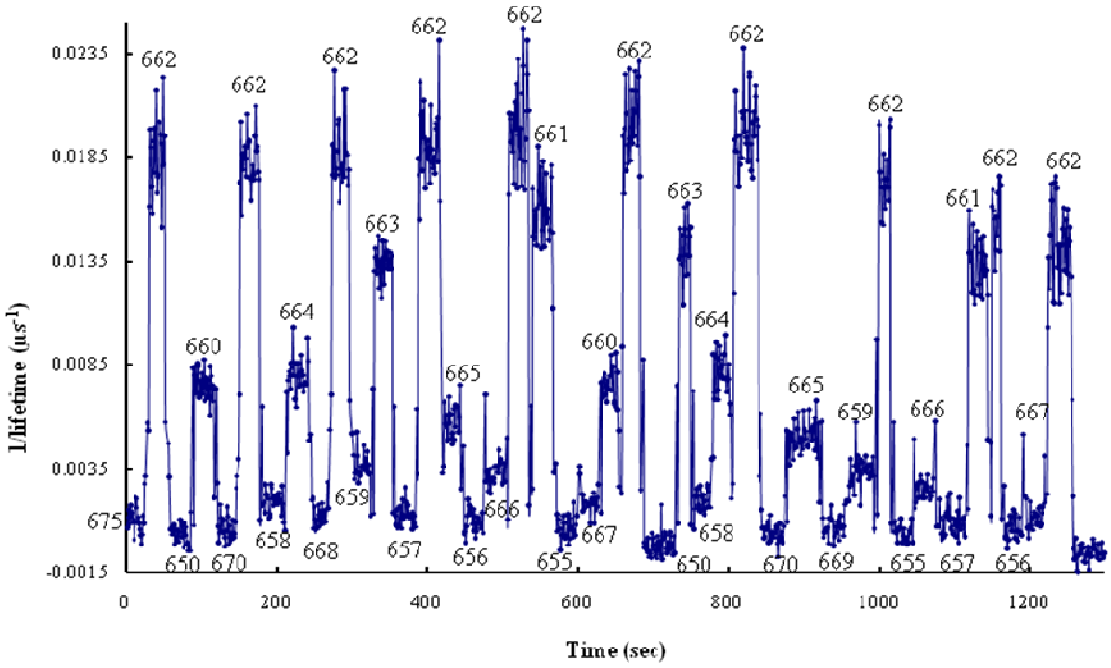

Figure 3.4. Time series of CRDS-recorded NO_3 radical spectrum. Data was recorded with a 2.5 s integration time on the original CRDS instrument design.

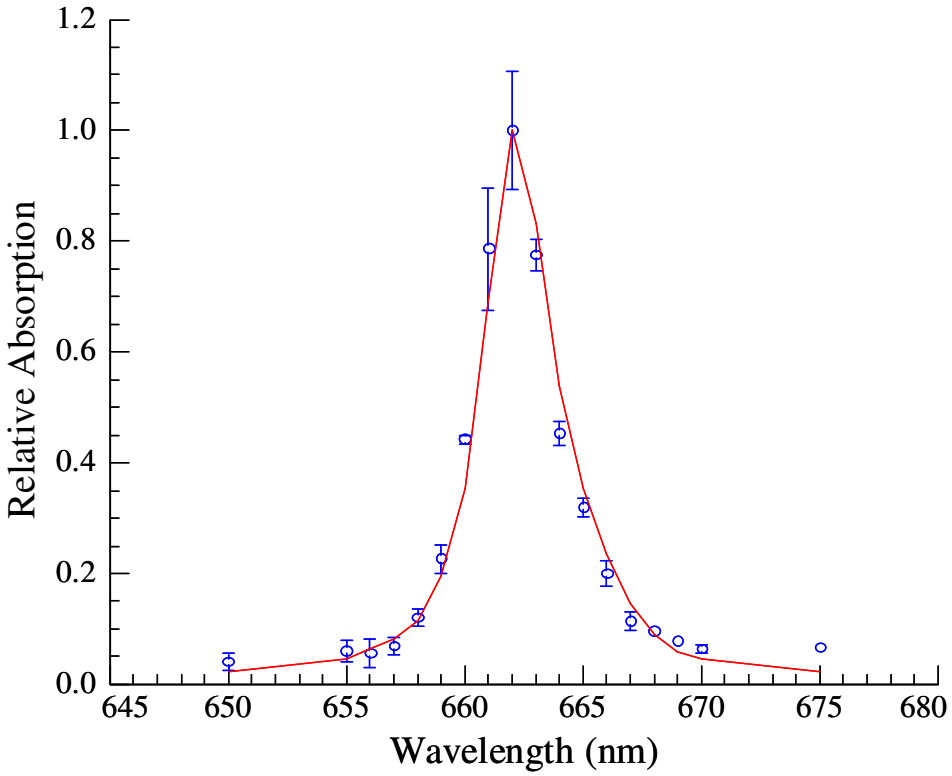

Figure 3.5. Absorption spectrum of the NO_3 radical. CRDS-derived data with a 25 laser shot average from the original CRDS instrument design is represented by open circles and the solid line is the normalized absorption spectrum from JPL 2006[24].

30 seconds every two minutes. This is equivalent to two weeks of operating the instrument every day before the titrant cylinder expires and needs to be replenished.

An ideal nitric oxide concentration of 1×10^{13} molecules cm^{-3} inserted into the system is accomplished by passing the NO/N_2 mixture through a flow controller (MKS, 1179A). The mixture concentration is carefully chosen to effectively titrate the nitrate radical in the system and to not produce a measureable concentration of NO_2. Verification of effective zeroing can be seen in Figure 3.6. The measurement started without the presence of the nitrate radical. N_2O_5 was then introduced into the system, similarly to that described for the measurement of the absorption spectrum above. Periodically nitric oxide was added through a flow controller at a rate of 90 sccm. In between the titrant cylinder and the flow controller, a trap containing sodium hydroxide-coated silica (Ascarite® II) allows for the removal of any NO_2 in the line that could lead to an increase in absorption and lead to contamination by increasing the extinction signal. The figure shows when the NO was added to the sampled air and when it was also shut off. Termination of the addition of N_2O_5 into the system provides another baseline measurement. It is observed that the zero efficiency with NO is 100%, which allows for accurate reproduction of τ_0. To also show that there was no contamination of NO_2 in the system, NO was again added after the N_2O_5 flow had ceased.

3.5 Thermal Conversion of N_2O_5 to NO_3

To provide accurate concentration measurements of N_2O_5, it is important to know the conversion efficiency of N_2O_5 to NO_3 and NO_2. Therefore, by measuring the NO_3 concentration as a function of inlet/cell temperature, the ideal conversion

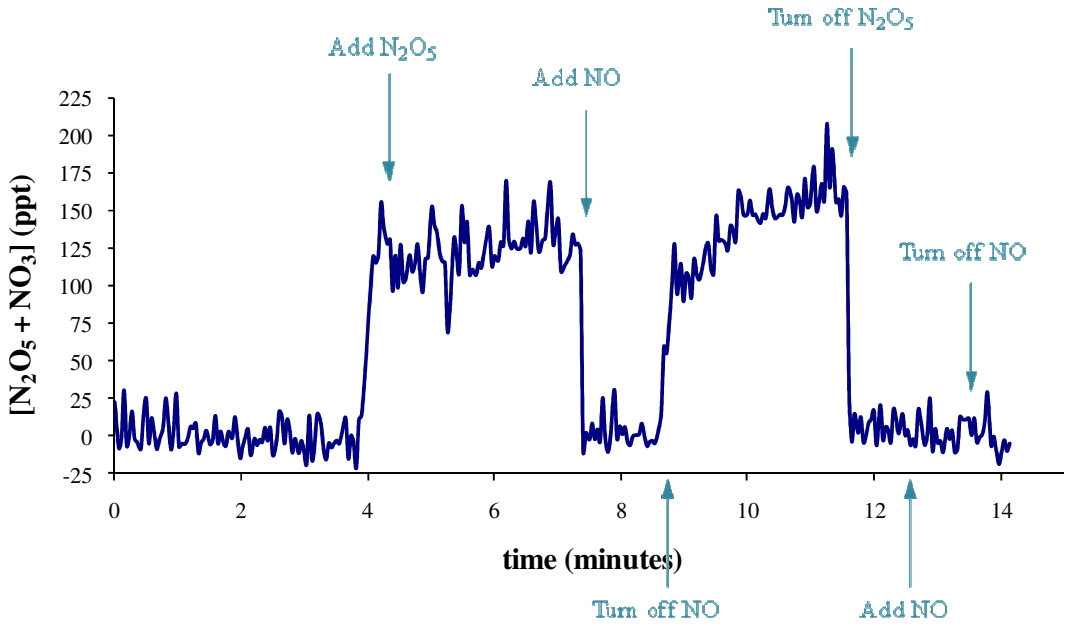

Figure 3.6. Chemical zeroing with NO with a 25 laser shot average.

temperature can be determined. This was accomplished by flowing synthesized N_2O_5 through the system similar to that described above. Measurements started with an inlet temperature of 158 °C and ended at room temperature, while keeping the cavity temperature constant at 75 °C throughout the run. The cavity remained heated to avoid ring-down instability caused by large temperature changes. Data was recorded every 2 seconds, corresponding to 20 laser shots. Equation 2.3 allows for the calculation of the NO_3 concentration. Figure 3.7 shows that as the temperature increases, the observed NO_3 concentration, or the conversion efficiency, also increases. The NO_3 concentration eventually plateaus and starts to slightly decrease. This is due to the increased wall losses at higher temperatures that cause immediate N_2O_5 decomposition in the system. Also plotted in the figure is the calculated conversion efficiency from the temperature dependent dissociation rate constant of N_2O_5 from Cantrell *et al.*[67] and the 0.17 s residence time of the system. Based on the data, the optimum preconverter or cracking temperature is between 85 and 100 °C.

3.6 Ring-down Stability

Fluctuations in the ring-down signal have a significant impact on the sensitivity of the instrument. Temperature fluctuations observed for the heated optical cavity oscillate between ± 2 °C from the desired temperature. The current setup employs variacs to control the fiberglass-insulated heat tape (Briskheat) temperature that is monitored *via* K-type thermocouples. The observed fluctuations are close to the specifications for K-type thermocouples, ±1.5 °C accuracy. An attempt to reduce the magnitude of the temperature fluctuations resulted in the utilization of a temperature

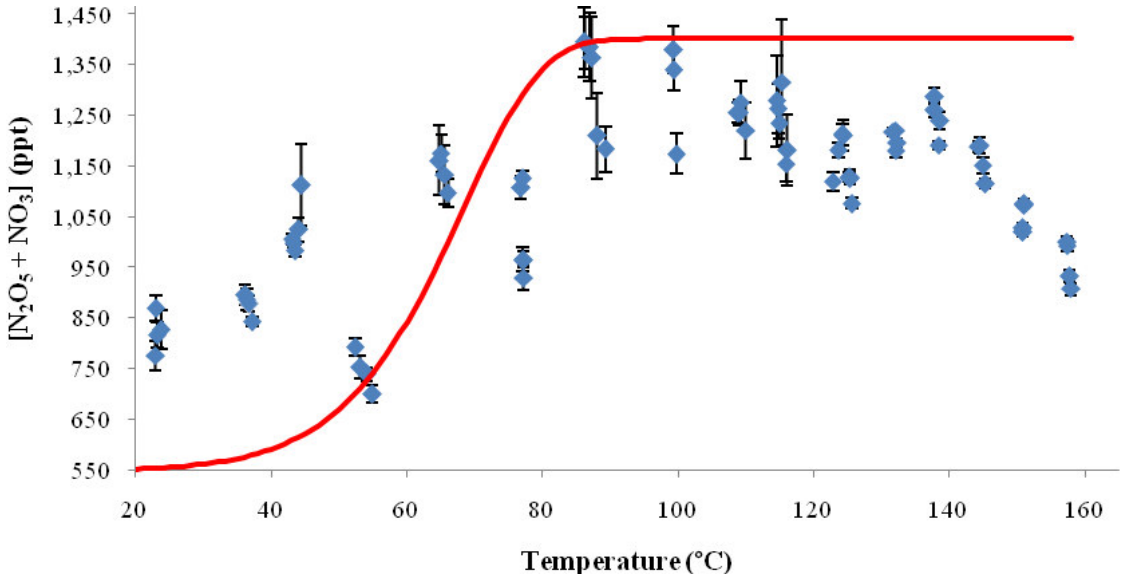

Figure 3.7. Relative N_2O_5 + NO_3 concentration as a function of preconverter temperature. The data points were recorded starting at 158˚C and letting the inlet cool to room temperature, while the red line corresponds to a calculation of the conversion efficiency of N_2O_5.

controller (Omega) in line with the heat tape and variacs. The minimal temperature fluctuations observed with the controller were ± 3 °C, with an also noticeably longer time to reach the desired temperature from ambient temperature. Therefore, the temperature controller use was discontinued and there was a reinstatement of the previous setup.

The possibility for the temperature of the nitrogen purge gas for the cavity mirrors varying significantly from the sampled air temperature was considered. Dubé *et al.*[50]suggested a mixture of 20% helium in zero air for mirror purging to correct for the thermal lensing that can possibly alter the optical alignment. For our instrument this mixture had no significant affect on the ring-down fluctuations. Thus, we reverted to the use of dry nitrogen for mirror purging.

If the laser beam from the dye laser is not produced with a uniform intensity profile, *i.e.* Gaussian profile, varying ring-down signals can be observed on a shot-to-shot basis. To produce a Gaussian beam profile, an optical spatial filter (Thorlabs, KT310) was placed in-line immediately after the first prism from the dye laser. An image of the spatial filter in our setup can be seen in Figure 3.8. Visibly, this cleaned up the laser beam profile; however, no noticeable difference in the ring-down fluctuations was observed.

Pressure pulsations were also measured and could be attributed to the diaphragm pumps responsible for flowing the sampled air through the system. Pressure dampening was possible with the construction of ballasts that were placed between the cavity pump

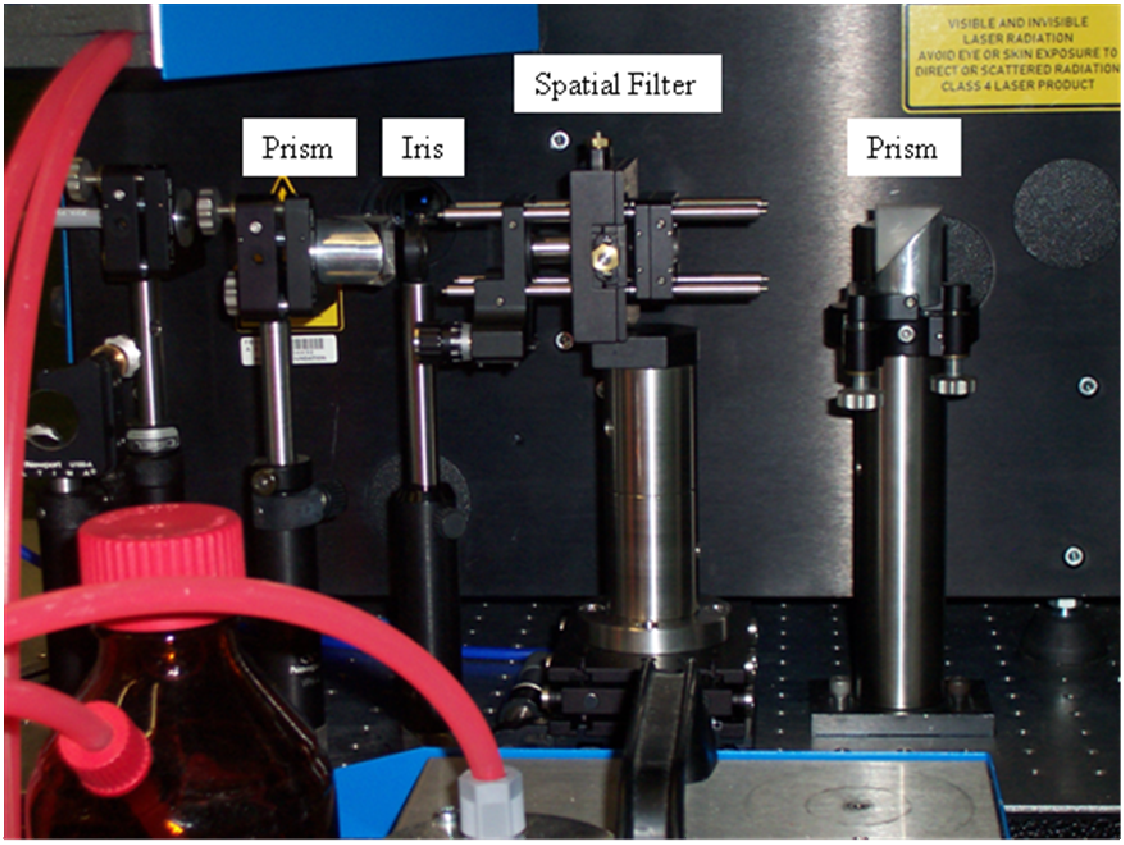

Figure 3.8. Optical spatial filter used to create a Gaussian beam from the dye laser before the beam is transported to the upper breadboard that houses the CRDS cells.

and the flow controllers. The ballasts were designed of PVC tubing that were 4 in. diameter and 3 ft long with Scotch Brite sponges placed inside. This addition made a considerable difference in ring-down stability and therefore a ballast was also added to the inlet pump line.

3.7 Conclusions

Laboratory observations of the nitrate radical absorption spectrum validate the successful operation of the TAMU cavity ring-down spectrometer. Further verification for the detection of NO_3 is seen with the effective titration with NO to provide a baseline ring-down trace. This chemical zeroing technique allows for modulation of the NO_3 concentration without affecting other gases and therefore eliminates water interferences. Furthermore, the determination of the preconverter temperature of 80 to 100 °C demonstrates the complete conversion efficiency of N_2O_5 to NO_2 and the detected NO_3. These results provide evidence for the instrument preparation for field testing, which will be discussed in the subsequent section.

4. FIELD OBSERVATIONS

4.1 Introduction

This section describes nitrate radical and dinitrogen pentoxide observations measured with the CRDS instrument at ground-level at Lick Creek Park in College Station, Texas. These CRDS observations were made in conjunction with NO_2 and O_3 measurements *via* commercially available Thermo Fisher Scientific instruments. The main objective of this field test was not only to observe ambient mixing ratios of NO_3 and N_2O_5, but also to evaluate the performance of the CRDS instrument under field conditions. These measurements gave insight for further modifications and improvements to the instrument.

4.2 Site Motivation

Lick Creek Park, a local College Station park, is located northwest of Houston, Texas (30.569ºN, 96.216ºW) as shown in Google Map[68] image in Figure 4.1. The CRDS sampling point was located in the equestrian entrance of the park at ground-level in a trailer provided by the atmospheric department of Texas A & M University. Between the cities of Houston and College Station is natural, non-agricultural vegetation, inhabited mainly of post oak woodlands. Therefore, typical southerly winds allow for the study of Houston's urban air plumes into rural College Station.

Post oak trees are known isoprene emitters.[69] As discussed in section 1, the nitrate radical is a potent oxidizer and thus the major fate of many volatile organic compounds, such as isoprene, in the nighttime atmosphere. The oxidation of isoprene by

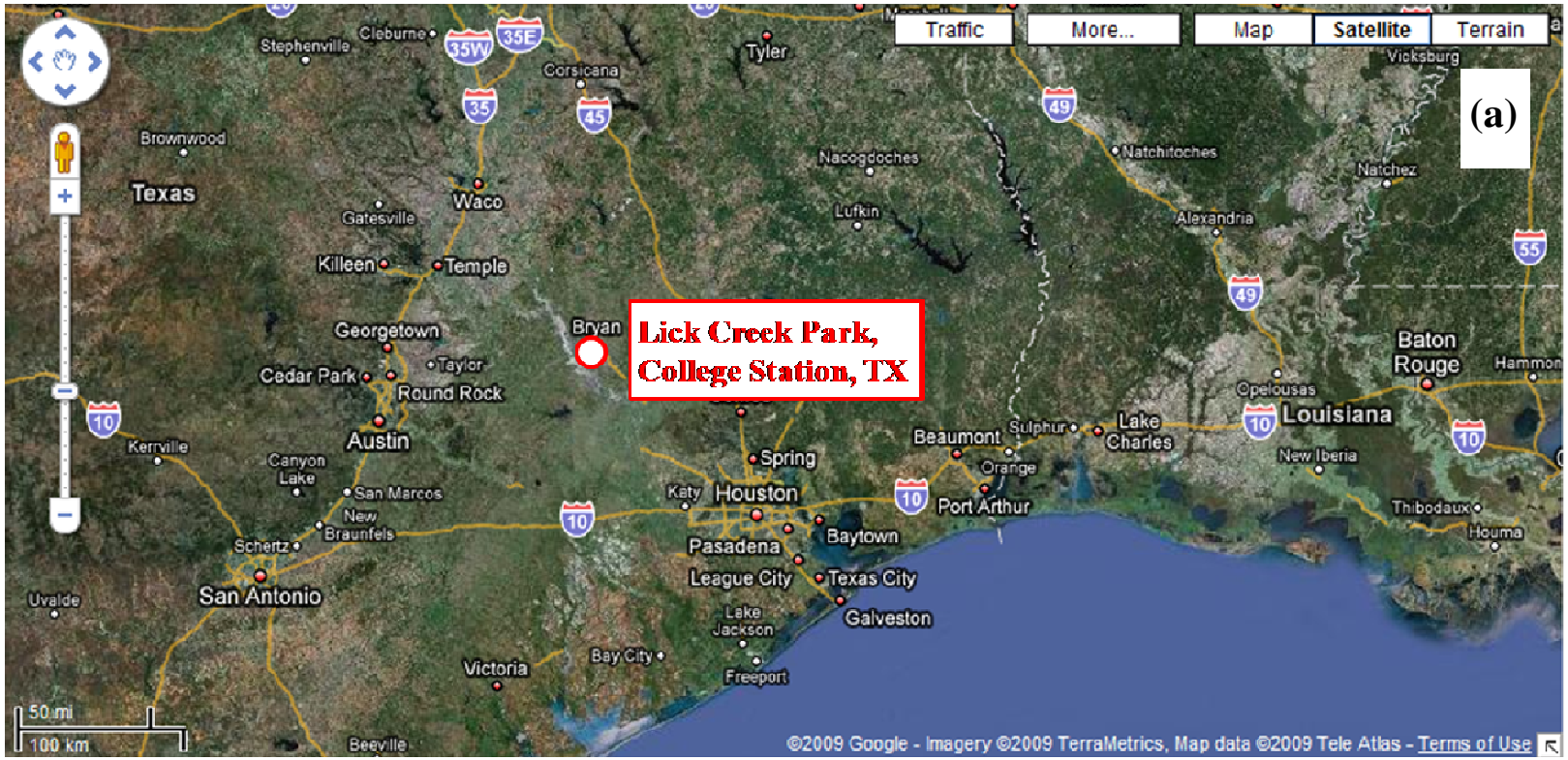

Figure 4.1. Google Map[68] images showing the location of the measurement site at Lick Creek Park in relation to Houston, Texas (a), and to College Station, Texas (b).

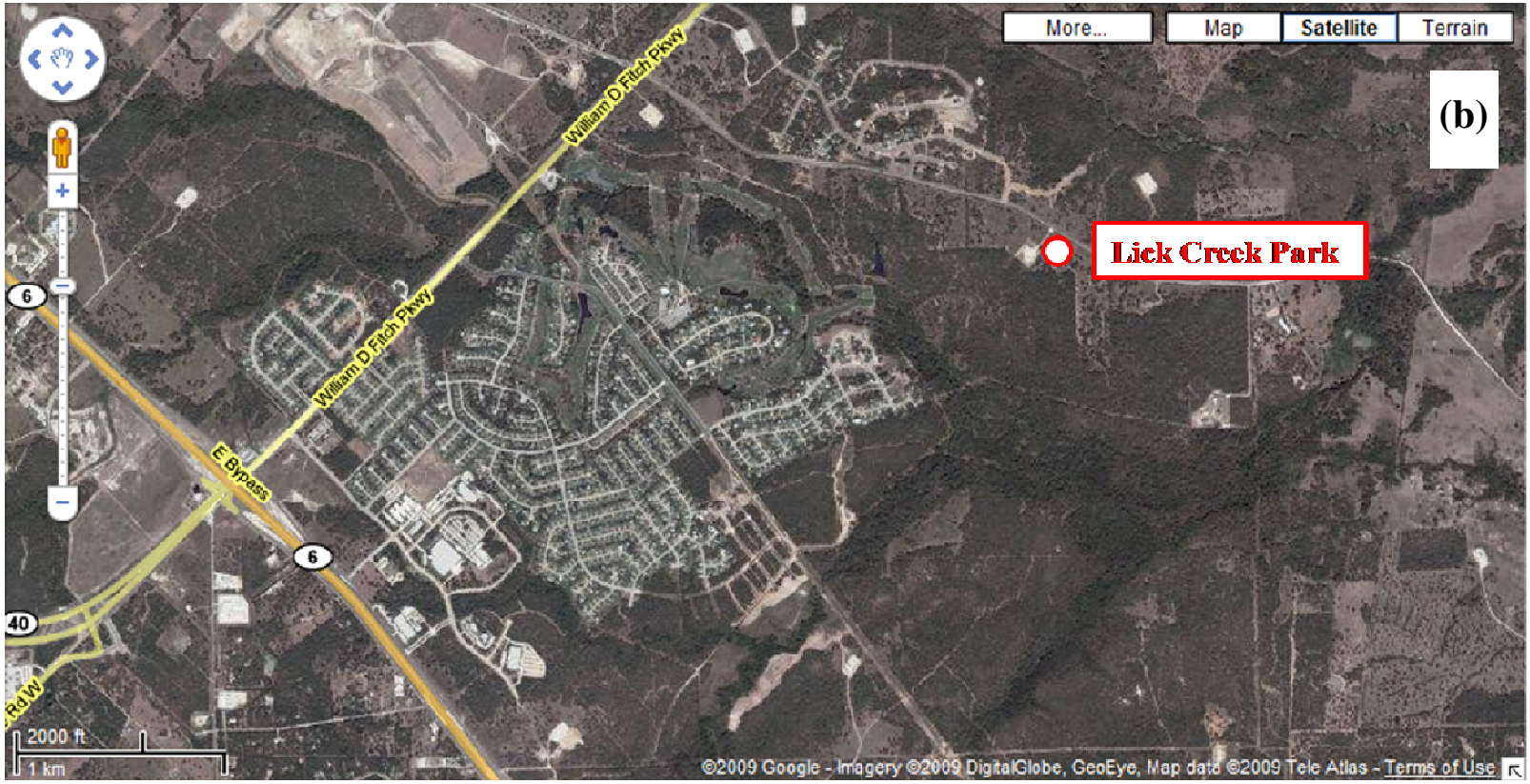

Figure 4.1. continued

reacting with NO_3 results in the formation of a nitrate radical by addition to one of the double bonds:

$$C_5H_8 + NO_3 \longrightarrow C_5H_8 - ONO_2$$

This nitrate radical can then further react with an oxygen molecule to give a nitroxy-peroxy radical.[70] Subsequent reactions provide a source for HO_2 radicals and in turn OH radicals. This reaction sequence is therefore an important sink for isoprene and other VOCs by providing a method for production of organic free radicals and OH at night, in the absence of photolytic sources and thus production of O_3.

4.3 Instrumentation

The trailer is shown in Figure 4.2, with the inlet ports raised approximately 3 m above the ground and facing southeast, while the exhaust lines were directed underneath the trailer facing northwest as to prevent re-sampling of the exhaust. Also pictured is the instrumentation setup inside the trailer.

In addition to the CRDS measurements of NO_3 and N_2O_5, simultaneous measurements of O_3 and NO_x were accomplished with the use of Thermo-Fischer Scientific Analyzers. The UV photometric ozone analyzer, model 49i, employs the absorption at 254 nm and calculates the ozone concentration *via* the Beer-Lambert Law

$$\frac{I}{I_0} = e^{-KLC}$$

where I is the UV light intensity with ozone present, I_0 is the UV light intensity without ozone present, K is the molecular absorption coefficient at 0 °C and 1 atm (=308 cm^{-1}),

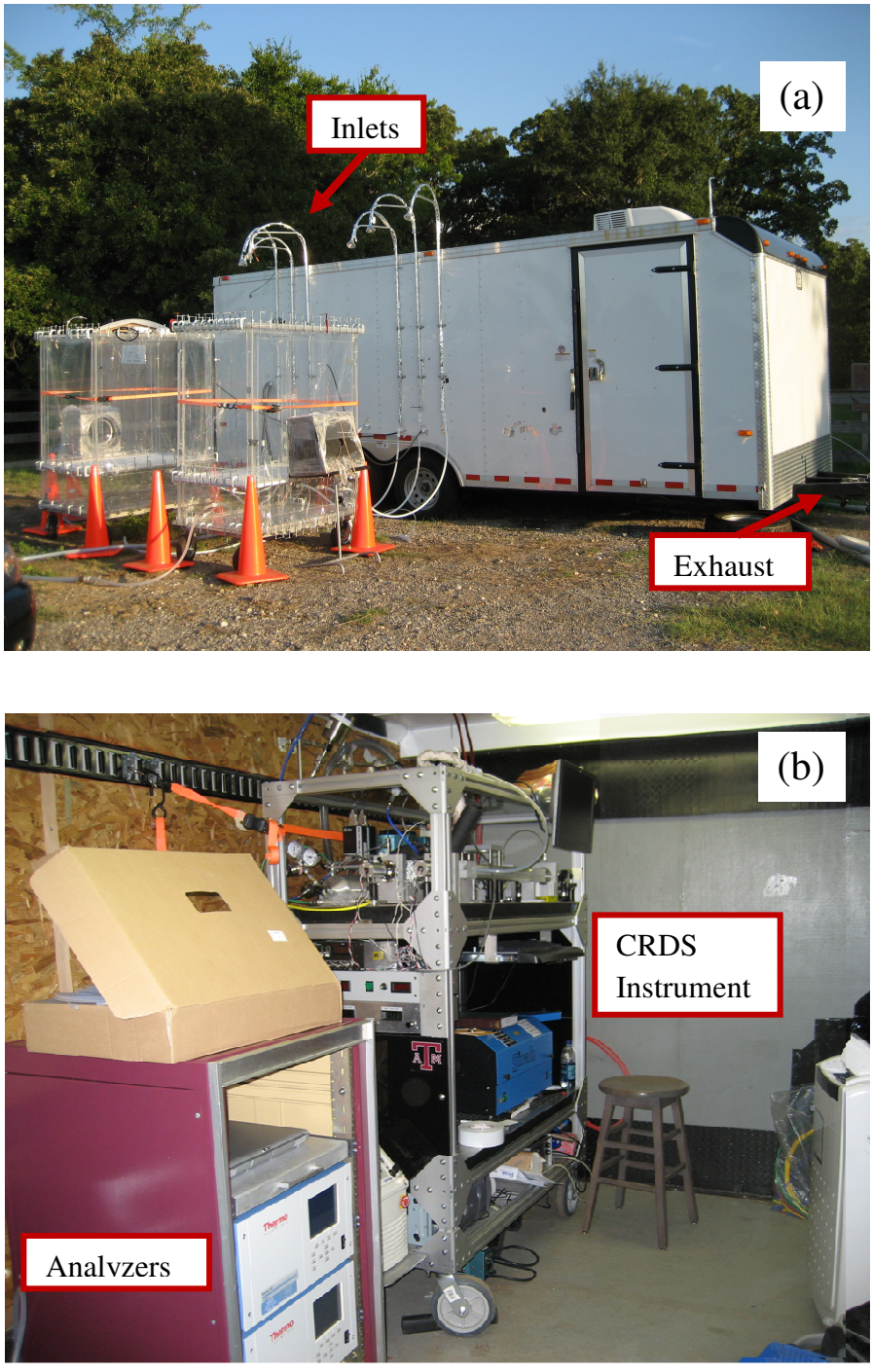

Figure 4.2. Instrumentation trailer for measurements at Lick Creek Park, College Station, TX. (a) Outside of the trailer with inlet and exhaust ports. (b) CRDS instrument and Thermo-Fisher Scientific analyzers inside the trailer.

L is the length of the cell at 38 cm, and C is the ozone concentration. The chemiluminescence NO-NO_2-NO_x analyzer, model 42i, utilizes the reaction

$$NO + O_3 \longrightarrow NO_2 + O_2$$

$$\longrightarrow NO_2 * + O_2 + hv$$

The luminescence intensity is linearly proportional to the NO concentration. NO_2 is first converted to NO by a molybdenum NO_2-to-NO converter heated to approximately 325 °C before being measured by the chemiluminescence reaction.

During the deployment at Lick Creek Park, the Thermo analyzers did not consistently record NO_x and ozone measurements. Both instruments would periodically shut down, which required restarting them. Therefore, measurements obtained from these instruments were sporadic and incomplete. The issue has since been corrected.

4.4 Results

During the one month period of September 2008, the TAMU CRDS instrument observed NO_3 and N_2O_5 during two nights, September 15-16 and 21-22, at Lick Creek Park. Only the results from September 21-22 will be discussed below because observations on the 15-16 were only for a small portion of the night.

Figure 4.3 shows the CRDS-N_2O_5 + NO_3 observed concentrations without any corrections for losses. The error bars correspond to the calculated sensitivity values from Equation 2.4. Ambient concentrations were observed starting at 11:20 pm on the night of September 21 and continued throughout the night and into the following morning. The last measurable concentration of N_2O_5 + NO_3 occurred at 4:40 am. Nighttime concentrations were shown to fluctuate around 30-40 ppt. NO_3 was detected

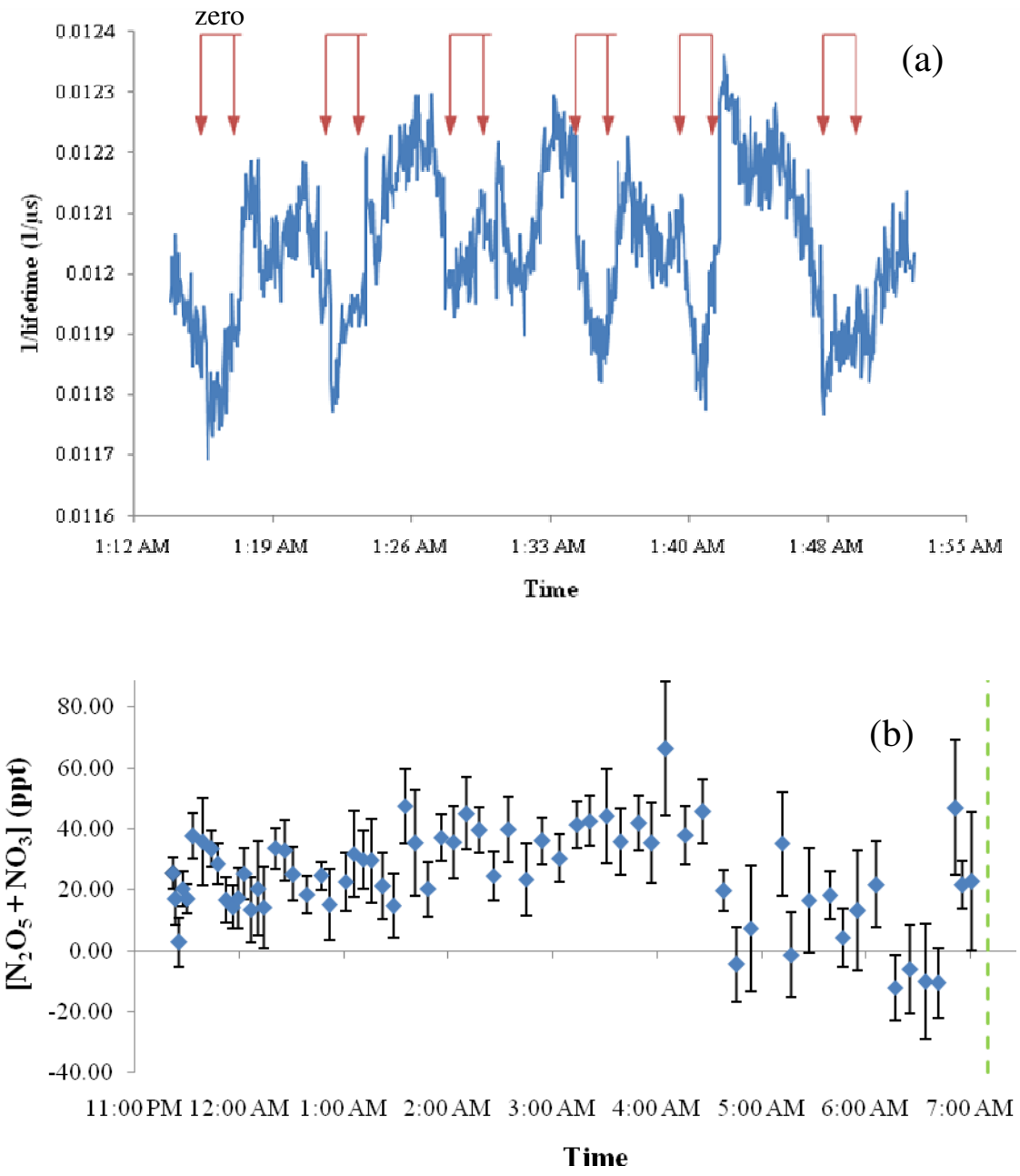

Figure 4.3. Lick Creek Park observations for September 21-22, 2008. (a) Portion of the observed 1/lifetime vs. time plot from the $N_2O_5 + NO_3$ cavity. The brackets indicate where zero measurements were taken by addition of NO. (b) The observed $N_2O_5 + NO_3$ without correcting for losses. Error bars correspond to calculated detection limits from Equation 2.4. Sunset is indicated with the dotted green line at 7:10 am central daylight savings time.

via the CRDS instrument, however, low concentrations did not allow for quantitative measurements to be made during this field study. Because of the rural area and the low concentrations of N_2O_5, steady-state mixing ratios of NO_3 were predicted to be at levels of only a few ppt. This was below the detection limit of the instrument at the time and will be discussed later.

NO addition occurred approximately every 3-5 minutes and an example is shown in Figure 4.3 for a portion of the night in the heated cavity. This zero measurement lasted on average about 1 minute and corresponds to the background ring-down measurements. The first 5 seconds of the zero measurement are discarded to allow NO to fill the inlet and completely deplete NO_3 in the system. The zeroed data is quantified by averaging the background data. Because flushing of the NO requires more time (*i.e.* NO diffusing out of the line), the first 15 seconds of the measurement cycle are discarded. A linear least square fit of 25 seconds on either side of the zeroed data is calculated. The best fit line equation is used to determine the measurement ring-down at the averaged zero time. The difference in the measurement ring-down and the background ring-down is used to quantify the $N_2O_5 + NO_3$ concentrations in the analysis cell *via* Equation 2.3.

The detection limit is highly affected by the drifts in the baseline between background measurements. When the background is subject to large and/or rapid changes, more frequent baseline measurements relative to signal are required. During the night of September 21st, significant background drifting was observed and appeared to worsen in the early morning hours of September 22nd. However, the frequency of

baseline measurements throughout the night did not change and thus with the increase in drifting at these times resulted in poor sensitivity values. Detection limits ranged from 4.5 ppt – 23 ppt, with an average of about 11 ppt, throughout the night of 21st – 22nd of September for the N_2O_5 + NO_3 and NO_3 measurements.

Possible sources for background drift are instability in the optical cavities, such as thermal alignment drift or pressure fluctuations, changes in background absorbers, changes in the density of fine aerosols that pass through the Teflon® membrane inlet filter, and/or extinction due to aerosol in the air sample. The observed temperature fluctuations of ± 2 °C and pressure changes of ± 3 Torr for the heated optical cavity could have possibly contributed to some baseline drifting, but cannot be the sole source of background instability. If the drifting was a result of temperature or pressure fluctuations in the heated cell, the ambient optical cavity would not have coincided with the heated cavity fluctuations as observed. Background absorbers, such as nitrogen dioxide and ozone, were measured simultaneously with the CRDS instrument to provide detection of dramatic changes in their concentrations. Unfortunately, the Thermo analyzers were not consistent in recording, especially for NO_x concentrations. The factory-calibrated analyzers were not recalibrated after shipment, which resulted in low, as well as negative, concentration measurements for NO_x and O_3. The ozone measurements for September 21-22, ranged between 0 and 10 ppb; however the ozone concentration fluctuations do not seem to correspond to the signal drifting in the CRDS instrument. It is possible that NO_2, water or aerosols caused the baseline drifting, but this cannot be determined.

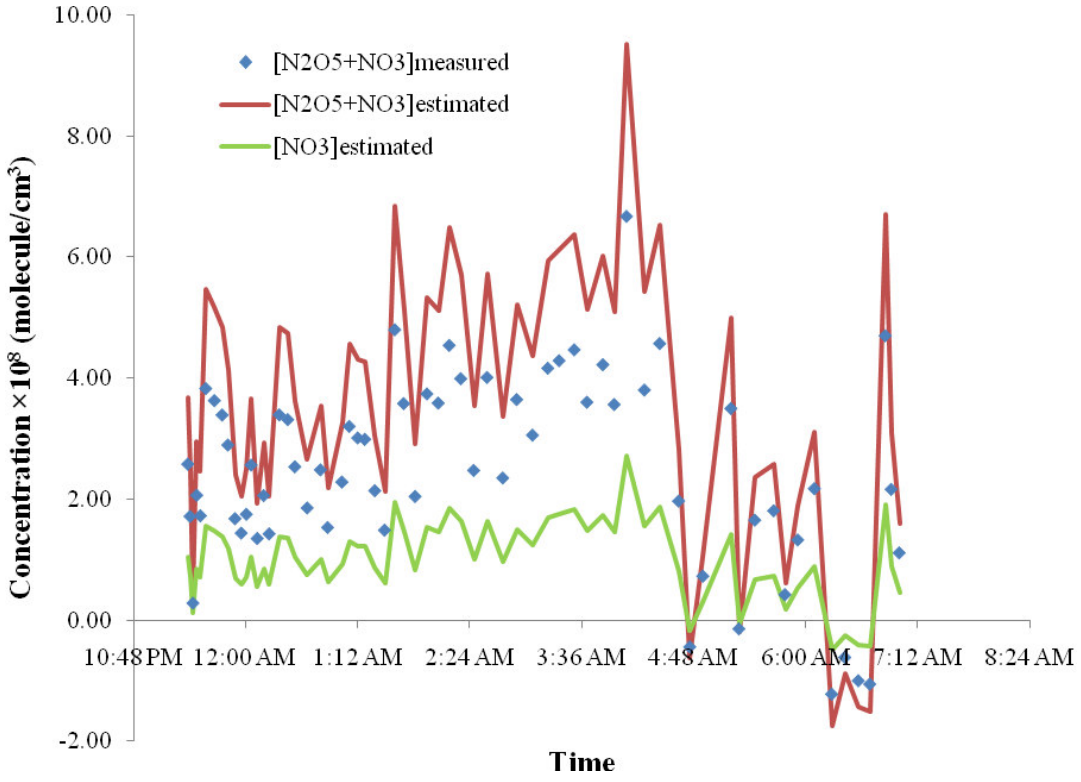

Figure 4.4. N_2O_5 and NO_3 measured and estimated concentrations for September 21-22, 2008. The points represent the measured [N_2O_5 + NO_3], while the lines correspond to the estimated [N_2O_5 + NO_3] and [NO_3] from the temperature dependent equilibrium expression and assuming a transmission efficiency of 70%.

The instrument was not fully calibrated prior to the deployment at Lick Creek Park. Therefore, total losses due to wall reactions, filter transmission, and thermal conversion efficiency of N_2O_5, could not be quantified. To approximate the concentration of NO_3, the transmission efficiency was assumed to be approximately 70%, based on similar CRDS designs.[50] The calculations utilized the temperature dependent equilibrium constant of 2.9×10^{-11} cm^3 molecule, at 760 Torr and 298 K. With an estimated concentration of 3.5 ppb of NO_2, the ratio of $[N_2O_5]/[NO_3]$ is 3.5. N_2O_5 concentrations along with NO_3 concentrations were calculated for the night of September 21-22, 2008, and are shown in Figure 4.4.

To determine the exact location from which the polluted air mass travelled, three-dimensional air mass trajectories were calculated using the National Oceanic and Atmospheric Administration (NOAA) Hybrid Single Particle Lagrangian Integrated Trajectory (HYSPLIT4) model with the 1° x 1° latitude-longitude grid, employing the Eta Data Assimilation System (EDAS) archived database.[71] The EDAS archived data is generated by the National Centers for Environmental Prediction (NCEP) and provides a 3-hour horizontal and 40 km vertical resolution. Basic information, such as u- and v-wind components, temperature, and humidity, are also provided in the archived database. Real-time Environmental Applications and Display sYstems (READY)[72] is internet-based and provides access to anyone to the HYSPLIT4 model to run trajectory and dispersion simulations.

The HYSPLIT4 model indicated that the air masses with the 3-day trajectories ending at an altitude of 5 meters at 12:00 AM central time for September 22, 2008

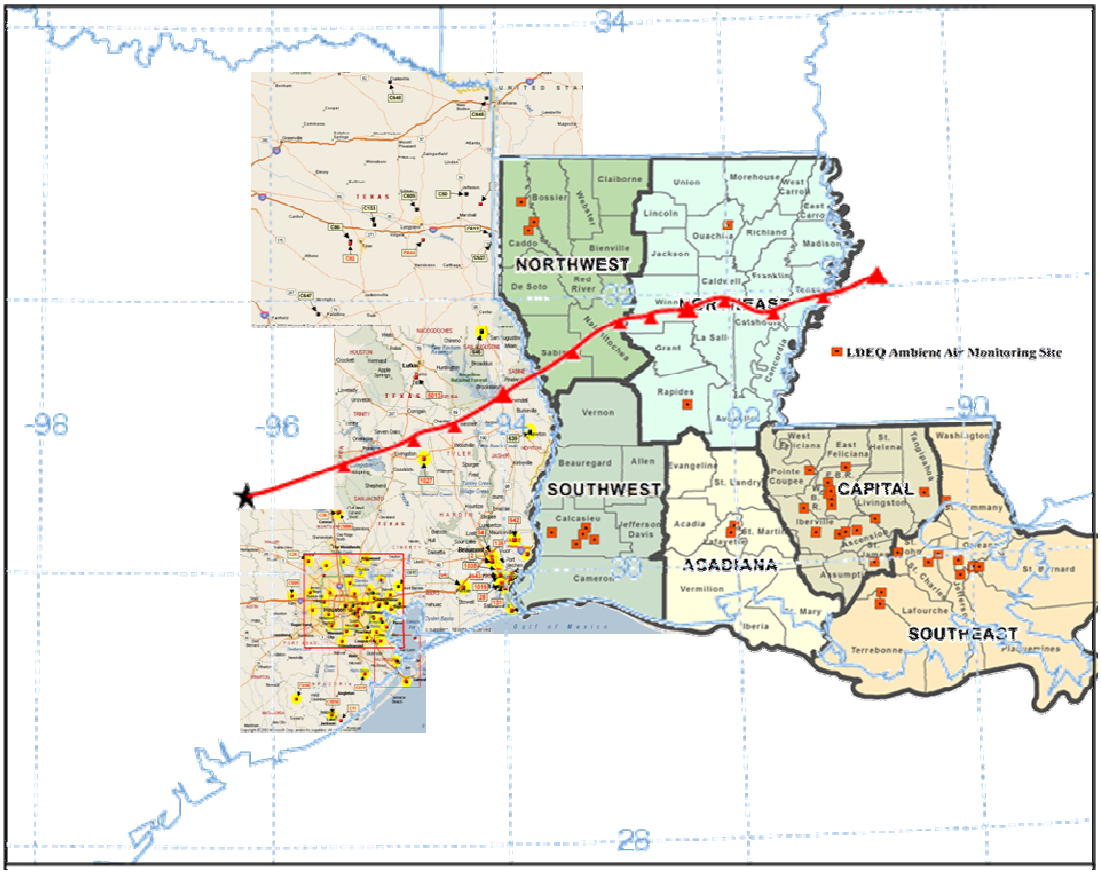

Figure 4.5. HYSPLIT4[71] back trajectory overlaid on a map displaying TCEQ[73] and LDEQ[74] monitoring sites.

originated from central Louisiana rather than over Houston, Texas. The unusual easterly winds, rather than the typical southerly winds, of Lick Creek Park can be attributed to Hurricane Ike. Landfall for Hurricane Ike was on September 13, 2008 in Galveston, Texas, while the storm surge travelled north to northeast through Texas and into Arkansas.

We investigated the possible explanation for the polluted air mass that travelled from the east into College Station, Texas. Accessing the Texas Commission on Environmental Quality (TCEQ) website,[73] as well as the Louisiana Department of Environmental Quality (LDEQ) website,[74] provided a determination of the active monitoring sites. These sites displayed in Figure 4.5 are represented with the HYSPLIT4 modeled back-trajectory for September 22, 2008. No monitoring sites in Louisiana were located within or near the trajectory path. One site in Texas, C1027, was located within a reasonable distance from the trajectory path. Within the timeframe of the Lick Creek Park measurements, this site was in the process of being deactivated. Therefore, ozone was the only monitored pollutant at the C1027 site and does not provide enough information for analysis. The possibility of the air mass resulting from coal plants in Texas was also researched. As with the case of the monitoring sites, the coal plants did not lie within or near the trajectory path for the Lick Creek Park air mass source. Even though the explanation of the polluted air mass could not be determined, it does not diminish the fact that N_2O_5 +NO_3 was observed.

4.5 Conclusions

Lick Creek field measurements provided considerable insight to the operation of our instrument and will also allow for future modifications to the instrument and sampling procedure. With the observation of highly variable background drifting during deployment, more frequent zeroing by titration with NO is therefore required to improve upon the detection limit. It was deemed necessary to reduce the noise in the instrument in order to detect ambient NO_3, which is typically in the range of sub-ppt to 20 ppt in concentration.

5. CURRENT AND FUTURE DIRECTIONS

5.1 Introduction

Prior to, and after, the successful deployment at Lick Creek Park, a considerable amount of effort was directed toward instrument modifications and determination of the loss of NO_3 and N_2O_5 to the sample inlet and filter. All alterations and measurements will aid in preparation for the future field campaign scheduled for April, 2009 in Houston, Texas. This section illustrates the further developments and calibration measurements that have led to an improvement in the accuracy of the instrument.

5.2 Current Modifications

Modifications for improvement of the CRDS instrument include replacement of the inlet tubing, addition of a solenoid valve in the NO titration line, and redesign of the filter mount. The fast-flow portion of the flow system is comprised of commercially available 25 ft of 1/4 in. OD, 1/16 in. ID PTFE Teflon® tubing. The remaining portion of the inlet and cells are constructed from FEP Teflon® tubing. PTFE is known to be slightly more reactive than FEP and can possibly lead to a greater loss of NO_3 and N_2O_5 prior to detection. Therefore, to also be consistent through the entire flow system, we replaced the PTFE tubing with FEP tubing of the same size.

Nitric oxide addition to the main flow line for titration of NO_3, as discussed in previous sections, presented problems with slow diffusion out of the line. Nitric oxide is added *via* a flow controller, located on the upper breadboard that houses the optical cavities. Therefore, it required a 36 in. long tube from the output of the flow controller

to the branch point at the sample inlet. At the completion of a baseline measurement, the NO flow controller is turned off. The remaining nitric oxide in the line therefore slowly diffuses out into the sample inlet, which affects the observed NO_3 concentration. In the laboratory, this diffusion time was quite variable and ranged from seconds to several minutes. To shorten this diffusion time, we added a nitrogen purge through the flow controller and thus the NO addition line. The purge was branched off of the dry nitrogen line for the CRDS mirror purging. This seemed to shorten the diffusion time, but not dramatically. While at Lick Creek Park, nitrogen purging of the NO line made no observable change in this diffusion time.

Addition of a PTFE solenoid valve (Parker Hannifin, 002-0017-900) into the NO titration line as close to the sample inlet branch point as possible, provided an observed reduction in the diffusion time. The solenoid valve, controlled *via* the Labview program, allowed for the testing of different timing scenarios for the opening and closing of the valve. A 30 second "on" time corresponds to the baseline measurement, with a 90 second "off" time equivalent to the measurement period. This timing sequence provided the shortest diffusion time of NO out of the line, while allowing the data measurement to stabilize before another baseline measurement. The calculated diffusion time for this 30 second on, 90 second off time, is approximately 7 seconds. It is also noted that this diffusion time is repeatable and not erratic as observed prior to the solenoid valve addition.

Another modification to the instrument includes a redesign of the filter mount. An automated filter changer, designed by Bill Dubé,[50] was constructed and mounted on

the top level of the instrumentation cart. The previous PTFE Teflon compression-fitted filter mount required a redesign for a few reasons. First, it entailed the user to dismantle the inlet line to replace the used filter with a new one. This was tedious and time consuming. In addition, the new design is comprised of PFA Teflon, which is less reactive in comparison to the PTFE Teflon utilized in the previous mount. The change in material may decrease the amount of NO_3 lost to wall reactions.

The filter changer, as seen in Figure 5.1, employs two PFA pistons that form an o-ring seal on either side of the Teflon membrane filter while air is flowing through the inlet. A filter change occurs when the flows to the inlet pump and cells are first turned off. The seal from the pistons onto the filter is broken once a vacuum to the back side of the pistons is applied and the pistons are withdrawn. The vacuum is held constant on the pistons until the filter is replaced. A change of filters occurs when the stepper motor (MicroMo, AM 1524) moves a rotating disk that holds the membrane filters. A new filter from a stack contained in the fresh filter reservoir falls into the rotating disk and is moved until it is placed in-line with the pistons. Simultaneously, the used filter is transported to a used filter reservoir. To confirm correct positioning of the new filter, a disk position sensor is utilized. An EZ BEAM, emitter and receiver (Banner Engineering, S186E and S18SN6R), is positioned on either side of the rotating filter disk. A slit in the disk allows the beam from the emitter through to the receiver to verify the correct placement of the filter. Once aligned, the pistons are then moved back into position and a seal is formed against the filter when compressed air is applied to the back sides of the pistons. The cell and inlet pumps are turned back on and data

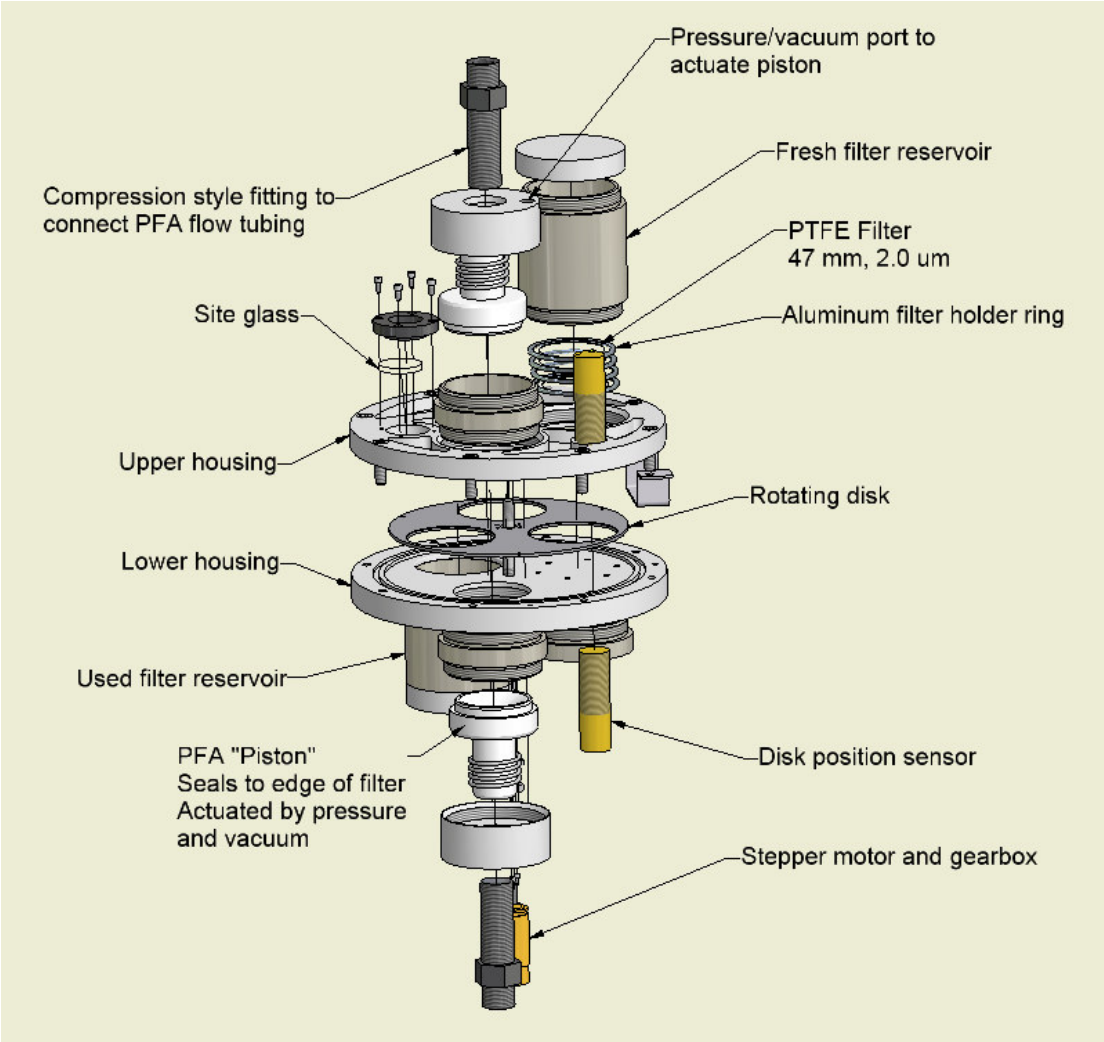

Figure 5.1. Schematic of the sealed, automated filter changer.

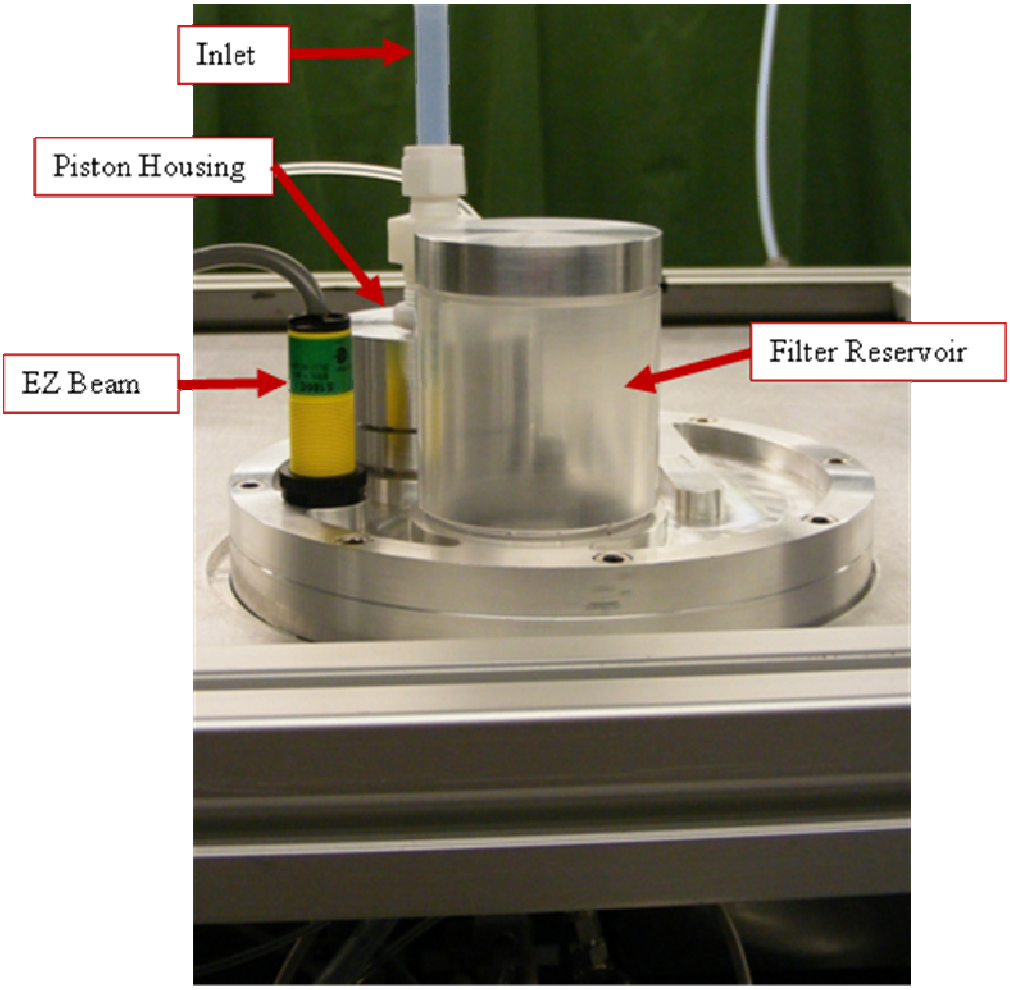

Figure 5.2. Filter changer mounted atop the instrument cart.

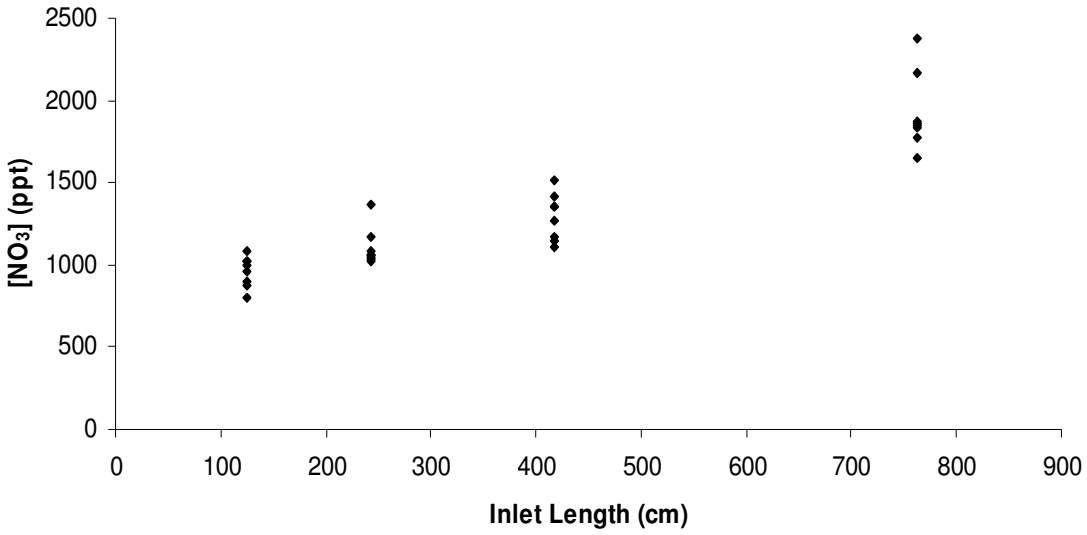

Figure 5.3. Observed $[N_2O_5]$ versus inlet length.

acquisitioning can commence. The pistons are held in place with the compressed air until it is time for another filter change. This prevents contamination into the inlet from room air. An image of the filter changer mounted onto the instrument cart is seen in Figure 5.2.

5.3 Laboratory Measurements

Due to the reactive nature of the nitrate radical, it is highly important to determine losses on surfaces throughout the system to perform accurate measurements of NO_3 and N_2O_5 concentrations *via* the *in situ* technique of CRDS. To ascertain these losses of NO_3 and to a lesser extent N_2O_5, observation of the nitrate radical concentration with different inlet lengths can provide absolute losses through the FEP tubing. This can be performed with a synthesized sample of N_2O_5 at a fixed concentration. Utilizing the setup resembled in Figure 3.3 shown previously, N_2O_5 losses can be determined by changing the inlet length between the sample bubbler and the tee-connection to the inlet pump. Similarly, NO_3 losses can be accomplished with different inlet lengths; however, it is necessary to decompose the N_2O_5 sample to NO_3 and NO_2 immediately after the sample bubbler prior to entering the inlet tubing. Figure 5.3 displays the results from the measurement of N_2O_5 losses with different inlet lengths, showing an inverse correlation between inlet length and wall loss. These results are inaccurate because losses from wall collisions should increase with inlet length. Instability in N_2O_5 concentrations may be to blame for this erroneous measurement. NO_3 losses have yet to be performed.

Further lab calibration testing is scheduled to determine filter transmission of NO_3 and N_2O_5, as well as repeating inlet length losses. In addition to repeating the wall

loss measurements, we will be repeating the thermal conversion efficiency measurements. These calibration measurements will be performed simultaneously with an ion-drift chemical ionization mass spectrometer (ID-CIMS) instrument provided by Dr. Zhang in the TAMU atmospheric department. To accurately determine the concentration of N_2O_5 flowing into the system, a UV-Vis spectrometer will be implemented.

5.4 SHARP/SOOT Field Campaign

The Houston/Galveston/Brazoria area has a large urban population where the largest petrochemical complex in the world resides. With the combination of motor vehicle emissions and VOC emissions from petrochemical plants, ozone concentrations are a major concern for the Houston area.

In 2006, the TexAQS-II (Texas Air Quality Study-II) and Tramp (TexAQS-II Radical and Aerosol Measurement Project) campaigns discovered that further understanding of radical processes in the Houston atmosphere were required for accurate atmospheric modeling. Therefore, the development of the Study of Houston Atmospheric Radical Precursors (SHARP) project was undertaken. A list of researchers participating in the project and the target species measured is compiled in Table 5.1. The goals of the project are to determine direct emissions from point sources of OH radical precursors, HCHO and HONO, to deduce possible sources of HONO during the day, to study the possible pathways of surface-induced formation of HONO, to determine ambient levels of $ClNO_2$ and its role as a source of chlorine radicals, and to decipher gaps from missing radical sources in atmospheric modeling. Measurements

Table 5.1. Investigators and the measurement targets during the SHARP campaign

Group	Investigators	Measurement Target
Aerodyne,	Scott Herdon	HONO
Harvard University,	Ezra Wood	Aerosol mass
Montana State University, and	Berk Knighton	Aerosol chemical composition
Molina Center	Tim Onasch	CO
	Ben Lee	CO_2
	John Hayne	O_3
	Bill Munger	NO
	Ed Fortne	NO_2
	Sally Ng	HCHO
	Miguel Zavala	HCOOH
		C_2H_4
		1,3-butadiene
		Particle number
		Black carbon
Georgia Institute of Technology	Greg Huey	$ClNO_2$
	Robert Stickel	N_2O_5
		PANs
National Oceanic and Atmospheric Administration	Winston Luke	NO
	Paul Kelley	NO_2
	Steve Brooks	NO_y
		SO_2
		Hg speciation
Pacific Northwest National Laboratory	James Cowin	Particle hygroscopicity,
	Martin Iedema	morpohology, and composition
	Xiao-Ying Yu	Organic and elemental carbon
		Particle number and concentration distribution
		Actinic flux and photolysis frequencies of NO_2/NO_3
Pennsylvania State University	Bill Brune	OH
	Xinrong Ren	HO_2
	Diana van Duin	PAM
	Maria Cazorla	ozone production
	Shelley Guare	
Rice University	Rob Giffin	Aerosol size and chemical
	Kabin Shakya	composition
	Sev Travis	
Texas A&M University	Simon North	NO_3
	Katie Perkins	N_2O_5
	Justine Geidosch	HONO
	Renyi Zhang	Aerosol
	Jun Zheng	
	Don Collins	
	Crystal Reed	
University of California - Los Angeles	Jochen Stutz	O_3
	Olga Pikelnava	NO_2
	Catalina Tsai	SO_2
	Deiian Fu	HONO
	Clare Wong	HCHO
	Jennie Thomas	NO_3

Table 5.1 continued

Group	Investigators	Measurement Target
University of Colorado	Michael Cubision	Aerosol size and chemical composition
	Amber Ortega	Particle number distribution
	Jose-Luis Jimenez	
University of Houston	Barry Leffer	O_3
	Bernhard Rappenglück	CO
	Gary Morris	NO
	James Flynn	NO_2
	Christine Haman	NO_y
	Marc Taylor	SO_2
	Nicole Grossberg	VOCs
	Richard Fuller	PANs
	Denet Pernia	HCHO
	Matt Haworth	HONO
	Barbara Schmeitz	HOOH
	Darrell Anderson	Temperature
	Julia Golovko	Pressure
	Leonardo Pedemonte	Relative humidity
	Sergio Alvarez	Wind speed
	Luis Ackermann	Wind direction
	Cari-Sue Wilmot	Precipitation
		Actinic flux
		Boundary layer height
University of L'Aquila	Piero Di Carlo	NO_2
	Franco Giammaria	HNO_3
	Cesare Dari-Salisburgo	Total peroxy nitrate
	Eleonora Aruffo	Total alkyl nitrate
University of Miami	Xinrong Ren	HONO
	Elliot Atlas	HNO_3
University of New Hampshire	Jack Dibb	HNO_3
	Eric Scheuer	HONO
	Chelsea Corr	HCl
	Luke Ziemba	
	Meridith Clevland	
University of Texas - Arlington	Purnendu K. Dasqupta	Nitrophenols
	Santosh Mishra	
	Abul Kalam Azad	
	Lucksagoon Ganranoo	
Washington State University	George Mount	HCHO
	Elena Spinei	Wind velocities
	Tom Jobson	Speciated OVOCs
	Matt Erickson	
	Will Wallace	
	Jacob McCoskey	
Valparaiso University	Gary Morris	O_3
		SO_2
		Pressure
		Temperature
		Relative humidity
		Wind speed
		Wind direction

occured in the late spring, when Houston typically exceeds the EPA standards for ozone, with an eight-hour ozone average greater than 75 ppb.[75]

To coincide with the SHARP campaign, Texas A&M University proposed the Surface-Induced Oxidation of Organics in the Troposphere (SOOT) project, which is one of many sub-projects of SHARP. The goal of this project is to assess heterogeneous chemistry involving radicals, oxidation of VOCs, and ozone formation during the day, as well as at night. The researchers involved are Dr. Renyi Zhang, Dr. Don Collins, and Dr. Simon North. Observations of HONO, HNO_3, HNO_4, N_2O_5, NO_3, and aerosols were conducted, with the addition of NO, NO_2, NO_y, speciated PANs, O_3, CO, SO_2, HCHO, HOOH, speciated VOCs, photolysis frequencies, aerosol optical depth, sky cam, and basic meteorological data provided by the University of Houston in accordance to the SHARP campaign.

The SOOT project proceeded alongside the SHARP project from April 15 to May 31, 2009 in Houston, Texas, atop the rooftop of Moody Tower at the University of Houston, depicted in Figure 5.4, which is 5 km from downtown Houston. Moody Tower is 18 stories tall, 70 m above ground level, which should be adequate for measuring NO_3 and N_2O_5. The Moody Towers site has no surface emission impacts and also allows for the observation of various air masses depending on the wind direction. The air masses of interest included downtown and the Houston ship channel. Moody Tower in relation to downtown and the ship channel is displayed in Figure 5.5.

As discussed previously, NO_3 is the dominant nighttime free radical and reacts with VOCs to produce peroxy radicals. These peroxy radicals serve as OH sources for

Figure 5.4. Moody Tower at the University of Houston – site for rooftop field measurements April 15 – May 31, 2009.

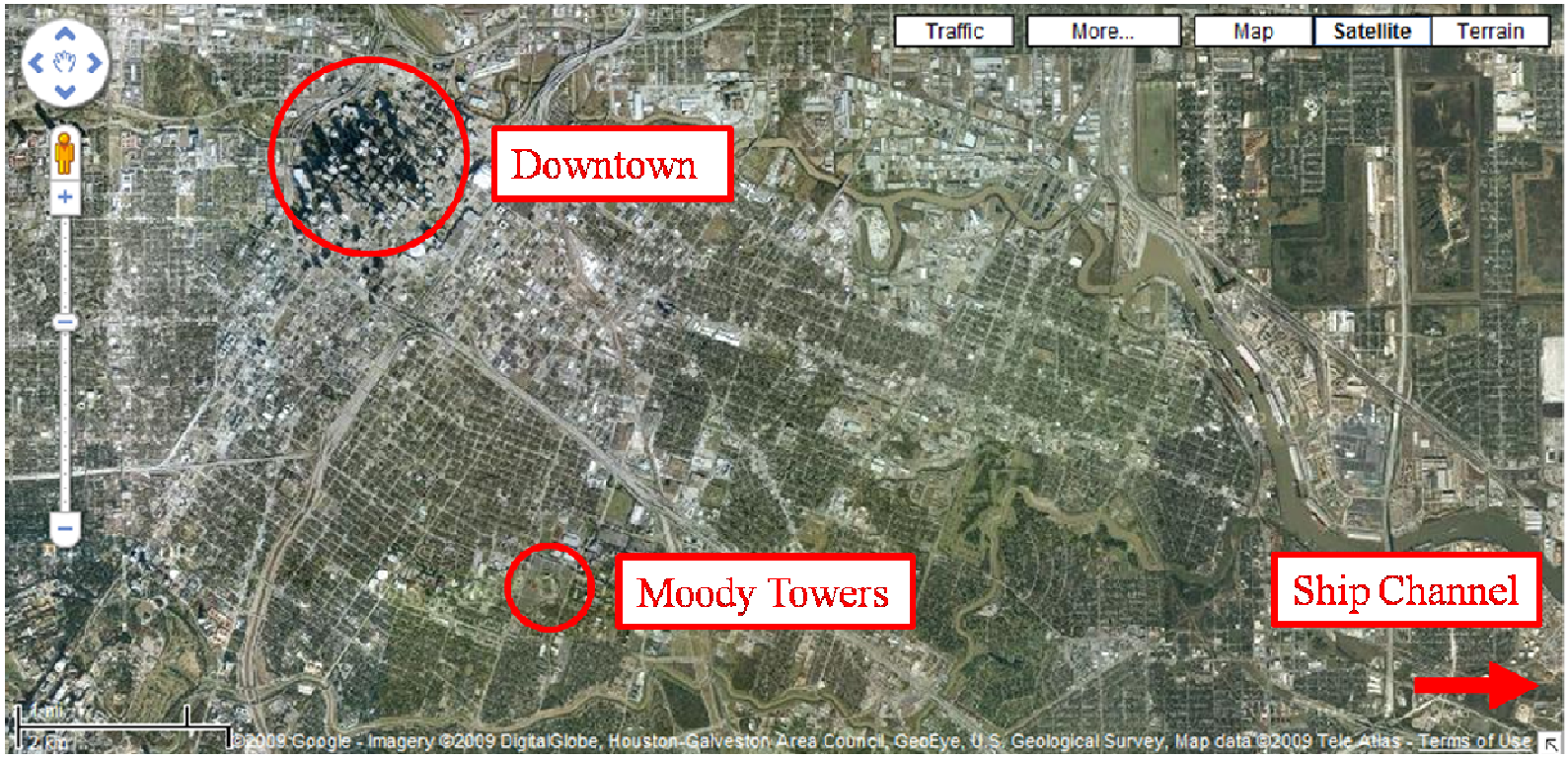

Figure 5.5. Google Map[68] of Houston, TX. Moody Towers, measurement site location in relation to downtown and the Houston Ship Channel.

the subsequent day to promote production of ground-level ozone. N_2O_5, as well as NO_3, also play an important role for removal of NO_x at night. N_2O_5 is readily removed *via* surface-induced heterogeneous reactions in the troposphere. The detailed mechanism for these heterogeneous processes is not well understood since the uptake coefficient of N_2O_5 on particles is highly variable.[76] The uptake coefficient for soot is approximately 0.005,[77] while for organic for organic particles or particles coated with organic material it is around 0.001 and below.[78, 79] The SOOT measurements aim to decipher the details of the heterogeneous processes. In addition to the surface-induced heterogeneous reactions involving N_2O_5, heterogeneous conversion of NO_x on soot particles is hypothesized to form nitrous acid (HONO). HONO concentrations would therefore increase during the night and then quickly photolyze in the early morning hours of the subsequent day to produce OH radicals. A detailed understanding of these heterogeneous processes can provide insight to the complexity of atmospheric nitrogen chemistry. In addition, the SHARP/SOOT campaign has the ability to aid in the reevaluation of the Houston SIP (State Implementation Plan) model for ozone and radical productivity.

Some preliminary data and discussion from the SHARP/SOOT campaign will be provided below. Note that the information provided is not in final form and presents approximate concentrations for the species measured. Figure 5.6 is a schematic for the location of the measurement trailers on the roof of Moody Tower. The TAMU CRDS inlet faces southeast towards the Houston Ship Channel and an image of the inlet port raised approximately 3 m above the rooftop is seen in Figure 5.7. Also pictuerd is the

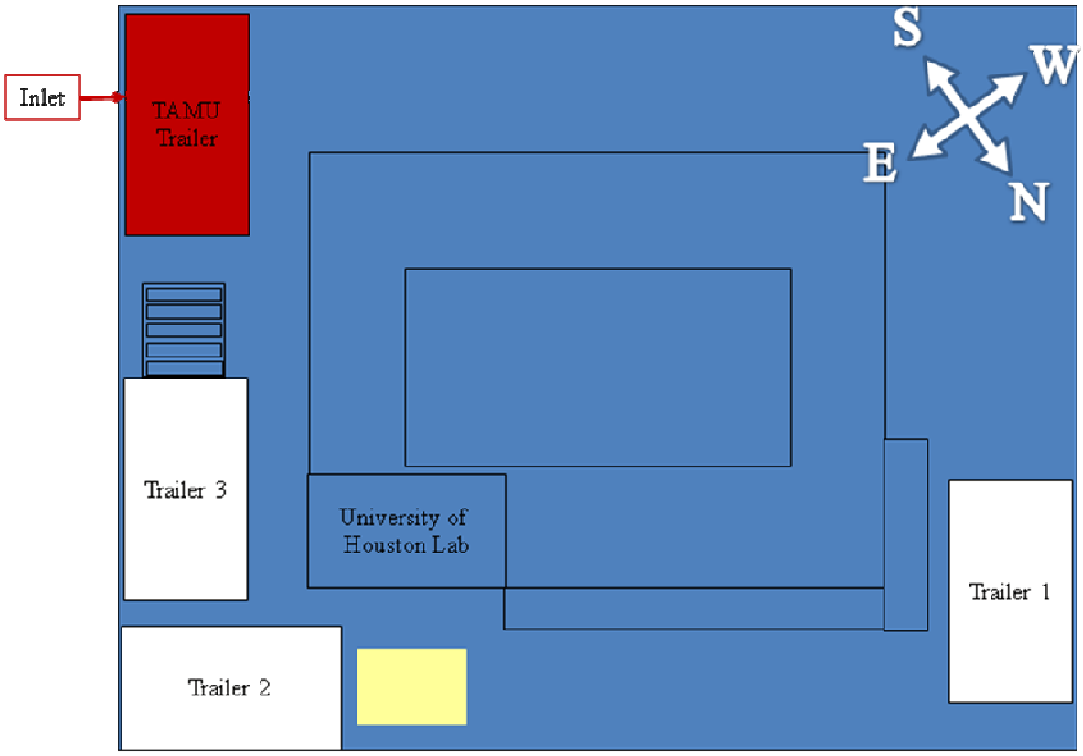

Figure 5.6. Schematic of the Moody Tower rooftop layout. In red is the TAMU trailer where the CRDS instrument was housed. The inlet location is also indicated.

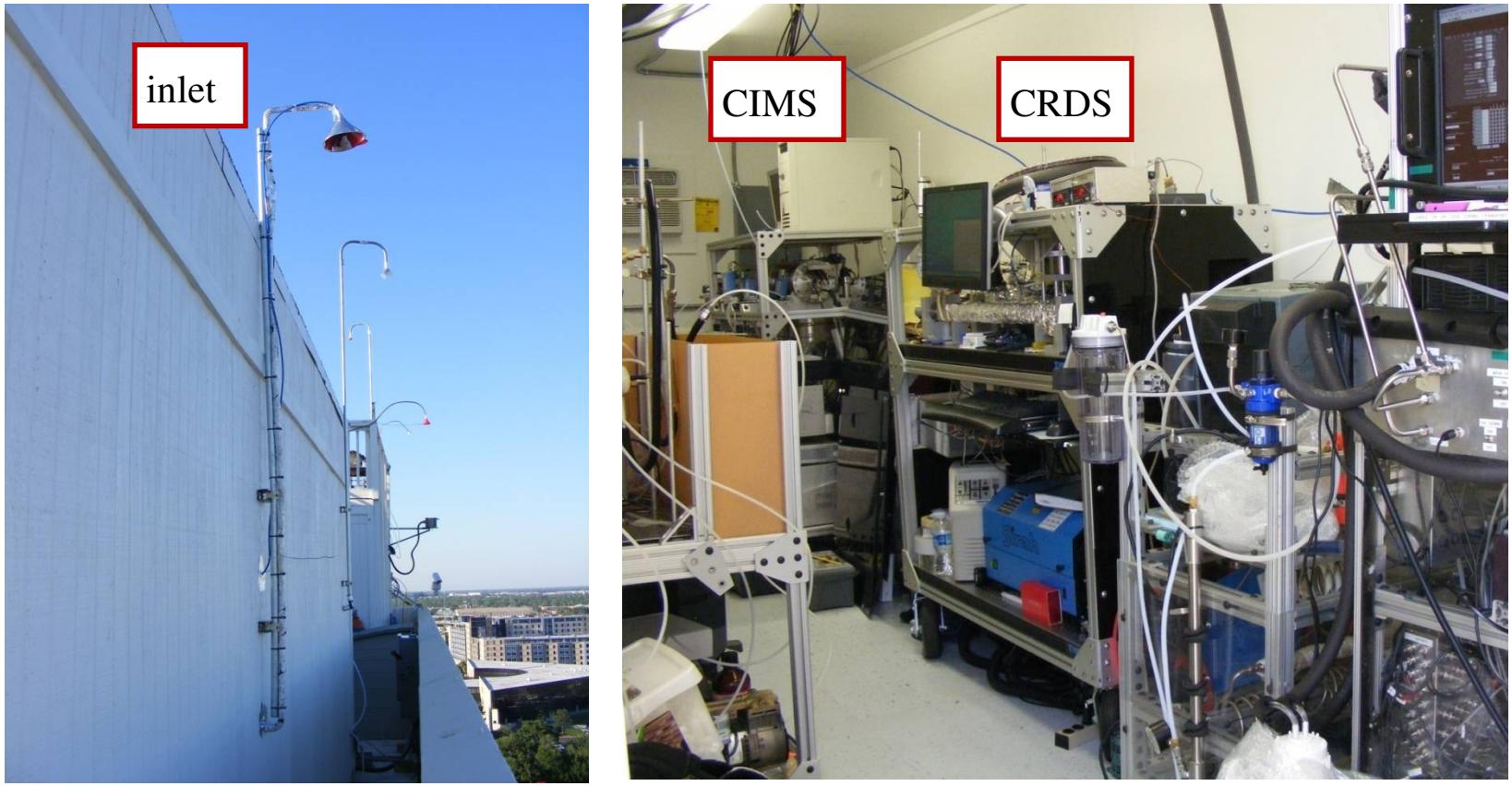

Figure 5.7. Instrumentation trailer for measurements at Moody Tower, Houston, TX. (a) Outside of the trailer with inlet mounted on the wall. (b) CRDS instrument and other TAMU instruments inside the trailer.

instrumentation setup inside the measurement trailer with the other instruments from Texas A&M University.

During the month and a half period of April 15 to May 31, 2009, the TAMU CRDS instrument observed NO_3 and N_2O_5 during ten nights at the University of Houston's Moody Towers. For the majority of the campaign, air quality in Houston was rather clean, with ozone concentrations reaching 40 ppb or less during the daytime hours. This resulted in ozone concentrations around 20 ppb or less at night, which in turn resulted in no observable NO_3 or N_2O_5. This is consistent with what is to be expected with low ozone concentrations, because the reaction of NO_2 and O_3 to form NO_3 is competing with the reaction of NO and O_3 to form NO_2. Only results from May 29-30 will be discussed in detail below since it was the evening with the maximum observed N_2O_5 concentration during the campaign.

Because the PTFE solenoid valve for the NO titration line had been installed prior to this campaign, the NO addition occurred at regular intervals, with an "on" time of 30 s and an "off" time of 90 s. A portion of raw data from the night of May 29-30, 2009 is displayed in Figure 5.8 to demonstrate the titration with NO to obtain a background ring-down lifetime. The first 5 seconds of zero measurement are discarded to allow NO to fill the inlet and completely deplete any NO_3 in the system. Because flushing the NO out of the line requires more time, the first 15 seconds, *i.e.* first 3 points, of the measurement cycle are discarded. The measurement ring-downs are quantified by calculating their average. The zeroed data on either side of the measurement ring-downs is used to calculate a linear least square fit of the background data. The best fit

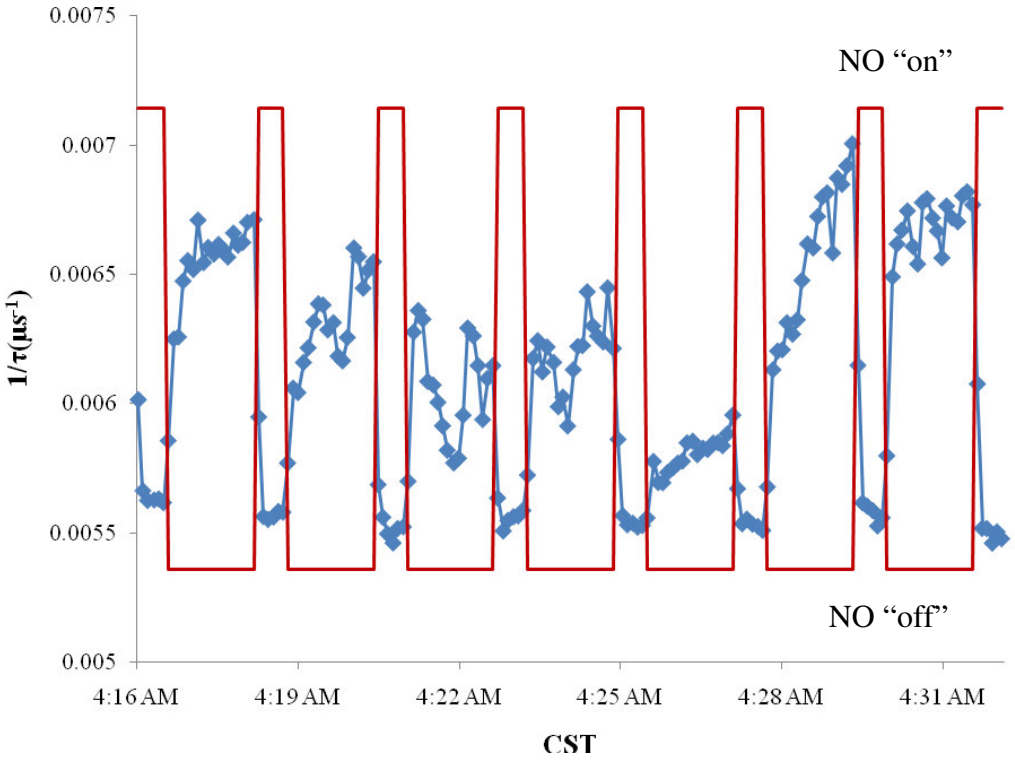

Figure 5.8. Portion of the observed 1/lifetime vs. time plot for May 29-30, 2009 from the $N_2O_5 + NO_3$ cavity. The red line indicates the NO solenoid valve "on" and "off" times for zero measurements.

line equation is used to determine the background ring-down at the averaged measurement time. The difference in the measurement ring-down and the background ring-down is used to quantify the $N_2O_5 + NO_3$ concentrations in the analysis cell *via* Equation 2.3.

Figure 5.9 shows the CRDS-$N_2O_5 + NO_3$ observed concentrations without any corrections for losses. The error bars correspond to the calculated sensitivity values from Equation 2.4. Observed detection limits for the night of May 29-30, 2009, ranged from 3 ppt – 20 ppt, with an average of approximately 8.5 ppt. Ambient concentrations were observed immediately and continued throughout the night and into the following morning. Nighttime concentrations were shown to increase into the morning hours, where the maximum $N_2O_5 + NO_3$ concentration of 295 ppt was observed at 4:30 am. Also plotted alongside the $N_2O_5 + NO_3$ data is the preliminary O_3, NO, NO_2, wind direction, and HONO measurements on the night of May 29-30, 2009. Zhang and Zheng[80] from Texas A & M University graciously provided the preliminary HONO measurements, while the University of Houston's B. Lefer and coworkers[81] were generous enough to provide the remaining preliminary measurements. These measurements are rough calculations and will only be used as approximate concentrations for comparison with the $N_2O_5 + NO_3$ data at this time.

For May 29, 2009, ozone concentrations reached a maximum of 127 ppb during the day, resulting in high concentrations around 60 ppb for most of the night. N_2O_5 concentrations gradually increased throughout the night. An expected correlation between O_3 and N_2O_5 was observed, with an inverse correlation between NO and these

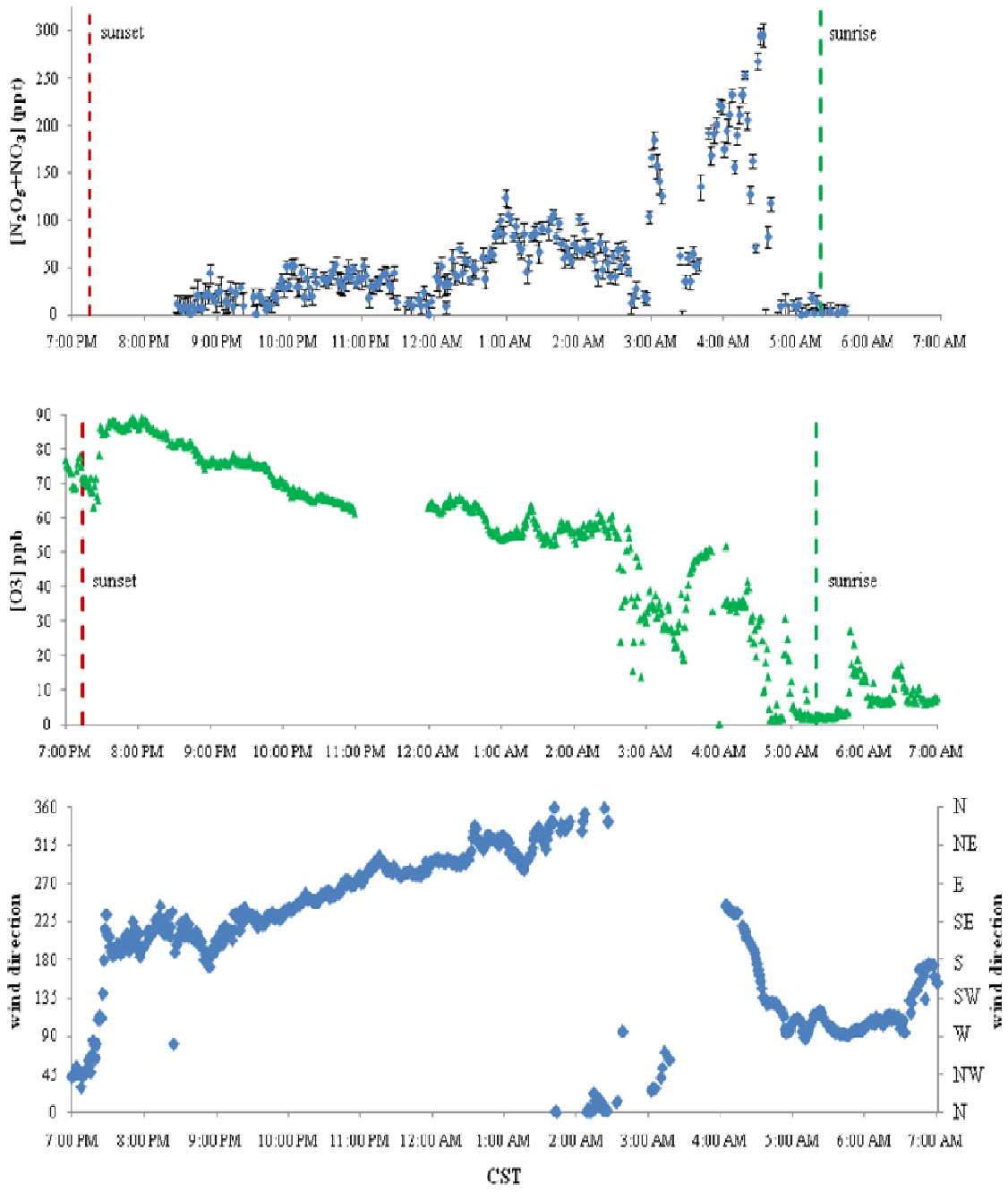

Figure 5.9. Moody Tower observations for May 29-30, 2009. Observed N_2O_5 + NO_3 without correcting for losses, ozone, wind direction, NO, NO_2 from B. Lefer *et al.*[81] and HONO measurements from Zhang and Zheng.[80]

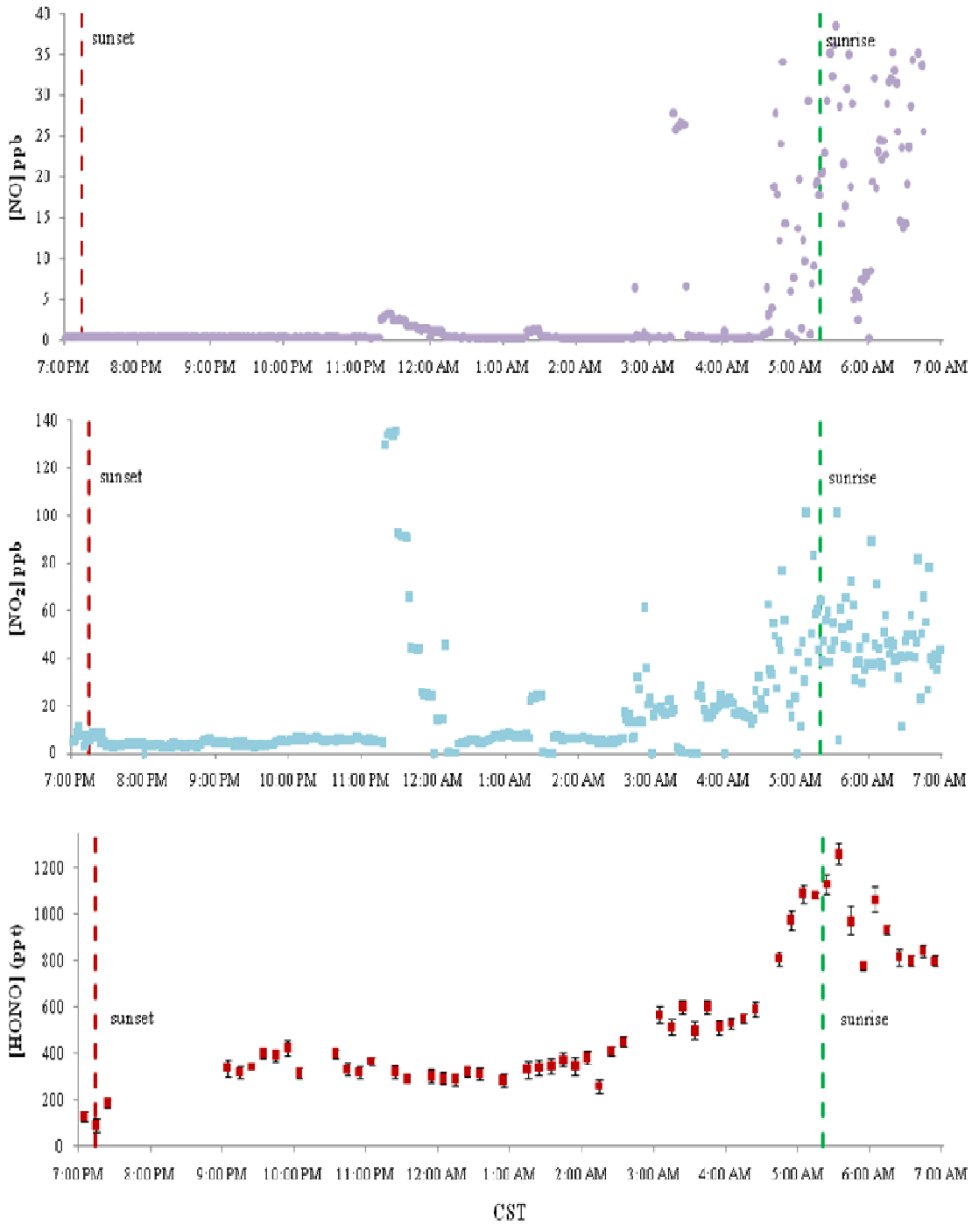

Figure 5.9. continued.

two species. Between 2:00 and 3:00 am a shift in the wind direction from north/northeast (downtown) to northwest caused a drop in the observed N_2O_5 and O_3. The Southeasterly wind shift from the Ship Channel then resulted in an increase in ozone and N_2O_5 concentrations. Once the wind direction changed again to a westerly breeze, a NO/NO_2 plume was measured and caused a drop in concentration for the O_3 and N_2O_5 species prior to sunrise. Also observed is the increase in the HONO concentration measurements throughout the night, coinciding with the N_2O_5 concentrations.

Similar to Lick Creek Park measurements, the instrument was not fully calibrated prior to the deployment at the University of Houston's Moody Tower. Total losses from wall reactions and filter transmission cannot be quantified at this time. NO_3 was detected *via* the CRDS instrument; however, quantitative measurements were not attained during this field study due to the detection limit of the instrument. To approximate the concentration of NO_3, the transmission efficiency was assumed to be approximately 70%, based on similar CRDS designs.[50] The calculations utilized the temperature dependent equilibrium constant of 2.9×10^{-11} cm^3 molecule, at 760 Torr and 298 K. With an estimated concentration from measurements by the University of Houston for NO_2, the concentrations for N_2O_5 and NO_3 were calculated for the night of May 29-30, 2009, and are shown in Figure 5.10. From this calculation, NO_3 concentrations were determined to range between 0 and approximately 20 ppt, with typical concentrations around 2 to 5 ppt throughout the night. This was below the detection limit of the instrument at the time.

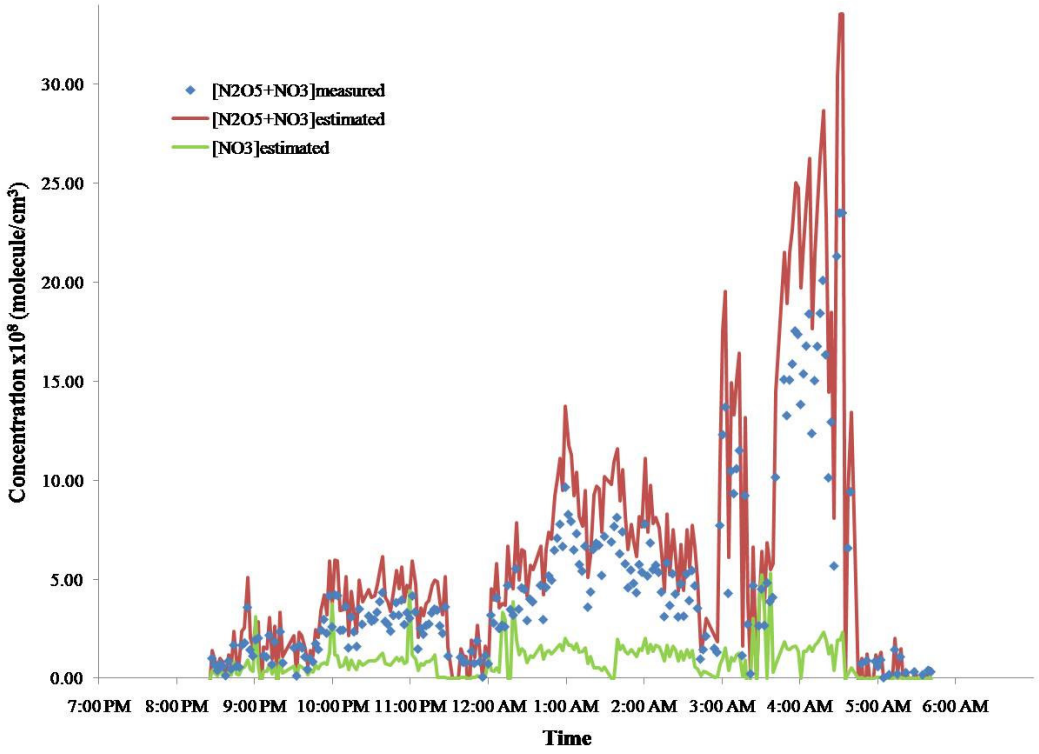

Figure 5.10. N_2O_5 and NO_3 measured and estimated concentrations for May 29-30, 2009. The points represent the measured [N_2O_5 + NO_3], while the lines correspond to the estimated [N_2O_5 + NO_3] and [NO_3] from the temperature dependent equilibrium expression and assuming a transmission efficiency of 70%.

5.5 Potential Instrument Modifications

Temperature fluctuations can greatly affect the stability of the cavity ring-down signal and in turn affect the sensitivity of the instrument. Currently, the instrument comprises of inlets that are directly wrapped in heat tape, while the cavity cells are first mounted in aluminum manifolds and then wrapped in heat tape, both of which are controlled by variacs. With the inlet wrapped directly with heat tape, there is a possibility of non-uniform heating. To prevent this non-uniformity, the inlet can be inserted into a copper or aluminum tube that would then be wrapped in the heat tape, similar to the functionality of the cavity's aluminum manifolds. The temperatures recorded for the inlet and cavity fluctuate ± 2 °C from the desired temperature with the use of heat tape and variacs. Reducing this temperature fluctuation is ideal for more stable ring-down traces. Replacing the heat tape and variacs with Peltier elements could provide maintenance of constant temperatures to within tenths of a degree. In addition, Peltier elements have the ability of being controlled and monitored *via* the computer. The existing setup only allows for recording of the temperature, while the variacs are manually adjusted to reach the desired temperatures.

The purchase of cavity ring-down mirrors with a higher reflectivity would also aid in the reduction of fluctuations in the ring-down traces. The current mirrors have a reflectivity of 99.99878% at 662 nm, giving an ideal τ_0 value of 250 µs. During an experiment ring-downs obtained for this reflectivity are typically between 125 µs and 150 µs. Assuming τ_0 is approximately 150 µs for the absorption of NO_3 at 662 nm with the absorption cross-section of 2.25×10^{-17} $cm^2molecule^{-1}$ and $\Delta\tau_{min}$ is about 1 µs,

$[NO_3]_{min} \approx 9 \times 10^7$ molecules cm^{-3}, or approximately 4 ppt at STP. If τ_0 is now assumed to be 300 μs under the same conditions, $[NO_3]_{min}$ is about 2×10^7 molecules cm^{-3}, or approximately 1 ppt at STP. One has to keep in mind that if the ring-down time is increased too much, resampling the same air mass in the optical cavity may be a concern.

The current instrumentation system is portable, but is still rather bulky. Possible size and weight reductions are probable by replacing the Sirah pulsed dye laser with a Dakota Technologies, Northern Lights pulsed dye laser. The size of the Sirah laser is $570 \times 494 \times 329$ cm^3, while the Dakota Technologies dye laser is $30.5 \times 6.5 \times 11.5$ cm^3. This replacement would also allow for a significant reduction of the custom aluminum framing that houses the instrument. One concern, however, is that the change requires a decrease in quality of the laser system and a comparison of the two should therefore be considered. The Sirah CBR-P dye laser has a tuning range from 370-900 nm, with a wavelength reproducibility of 0.05 nm. In comparison, the Dakota Technologies dye laser can be tuned between 546 and 800 nm, with a wavelength repeatability of 0.01 nm. Both are capable of providing 5-10 mJ/pulse of output power and provide the option of being computer-controlled. From the provided specifications alone, it seems that replacement of the Sirah CBR-P dye laser with the Northern Lights dye laser would offer comparable quality with a significantly more compact design.

6. SUMMARY

Accurate predictive models for atmospheric chemistry, meteorology, and deposition are crucial for the development of pollution control strategies. The ability of the predictive models to correctly characterize these systems relies on accurate data measurements. Therefore, measurement techniques are required to be sensitive, accurate, and capable of resolving the spatial and temporal variations of key chemical species. The species of interest for our measurements include the nitrate radical and dinitrogen pentoxide. The application of a sensitive *in situ* technique, known as cavity ring-down spectroscopy, was introduced to measure these two species simultaneously.

The key nitrogen species involved in tropospheric chemistry in relation to the photolytic NO_x-O_3 cycle were introduced to explain the importance of the nitrate radical and dinitrogen pentoxide. These two species act as reservoirs or a means for removal for NO_x at night. Thus, the nocturnal nitrogen chemistry can have a major impact on the subsequent day's ozone levels.

The basic principles of cavity ring-down spectroscopy, in addition to complications involved with measuring the highly reactive nitrate radical, provided an explanation for the advantages of this technique for detecting NO_3 and N_2O_5. Details of our instrument design and operation based on the experiments by Brown *et al.*[48] provided a starting point for the project. Since then, the instrument underwent numerous revisions before attaining the current setup. The instrument successfully demonstrated the observation of NO_3 and N_2O_5 through laboratory measurements of the nitrate radical

absorption spectrum centered at 662 nm, efficient thermal decomposition of N_2O_5, as well as effective chemical zeroing with addition of nitric oxide upstream of the detection region.

Field observations during September 2008 demonstrated the successful detection of N_2O_5 and NO_3 in the semi-urban atmosphere of College Station, Texas. Detection of N_2O_5 and NO_3 occurred during the evenings of September 15-16 and 21-22, with an average measurement of 30-40 ppt for the heated cavity (i.e. $N_2O_5 + NO_3$ channel). Unfortunately, the 2.5 s integration time and infrequent baseline detection *via* titration with nitric oxide, provided detection limits much greater than those observed in the laboratory. Therefore, we were unable to accurately measure the ambient NO_3 concentrations while at Lick Creek Park. It was also observed that in the early morning hours of the 22nd, the signal became quite noisy and therefore decreased the sensitivity of the instrument. This could be due to an increase in the density of aerosols in the detection region that were not successfully filtered out in the inlet of the system. Regardless of that fact, the sensitivity of the instrument can still be improved by increasing integration times and making more frequent zero measurements.

Since deployment at Lick Creek Park, instrumentation modifications and laboratory measurements are in progress. Modifications include automation of the nitric oxide titration with a solenoid valve controlled in the Labview measurement program, and redesign of the filter mount to be controlled by the computer to avoid physically changing out a filter by hand. Laboratory measurements to determine absolute wall losses and transmission through the filter for NO_3 and N_2O_5 will be performed

simultaneously with and ion-drift chemical ionization mass spectrometer provided by Dr. Zhang in the atmospheric department at Texas A&M University. These changes and measurements are to aid in the calibration of the instrument for the SHARP and SOOT field campaign in Houston, Texas in April and May of 2009. This campaign aims to reveal the details of radical processes involved in the complex atmospheric chemistry of urban areas. Preliminary results from May 29-30, 2009 during the SHARP/SOOT campaign were presented and discussed with N_2O_5 concentrations peaking at approximately 300 ppt and coinciding with the measured ozone, nitric oxide, and nitrogen dioxide fluctuations.

REFERENCES

1. Crutzen, P. J., *Ann. Rev. Earth Plan. Sci.* **1979,** *7*, 443-472.

2. Sander, S. P.; Ravishankara, A. R.; Golden, D. M.; Kolb, C. E.; Kurylo, M. J.; Molina, M. J.; Moortgat, G. K.; Finlayson-Pitts, B. J.; Wine, P. H.; Huie, R. E., *JPL Publication 06-2* **2006**.

3. Platt, U.; Perner, D.; Winer, A. M.; Harris, G. W.; Pitts, J., J. N., *Geophys. Res. Lett.* **1980,** *7*, 89-92.

4. Davis, H. F.; Kim, B.; Johnston, H. S.; Lee, Y. T., *J. Phys. Chem.* **1993,** *97*, 2172-2180.

5. Johnston, H. S.; Davis, H. F.; Lee, Y. T., *J. Phys. Chem.* **1996,** *100* (12), 4713-4723.

6. Penkett, S. A.; Blake, N. J.; Lightman, P.; Marsh, A. R. W.; Anwyl, P.; Butcher, G., *J. Geophys. Res.* **1993,** *98* (D2), 2865-2885.

7. Atkinson, R., *Atmos. Environ.* **2000,** *34* (12-14), 2063-2101.

8. Dentener, F.; Crutzen, P. J., *J. Geophys. Res.* **1993,** *98* (D4), 7149-7163.

9. Geyer, A.; Alicke, B.; Konrad, S.; Schmitz, T.; Stutz, J.; Platt, U., *J. Geophys. Res.* **2001,** *106* (D8), 8013-8025.

10. Stull, R. B., *An Introduction to Boundary Layer Meteorology*. Kluwer Academic Publishers: Dordrecht/Norwell, MA, 1988.

11. Teixeira, J.; Stevens, B.; Bretherton, C. S.; Cederwall, R.; Doyle, J. D.; Golaz, J. C.; Holtslag, A. A. M.; Klein, S. A.; Lundquist, J. K.; Randall, D. A.; Siebesma, A. P.; Soares, P. M. M., *Bull. Amer. Met. Soc.* **2008,** *89* (4), 453-458.

12. Oke, T. R., *Boundary Layer Climates*. 2nd ed.; Routledge: Methuen, London and New York, 1987; p 435.

13. Dabberdt, W. F.; Carroll, M. A.; Baumgardner, D.; Carmichael, G.; Cohen, R.; Dye, T.; Ellis, J.; Grell, G.; Grimmond, S.; Hanna, S.; Irwin, J.; Lamb, B.; Madronich, S.; McQueen, J.; Meagher, J.; Odman, T.; Pleim, J.; Schmid, H. P.; Westphal, D. L., *Bull. Amer. Met. Soc.* **2004,** *85* (4), 563-586.

14. Doran, J. C.; Berkowitz, C. M.; Coulter, R. L.; Shaw, W. J.; Spicer, C. W., *Atmos. Environ.* **2003,** *37*, 2365-2377.

15. Pisano, J. T.; McKendry, I.; Steyn, D. G.; Hastie, D. R., *Atmos. Environ.* **1997,** *31* (14), 2071-2078.

16. Wang, S.; Ackermann, R.; Stutz, J., *Atmos. Chem. Phys.* **2006,** *6*, 2671-2693.

17. Stutz, J.; Wong, K. W.; Lawrence, L.; Ziemba, L.; Flynn, J. H.; Rappengluck, B.; Lefer, B., *Atmos. Environ.* **2009**, doi: 10.1016/j.atmosenv.2009.03.004.

18. Geyer, A.; Stutz, J., *J. Geophys. Res.* **2004,** *109* (D12), D12307.

19. Cros, B.; Fontan, J.; Minga, A.; Helas, G.; Nganga, D.; Delmas, R.; Chapuis, A.; Beneech, B.; Druilhet, A.; Andreae, M. O., *J. Geophys. Res.* **1992,** *97*, 12877.

20. Beyrich, F.; Weisensee, U.; Sprung, D.; Gusten, H., *Bound. Lay. Met.* **1996,** *81*, 1-9.

21. Gusten, H.; Heinrich, G.; Sprung, D., *Atmos. Environ.* **1998,** *32*, 1195-1202.

22. Zhang, J.; Rao, S. T., *J. Appl. Meteorol.* **1999,** *38*, 1674-1691.

23. Glaser, K.; Vogt, U.; Baumbach, G.; Volz-Thomas, A.; Geiss, H., *J. Geophys. Res.* **2003,** *108* (D4), 8253.

24. Stutz, J.; Alicke, B.; Ackermann, R. J.; Geyer, A.; White, A.; Williams, E., *J. Geophys. Res.* **2004,** *109*, D12306.

25. Brown, S. S.; Stark, H.; Ravishankara, A. R., *J. Geophys. Res.* **2003,** *108* (D17), 4539.

26. Platt, U.; Winer, A. M.; Bierman, H. W.; Atkinson, R.; Pitts, J., J. N., *Environ. Sci. Technol.* **1984,** *18*, 365-369.

27. Brown, S. S.; Dube, W. P.; Osthoff, H. D.; Stutz, J.; Ryerson, T. B.; Wollny, A. G.; Brock, C. A.; Warneke, C.; de Gouw, J. A.; Atlas, E.; Neuman, J. A.; Holloway, J. S.; Lerner, B. M.; Williams, E.; Kuster, W. C.; Goldan, P. D.; Angevine, W. M.; Trainer, M.; Fehsenfeld, F. C.; Ravishankara, A. R., *J. Geophys. Res.* **2007,** *112*, D22304.

28. Brown, S. S.; Dube, W. P.; Osthoff, H. D.; Wolfe, D. E.; Angevine, W. M.; Ravishankara, A. R., *Atmos. Chem. Phys.* **2007,** *7*, 139-149.

29. Wayne, R. P.; Barnes, I.; P., B.; Burrows, J. P.; Canosa-Mas, C. E.; Hjorth, J.; Le Bras, G.; Moortgat, G. K.; Perner, D.; Poulet, G.; Restelli, G.; Sidebottom, H., *Atmos. Environ.* **1991,** *25A* (1), 1-203.

30. Sander, S. P., *J. Phys. Chem.* **1986,** *90*, 4135-4142.

31. Cantrell, C. A.; Davidson, J. A.; Shetter, R. E.; Anderson, B. A.; Calvert, J. G., *J. Phys. Chem.* **1987,** *91*, 5858-5863.

32. Yokelson, R. J.; Burkholder, J. B.; Fox, R. W.; Talukdar, R. K.; Ravishankara, A. R., *J. Phys. Chem.* **1994,** *98* (50), 13144-13150.

33. Orphal, J.; Fellows, C. E.; Flaud, P.-M., *J. Geophys. Res.* **2003,** *108* (D3), 4077.

34. Osthoff, H. D.; Pilling, M. J.; Ravishankara, A. R.; Brown, S. S., *Phys. Chem. Chem. Phys.* **2007,** *9*, 5785-5793.

35. Schneider, W.; Moortgat, G. K.; Burrows, J. P.; Tyndall, G. S., *J. Photochem. Photobiol. A Chem.* **1987,** *40*, 195.

36. Coheur, P.-F.; Fally, S.; Carleer, M.; Clerbaux, C.; Colin, R.; Jenouvrier, A.; Merienne, M.-F.; Hermans, C.; Vandaele, A. C., *J. Quant. Spectrosc. Radiat. Trans.* **2002,** *74* (4), 493-510.

37. Fally, S.; Coheur, P.-F.; Carleer, M.; Clerbaux, C.; Colin, R.; Jenouvrier, A.; Merienne, M.-F.; Hermans, C.; Vandaele, A. C., *J. Quant. Spectrosc. Radiat. Trans.* **2003,** *82* (1-4), 119-131.

38. Burkholder, J. B.; Talukdar, R. K., *Geophys. Res. Lett.* **1994,** *21* (7), 581-584.

39. Allan, B. J.; McFiggans, G.; Plane, J. M. C.; Coe, H.; McFadyen, G. G., *J. Geophys. Res.* **2000,** *105* (D19), 24191-24204.

40. Platt, U.; Perner, D.; Schroder, J.; Kessler, C.; Toennissen, A., *J. Geophys. Res.* **1981,** *86* (C12), 11965-11970.

41. Allan, B. J.; Plane, J. M. C.; Coe, H.; Shillito, J. A., *J. Geophys. Res.* **2002,** *107* (D21), 4588.

42. Atkinson, R.; Winer, A. M.; Pitts, J., J. N., *Atmos. Environ.* **1986,** *20* (2), 331-339.

43. Geyer, A.; Alicke, B.; Mihelcic, D.; Stutz, J.; Platt, U., *J. Geophys. Res.* **1999,** *104* (D21), 26,097-26,105.

44. Mihelcic, D.; Klemp, D.; Musgen, P.; Patz, H. W.; Volz-Thomas, A., *J. Atmos. Chem.* **1993,** *16*, 313-335.

45. Slusher, D. L.; Huey, G. L.; Tanner, D. J.; Flocke, F. M.; Roberts, J. M., *J. Geophys. Res.* **2004,** *109* (D19315).

46. Zheng, J.; Zhang, R.; Fortner, E. C.; Volkamer, R. M.; Molina, L.; Aiken, A. C.; Jimenez, J. L.; Gaeggeler, K.; Dommen, J.; Dusanter, S.; Stevens, P. S.; Tie, X., *Atmos. Chem. Phys.* **2008,** *8*, 6823-6838.

47. Brown, S. S.; Stark, H.; Ciciora, S. J.; Ravishankara, A. R., *Geophys. Res. Lett.* **2001,** *28* (17), 3227-3230.

48. Brown, S. S.; Stark, H.; Ciciora, S. J.; McLaughlin, R. J.; Ravishankara, A. R., *Rev. Sci. Instrum.* **2002,** *73* (9), 3291-3301.

49. Brown, S. S.; Stark, H.; Ryerson, T. B.; Williams, E. J.; Nicks, D. K., Jr.; Trainer, M.; Fehsenfeld, F. C.; Ravishankara, A. R., *J. Geophys. Res.* **2003,** *108* (D9), 4299.

50. Dube, W. P.; Brown, S. S.; Osthoff, H. D.; Nunley, M. R.; Ciciora, S. J.; Paris, M. W.; McLaughlin, R. J.; Ravishankara, A. R., *Rev. Sci. Instrum.* **2006,** *77* (3), 034101-034111.

51. King, M. D.; Dick, E. M.; Simpson, W. R., *Atmos. Environ.* **2000,** *34* (5), 685-688.

52. Simpson, W. R., *Rev. Sci. Instrum.* **2003,** *74* (7), 3442.

53. Ball, S. M.; Povey, I. M.; Norton, E. G.; Jones, R. L., *Chem. Phys. Lett.* **2001,** *342* (1-2), 113-120.

54. Bitter, M.; Ball, S. M.; Povey, I. M.; Jones, R. L., *Atmos. Chem. Phys.* **2005,** *5*, 2547-2560.

55. Wood, E. C.; Wooldridge, P. J.; Freese, J. H.; Albrecht, T.; Cohen, R. C., *Environ. Sci. Technol.* **2003,** *37* (24), 5732-5738.

56. Wood, E. C.; Bertram, T. H.; Wooldridge, P. J.; Cohen, R. C., *Atmos. Chem. Phys.* **2005,** *5*, 483-491.

57. Matsumoto, J.; Kosugi, N.; Imai, H.; Kajii, Y., *Rev. Sci. Instrum.* **2005,** *76* (6), 064101.

58. Matsumoto, J.; Imai, H.; Kosugi, N.; Kajii, Y., *Atmos. Environ.* **2005,** *39* (36), 6802-6811.

59. Herbelin, J. M.; McKay, J. A.; Kwok, M. A.; Ueunten, R. H.; Urevig, D. S.; Spencer, D. J.; Benard, D. J., *Applied Optics* **1980,** *19* (1), 144-147.

60. O'Keefe, A.; Deacon, D. A. G., *Rev. Sci. Instrum.* **1988,** *59*, 2544-2551.

61. Paul, J. B.; Saykally, R. J., *Analyt. Chem.* **1997,** *69*, A287-A292.

62. Scherer, J. J.; Paul, J. B.; O'Keefe, A.; Saykally, R. J., *Chem. Rev.* **1997,** *97*, 25-51.

63. Busch, K. W.; Busch, M. A., *Cavity-ringdown Spectroscopy: an Ultratrace-absorption Measurement Technique*. American Chemical Society: Washington, D. C., 1999.

64. Pettersson, A.; Lovejoy, E. R.; Brock, C. A.; Brown, S. S.; Ravishankara, A. R., *J. Aerosol Sci.* **2004,** *35* (8), 995-1011.

65. Davidson, J. A.; Viggiano, A. A.; Howard, C. J.; Dotan, I.; Fehsenfeld, F. C.; Albritton, D. L.; Ferguson, E. E., *J. Chem. Phys.* **1978,** *68* (5), 2085-2087.

66. Osborne, B. A.; Marston, G.; Kaminski, L.; Jones, N. C.; Gingell, J. M.; Mason, N.; Walker, I. C.; Delwiche, J.; Hubin-Franskin, M.-J., *J. Quant. Spectrosc. Radiat. Trans.* **2000,** *64*, 67-74.

67. Cantrell, C. A.; Shetter, R. E.; Calvert, J. G.; Tyndall, G. S.; Orlando, J. J., *J. Phys. Chem.* **1993,** *97* (36), 9141-9148.

68. Google Maps. www.google.com (accessed January 2009).

69. Monson, R. K.; Trahan, N.; Rosenstiel, T. N.; Veres, P.; Moore, D.; Wilkinson, M.; Norby, R. J.; Volder, A.; Tjoelker, M. G.; Briske, D. D.; Farnosky, D. F.; Fall, R., *Phil. Trans. R. Soc. A* **2007,** *365*, 1677-1695.

70. Barnes, I.; Bastian, V.; Becker, K. H.; Tong, Z., *J. Phys. Chem.* **1990,** *94* (6), 2413-2419.

71. Draxler, R. R.; Rolph, G. D. HYSPLIT (HYbrid Single-Particle Lagrangian Integrated Trajectory) Model access via NOAA ARL READY Website. http://www.arl.noaa.gov/ready/hysplit4.html.

72. Rolph, G. D. Real-Time Environmental Applications and Display sYstem (READY) Website. http://www.arl.noaa.gov/ready/hysplit4.html.

73. Texas Commission on Environmental Quality. http://www.tceq.state.tx.us (accessed October 2008).

74. Louisiana Department of Environmental Quality. http://www.deq.louisiana.gov/portal (accessed October 2008).

75. Estes, M., Overview of Ozone Exceedances in Houston and Dallas. In *TexAQSII Rapid Science Synthesis Workshop*, Houston, 2006.

76. Brown, S. S.; Ryerson, T. B.; Wollny, A. G.; Brock, C. A.; Peltier, R.; Sullivan, A. P.; Weber, R. J.; Dube, W. P.; Trainer, M.; Meagher, J. F.; Fehsenfeld, F. C.; Ravishankara, A. R., *Science* **2006,** *311* (5757), 67-70.

77. Mak, J.; Gross, S.; Bertram, A. K., *Geophys. Res. Lett.* **2007,** *34*, L10804.

78. Thornton, J. A.; Braban, C. F.; Abbatt, J. P. D., *Phys. Chem. Chem. Phys.* **2003,** *5*, 4593-4603.

79. Thornton, J. A.; Abbatt, J. P. D., *J. Phys. Chem. A* **2005,** *109* (44), 10004-10012.

80. Zhang, R.; Zheng, J., Texas A & M University. personal communication.

81. Lefer, B.; Flynn, J. H.; Rappengluck, B., University of Houston. personal communication.

VITA

Name:	Katie Christine Perkins
Address:	Department of Chemistry, Texas A&M University, PO Box 30012 College Station, TX 77842-3012
Email Address:	katiecperkins@gmail.com
Education:	B.S., Chemistry, Truman State University, 2004 Ph. D., Chemistry, Texas A&M University, 2009